

**Analysis of  
electron diffraction patterns  
from carbon nanotubes  
with image processing  
to determine structural parameters**

DISSERTATION

zur Erlangung des Doktorgrades  
der Naturwissenschaften (Dr. rer. nat.)  
der Naturwissenschaftlichen Fakultät II - Physik -  
der Universität Regensburg

vorgelegt von

**DOMINIK SENNINGER**

aus

Regen

2011

Promotionsgesuch eingereicht am 06.07.2011.

Die Arbeit wurde durchgeführt am Institut für Biophysik und physikalische Biochemie unter der Anleitung von Prof. Dr. Elmar W. Lang.

Prüfungsausschuss:

- Vorsitzender : Prof. Dr. Karsten Rincke
- 1. Gutachter : Prof. Dr. Elmar W. Lang
- 2. Gutachter : Prof. Dr. Christoph Strunk
- 3. Prüfer : Prof. Dr. Ingo Morgenstern

# Contents

<b>1</b>	<b>Introduction</b>	<b>7</b>
<b>2</b>	<b>Carbon nanotubes</b>	<b>9</b>
2.1	Atomic structure of carbon nanotubes . . . . .	9
2.2	Diffraction from nanotubes . . . . .	12
2.2.1	Atomic scattering amplitude . . . . .	12
2.2.2	Diffraction from a continuous helix . . . . .	13
2.2.3	Electron diffraction from a nanotube . . . . .	17
2.2.4	Selection rule . . . . .	18
2.2.5	Structure factor of a carbon nanotube . . . . .	19
2.2.6	Cylindrical correction . . . . .	22
2.2.7	Multi-walled nanotubes . . . . .	23
2.3	Determination of chiral indices . . . . .	25
2.3.1	Principal layer lines . . . . .	25
2.3.2	Direct method . . . . .	25
2.3.3	Ratio of indices $m/n$ . . . . .	29
2.4	Symmetry . . . . .	30
<b>3</b>	<b>Auxiliary algorithms for the (pre)processing</b>	<b>35</b>
3.1	Generalized Linear Least Squares . . . . .	35
3.2	Snake algorithm . . . . .	38
3.2.1	Overview . . . . .	38
3.2.2	Inner energy . . . . .	39
3.2.3	Outer energy . . . . .	41
3.2.4	Normalizations . . . . .	43
<b>4</b>	<b>The analysis algorithm</b>	<b>45</b>
4.1	Simulation of diffraction patterns . . . . .	46
4.2	Approximate determination of center . . . . .	48

4.3	Delineation of the beamstopper . . . . .	50
4.3.1	Initialization of the snake algorithm . . . . .	50
4.3.2	Application of the snake algorithm . . . . .	51
4.4	Normalization of the intensity . . . . .	54
4.5	Layer line distances . . . . .	57
4.5.1	Determination of the equatorial line . . . . .	57
4.5.2	Radius of the first reflection spots . . . . .	58
4.5.3	Correction of center and angle . . . . .	59
4.5.4	Determination of the ellipse parameters . . . . .	65
4.5.5	Determination of the layer line distances . . . . .	65
4.5.6	Improvement of the accuracy . . . . .	70
4.6	Selection of the possible tubes . . . . .	71
4.6.1	Estimation of the error of the measured $m/n$ . . . . .	72
4.6.2	Score for the ratio . . . . .	73
4.7	Comparison of the candidates to the simulation . . . . .	74
4.7.1	Correction of the center using the layer lines . . . . .	74
4.7.2	Determination of the scale and the incidence angle . . . . .	75
4.7.3	Comparison of the maxima distances on the layer lines . . . . .	79
<b>5</b>	<b>Algorithm testing with simulated patterns</b>	<b>83</b>
5.1	Broad layer lines . . . . .	83
5.2	Low intensity of the reflections . . . . .	88
5.3	Special cases of nanotubes . . . . .	91
5.3.1	“Zigzag” nanotube . . . . .	91
5.3.2	“Armchair” nanotube . . . . .	93
5.4	Bundle of tubes . . . . .	94
<b>6</b>	<b>Analysis of experimental patterns</b>	<b>97</b>
6.1	Single-walled tube . . . . .	97
6.1.1	Noise reduction . . . . .	97
6.1.2	Rough detection of the center . . . . .	99
6.1.3	Parasitic stripe of high intensity . . . . .	99
6.1.4	Detection of the beamstopper . . . . .	101
6.1.5	Normalization of the intensity . . . . .	101
6.1.6	Determination of the radius . . . . .	103
6.1.7	Correction of the center . . . . .	104
6.1.8	Determination of the layer line distances . . . . .	105

6.1.9	Center correction using the layer lines . . . . .	106
6.1.10	Determination of the maxima positions on the layer lines . . .	107
6.1.11	Comparison between measurement and simulation . . . . .	109
6.2	Analysis of bundle . . . . .	111
6.2.1	Noise Reduction . . . . .	111
6.2.2	Rough determination of the center . . . . .	112
6.2.3	Delineation of the beamstopper . . . . .	113
6.2.4	Normalization of the intensity . . . . .	113
6.2.5	Determination of the radius . . . . .	116
6.2.6	Correction of the center . . . . .	116
6.2.7	Determination of the layer line distances . . . . .	117
6.2.8	Analysis of the layer lines . . . . .	120
<b>7</b>	<b>Conclusions</b>	<b>127</b>
<b>A</b>	<b>Table of carbon nanotubes</b>	<b>131</b>



# Chapter 1

## Introduction

For a long time, graphite and diamond have been the only known crystalline structures of carbon. But in 1985 the fullerenes were discovered, which led to a Nobel prize. Professor Sumio Iijima by chance observed multi-walled carbon nanotubes in an electron microscope for the first time in 1991. Two years later single-walled nanotubes could be detected. Since that time, carbon nanotubes represent a popular and interesting field of research.

The structure of a single-walled carbon nanotube can be described as a rectangle cut out of a single graphite layer (graphene), which is rolled up to form a cylinder. The structure, i.e. the diameter and the chirality, is then uniquely defined by the so called chiral indices  $(n, m)$ .

Carbon nanotubes possess many interesting characteristics. For instance their tensile strength is extremely high in relation to their weight [1]. However the probably most amazing features are their electrical properties. There exist semiconducting tubes and metallic-conducting tubes. Which kind of conductivity a tube possesses, depends on its chiral indices [1]. Furthermore the band gap depends on the diameter. After the growing of a carbon nanotube in the experiment its chiral indices are not known. However it would be desirable to know, which structure the tube possesses, before measurements (for example a measurement of the conductivity) are done. The analysis in a Transmission Electron Microscope (TEM) proved to be a good choice to estimate the structure.

In high resolution images in real space usually only the diameter can be determined. Since the properties depend strongly on the chirality, it is necessary to estimate the helical angle too. Therefore electron diffraction in a TEM is a suited method.

The analysis of these diffraction patterns by hand is nontrivial and needs expertise. Additionally the recording of a diffraction pattern of a nanotube is quite hard, so

the quality of the images is often not perfect. The analysis is challenging especially of images of low quality. By that the result of the analysis might be different, in case of different persons performing it. An analysis, which is done by an algorithm, is objective and always leads to the same result.

Therefore the goal of this work is to develop an algorithm, which analyzes diffraction patterns autonomously. For user-friendliness a graphical user interface was programmed, which gives the user the possibility to follow the individual steps of the analysis and even correct steps, if necessary.

The thesis is arranged as follows: First of all in chapter 2 the atomic structure of carbon nanotubes and the chiral indices  $(n, m)$  are described. From this structure the corresponding diffraction pattern is derived. Afterwards possibilities are presented, how the chiral indices may be obtained from the diffraction pattern.

Chapter 3 describes two methods, which are used for the analysis respectively the preprocessing. The presented General Linear Least Squares (GLLS) algorithm is useful to approximate measured data by functions. The other method, that is described, is the snake algorithm, which is able to automatically detect objects in images by following their edges.

The actual analysis algorithm is explained step by step in chapter 4 using the example of a simulated image, which was adapted to the features of experimental images. First of all the steps of the preprocessing are described, like the delineation of the beamstopper and the normalization of the intensity. Afterwards a set of possible tubes, called candidates, is obtained by the evaluation of the distances of the diffraction spots. Afterwards the measured intensity distributions are compared to simulated curves to reduce the number of candidates.

The algorithm is applied to several different simulated images, which possess special properties, in chapter 5. It is tested how the algorithm can deal with strongly widened diffraction spots and low intensity and how the special cases of nanotubes (“zigzag” and “armchair”) and bundles of tubes are treated.

Chapter 6 explains the behavior of the algorithm analyzing two experimental diffraction patterns. At first the analysis of an image of a single-walled tube is described, which was taken at the University of Regensburg by Christian Huber. The second part of that chapter deals with the analysis of a diffraction pattern of a bundle of tubes or a multi-walled tube.

# Chapter 2

## Carbon nanotubes

The structure of a carbon nanotube can be illustrated by rolling up a single graphite layer (graphene). The atomic structure of a nanotube is uniquely characterized by two indices  $n$  and  $m$ . These indices also determine the electric conductance of the nanotube: If the difference  $n - m$  is a multiple of three, the tube is metallic-conducting, else it is semiconducting. The theory in this chapter is mainly based on a paper of Lu-Chang Qin [4].

### 2.1 Atomic structure of carbon nanotubes

The basis vectors  $\vec{a}_1$  and  $\vec{a}_2$  ( $a_1 = a_2 = a_0 = 0.246$  nm), which include an angle of  $60^\circ$ , are defined to describe the graphene lattice (cf. figure 2.1). The plane grid is also referred as the radial projection of the nanotube. Using the crystallographic basis vectors defined in real space, the basis vectors  $\vec{a}_1^*$  and  $\vec{a}_2^*$  in the reciprocal space can be written as [2]:

$$\begin{aligned}\vec{a}_1^* &= 2\pi \frac{2}{3a_0^2} (2\vec{a}_1 - \vec{a}_2) \\ \vec{a}_2^* &= 2\pi \frac{2}{3a_0^2} (-\vec{a}_1 + 2\vec{a}_2)\end{aligned}\tag{2.1}$$

On the graphene lattice, the tube can be described by a vector  $(n, m)$ , which determines the perimeter (cf. figure 2.1). These two positive integers  $n$  and  $m$  are called the *chiral indices*. For given indices  $(n, m)$  the perimeter vector is [4]:

$$\vec{A} = (n, m) = n\vec{a}_1 + m\vec{a}_2\tag{2.2}$$

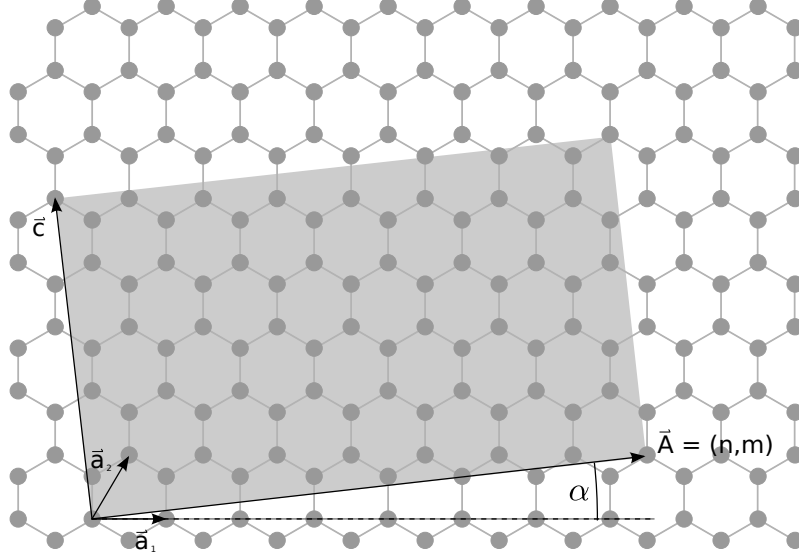


Figure 2.1: Schematic structure of graphene with basis vectors  $\vec{a}_1$  and  $\vec{a}_2$ . The gray rectangle is the radial projection of a carbon nanotube (7, 1) with perimeter  $\vec{A}$  and helical angle  $\alpha$ . Vector  $\vec{c}$  describes the tube axis (image adapted from [4]).

The perimeter is given by  $A = |\vec{A}| = a_0(n^2 + m^2 + nm)^{1/2}$  and the diameter of the tube by  $d = A/\pi$ . The tube axis  $\vec{c} = (n_c, m_c)$ , which is perpendicular to the chiral vector  $\vec{A}$ , can be calculated using the orthogonality between the perimeter and the axis:

$$(n, m) \cdot (n_c, m_c) = nn_c + mm_c + \frac{nm_c + n_cm}{2} = 0 \quad (2.3)$$

$$\implies \frac{n_c}{m_c} = -\frac{n + 2m}{2n + m} \quad (2.4)$$

The indices of the tube axis  $(n_c, m_c)$  are chosen such, that the only common divisor is 1. With the greatest common divisor  $M$  of  $(2n + m)$  and  $(n + 2m)$ , one gets the axial lattice vector  $(n_c, m_c)$ :

$$\begin{aligned} n_c &= -\frac{n + 2m}{M} \\ m_c &= \frac{2n + m}{M} \end{aligned} \quad (2.5)$$

The periodicity along the tube axis can be written as:

$$c = a_0 \sqrt{n_c^2 + m_c^2 + n_cm_c} = \frac{\sqrt{3}a_0}{M} \sqrt{n^2 + m^2 + nm} = \frac{\sqrt{3}A}{M} \quad (2.6)$$

If one cuts a rectangle with side length  $A$  and  $c$  out of graphene and rolls this

rectangle up along an axis perpendicular to the perimeter vector  $\vec{A}$ , one gets a cylindrical nanotube. The helical angle  $\alpha$ , which is defined as angle between the perimeter vector  $\vec{A} = (n, m)$  and the basis vector  $\vec{a}_1$ , is given by:

$$\begin{aligned}\alpha &= \cos^{-1} \left( \frac{2n + m}{2\sqrt{(n^2 + m^2 + nm)}} \right) \\ &= \sin^{-1} \left( \frac{\sqrt{3}m}{2\sqrt{n^2 + m^2 + nm}} \right) \\ &= \tan^{-1} \left( \frac{\sqrt{3}m}{2n + m} \right)\end{aligned}\tag{2.7}$$

The positions of the atoms can be described in two different ways. First Cartesian coordinates  $(x_j, z_j)$  in the radial projection of the tube onto a rectangle with side length  $A$  and  $c$  can be used. Second it is possible to depict the positions of the atoms in cylindrical coordinates  $(\phi_j, z_j)$ . The atomic structure of a carbon nanotube can be described by pairs of parallel helices of carbon atoms. There are three equivalent helices, which are aligned to the crystallographic directions  $\vec{a}_1$ ,  $\vec{a}_2$  respectively  $\vec{a}_3 = \vec{a}_2 - \vec{a}_1$ . Each helix again consists of two atomic helices, which are shifted by a vector. Each unit cell contains  $m$  pairs of helices parallel to  $\vec{a}_1$ ,  $n$  pairs of helices parallel to  $\vec{a}_2$  or  $n + m$  pairs of helices parallel to  $\vec{a}_3$ .

Relative to a carbon atom, which is located at the origin  $\phi_0^0 = 0$  and  $z_0^0 = 0$ , the positions of the  $n + m$  atoms of the primary helix parallel to  $\vec{a}_1$  can be written as:

$$\begin{aligned}\phi_j^{(1,0)} &= -2\pi j a_0 \cos(\alpha) / A \\ z_j^{(1,0)} &= j a_0 \sin(\alpha) \\ \text{with } j &= 0, 1, 2, \dots, n + m\end{aligned}\tag{2.8}$$

The positions of the secondary helix are:

$$\begin{aligned}\phi_j^{(1,1)} &= \phi_j^{(1,0)} + \frac{2\pi a_0}{\sqrt{3}A} \cos(30^\circ + \alpha) \\ z_j^{(1,1)} &= z_j^{(1,0)} + \frac{a_0}{\sqrt{3}} \sin(30^\circ + \alpha) \\ \text{with } j &= 0, 1, 2, \dots, n + m\end{aligned}\tag{2.9}$$

The helices parallel to  $\vec{a}_2$  and  $\vec{a}_3$  could be given analogously.

Due to the hexagonal rotational symmetry of the graphene lattice, the non-degenerated interval for the helical angle is between  $0^\circ$  and  $60^\circ$ . Values between  $30^\circ$  and  $60^\circ$  are

assigned to left-handed tubes, whereas the interval between  $0^\circ$  and  $30^\circ$  is assigned to right-handed tubes.

If the handedness of the tube is ignored, the chiral angle is limited to the interval  $[0^\circ, 30^\circ]$ , which yields the following conditions for the chiral indices:

$$\begin{aligned} n &> 0 \\ n \geq m \geq 0 \end{aligned} \tag{2.10}$$

The rotational symmetry of a nanotube can be determined by looking at the chiral indices. A tube with indices  $(n, m)$  possesses an  $M$ -fold rotational symmetry, where  $M$  is the greatest common divisor of  $n$  and  $m$ . If  $m = 0$ , it possesses an  $n$ -fold rotational symmetry, for even  $n$  it is also centrosymmetric. There are two special cases with non-helical structure which should be mentioned. First the so called “zigzag” structure, which has indices of the form  $(n, 0)$  and an helical angle of  $0^\circ$ . The second case describes the “armchair” structure with indices of the form  $(n, n)$  and an helical angle of  $30^\circ$ . For the “zigzag” structure the tube axis is given by  $(n_c, m_c) = (-1, 2)$ , for the “armchair” structure by  $(n_c, m_c) = (-1, 1)$  [4].

## 2.2 Electron diffraction from carbon nanotubes

Diffraction is an effective method to determine periodic structures. Evaluable diffraction effects only occur, if the wave length of the used radiation is similar to the size of the period of the examined material. Electrons fulfill this condition for atomic dimensions, so a Transmission Electron Microscope (TEM) is suitable for the determination of the structure of carbon nanotubes.

### 2.2.1 Atomic scattering amplitude

If fast electrons hit an atom, the atomic scattering amplitude can approximatively be described by the first Born approximation [4]:

$$f(\vec{q}) = \frac{2\pi m e}{h^2} \int v(\vec{r}) \exp [2\pi i \vec{q} \cdot \vec{r}] d\vec{r} \tag{2.11}$$

where  $v(\vec{r})$  is the Coulomb-potential of the scattering atom,  $e$  the elementary charge,  $m$  the relativistic mass of the electron,  $h$  the Planck constant and  $\vec{q}$  the scattering vector of the length

$$q = \frac{2\sin(\Theta/2)}{\lambda} \quad (2.12)$$

where  $\Theta$  is the total scattering angle and  $\lambda$  is the wave length of the incoming electron beam. The values of the scattering amplitudes can be looked up in tables [14].

### 2.2.2 Diffraction from a continuous helix

The electron scattering amplitude can be expressed by the structure factor

$$F(\vec{q}) = \int V(\vec{r}) \exp [2\pi i \vec{q} \cdot \vec{r}] d\vec{r} \quad (2.13)$$

where

$$V(\vec{r}) = ((2\pi me)/h^2)U(\vec{r}) \quad (2.14)$$

is the modified scattering potential with the Coulomb potential  $U(\vec{r})$  of the scattering object. The measured intensity  $I(\vec{q})$  of the diffracted beam in reciprocal space is given by:

$$I(\vec{q}) = |F(\vec{q})|^2 \quad (2.15)$$

In the general case, where Friedel's Law is valid [3], the intensity distribution is always centrosymmetric independent of the scattering potential, i.e.:

$$I(-\vec{q}) = I(\vec{q}) \quad (2.16)$$

Because the nanotube is a cylindrical object, it is more convenient to describe the scattering amplitude in polar coordinates  $(r, \phi, z)$ , which are related to Cartesian coordinates in the following way:

$$\begin{aligned} x &= r \cos(\phi) \\ y &= r \sin(\phi) \\ z &= z \end{aligned} \quad (2.17)$$

In reciprocal space we get:

$$\begin{aligned} X &= R \cos(\Phi) \\ Y &= R \sin(\Phi) \\ Z &= Z \end{aligned} \quad (2.18)$$

With use of the addition theorem

$$\cos(\alpha) \cos(\beta) + \sin(\alpha) \sin(\beta) = \cos(\alpha - \beta) \quad (2.19)$$

we can rewrite the structure factor in polar coordinates:

$$\begin{aligned} F(R, \Phi, Z) &= \int V(\vec{r}) \exp [2\pi i \vec{q} \cdot \vec{r}] d\vec{r} \\ &= \int_{-\infty}^{+\infty} \int_0^{2\pi} \int_0^{\infty} V(r, \phi, z) \exp [2\pi i (rR \cos(\Phi) \cos(\phi) \\ &\quad + rR \sin(\Phi) \sin(\phi) + Zz)] r dr d\phi dz \\ &= \int_{-\infty}^{+\infty} \int_0^{2\pi} \int_0^{\infty} V(r, \phi, z) \exp [2\pi i rR \cos(\Phi - \phi)] \\ &\quad \times \exp [2\pi i zZ] r dr d\phi dz \end{aligned} \quad (2.20)$$

Using the Bessel function  $J_\nu$  of order  $\nu$

$$2\pi i^\nu J_\nu(u) = \int_0^{2\pi} \exp [i u \cos(\phi) + i \nu \phi] d\phi \quad (2.21)$$

and the relation

$$\exp [iu \cos(\phi)] = \sum_{\nu=-\infty}^{+\infty} J_\nu(u) \exp \left[ i \nu \left( \phi + \frac{\pi}{2} \right) \right] \quad (2.22)$$

we get:

$$\begin{aligned}
F(R, \Phi, Z) &= \sum_{\nu=-\infty}^{+\infty} \int_{-\infty}^{+\infty} \int_0^{2\pi} \int_0^{\infty} V(r, \phi, z) J_{\nu}(2\pi r R) \exp \left[ i \nu \left( \Phi - \phi + \frac{\pi}{2} \right) \right] \\
&\quad \times \exp [2\pi i z Z] r dr d\phi dz \quad (2.23) \\
&= \sum_{\nu=-\infty}^{+\infty} \exp \left[ i \nu \left( \Phi + \frac{\pi}{2} \right) \right] \int_{-\infty}^{+\infty} \int_0^{2\pi} \int_0^{\infty} V(r, \phi, z) J_{\nu}(2\pi r R) \\
&\quad \times \exp [-i \nu \phi + 2\pi i z Z] r dr d\phi dz
\end{aligned}$$

If the potential  $V(r, \phi, z)$  possesses  $N$ -fold rotational symmetry relative to the  $z$ -axis, i.e.:

$$V(r, \phi, z) = V \left( r, \phi + \frac{2\pi}{N}, z \right) \quad (2.24)$$

the Fourier expansion can be written as:

$$V(r, \phi, z) = \sum_{\nu=-\infty}^{+\infty} V_{\nu N}(r, z) \exp[i \nu N \phi] \quad (2.25)$$

with

$$V_{\nu N}(r, z) = \frac{N}{2\pi} \int_0^{2\pi/\nu} V(r, \phi, z) \exp[-i \nu N \phi] d\phi \quad (2.26)$$

The structure factor is then given by

$$\begin{aligned}
F(R, \Phi, Z) &= N \sum_{\nu=-\infty}^{+\infty} \exp \left[ i \nu N \left( \Phi + \frac{\pi}{2} \right) \right] \int_{-\infty}^{+\infty} \int_0^{2\pi} \int_0^{\infty} V(r, \phi, z) \\
&\quad \times J_{\nu N}(2\pi r R) \exp[2\pi i z Z] \exp[-i \nu N \phi] r dr d\phi dz \quad (2.27)
\end{aligned}$$

For an object with an iterating structure with period  $c$  in direction of the  $z$ -axis, the Fourier expansion can be written as:

$$V(r, \phi, z) = \sum_{\nu=-\infty}^{+\infty} \sum_{l=-\infty}^{+\infty} V_{\nu l} \exp \left[ -i \nu \phi + \frac{2\pi i l z}{c} \right] \quad (2.28)$$

This yields the structure factor:

$$F(R, \Phi, l) = \frac{1}{c} \sum_{\nu=-\infty}^{\infty} \exp \left[ i \nu \left( \phi + \frac{\pi}{2} \right) \right] \int_0^c \int_0^{2\pi} \int_0^{\infty} V(r, \phi, z) J_{\nu}(2\pi r R) \quad (2.29)$$

$$\times \exp \left[ i \left( -\nu \phi + \frac{2\pi l z}{c} \right) \right] r dr d\phi dz$$

with  $J_{\nu}$  the Bessel function of order  $\nu$ . In a continuous helix the scattering potential is given by:

$$V(r, \phi, z) = V_0 \delta(r - r_0) \delta \left( \frac{2\pi z}{C} - \phi \right) \quad (2.30)$$

where  $r_0$  represents the radius of the helix and  $C$  the pitch length. In this potential we only get a non-zero contribution, if  $l = \nu$ . Now we have the following scattering amplitude:

$$F(R, \Phi, l) = r_0 V_0 J_l(2\pi r_0 R) \exp \left[ i \left( \Phi + \frac{\pi}{2} \right) l \right] \quad (2.31)$$

The associated scattering intensity is:

$$I(R, \Phi, l) = |F(R, \Phi, l)|^2 = r_0^2 V_0^2 [J_l(2\pi r_0 R)]^2 \quad (2.32)$$

Two characteristics of the diffraction pattern of a helix should be considered particularly:

- The intensity is limited to discrete lines (layer lines), which are indexed by  $l \in \mathbb{Z}$ .
- The intensity on layer line  $l$  is proportional to the square of the Bessel function of order  $l$ .

With a second helix, formed by a rotation by  $\pi$ , the potential is

$$V(r, \phi, z) = V_0 \delta(r - r_0) \left[ \delta \left( \frac{2\pi z}{C} - \phi \right) + \delta \left( \frac{2\pi z}{C} - \phi + \pi \right) \right] \quad (2.33)$$

and the scattering amplitude

$$F(R, \Phi, l) = r_0 V_0 J_l(2\pi r_0 R) \left( \exp \left[ i \left( \Phi + \frac{\pi}{2} \right) l \right] + \exp \left[ i \left( \Phi - \frac{\pi}{2} \right) l \right] \right)$$

$$= r_0 V_0 J_l(2\pi r_0 R) (1 + \exp[-i\pi l]) \exp \left[ i \left( \Phi + \frac{\pi}{2} \right) l \right] \quad (2.34)$$

The intensity distribution becomes

$$I(R, \Phi, l) = |F(R, \Phi, l)|^2 = \begin{cases} 4r_0^2 V_0^2 (J_l(2\pi r_0 R))^2 & , l = \text{even} \\ 0 & , l = \text{odd} \end{cases} \quad (2.35)$$

All layer lines with odd index  $l$  disappear.

For an object with  $N$ -fold rotational symmetry, all layer lines disappear except those, whose index is a multiple of  $N$ .

### 2.2.3 Electron diffraction from a nanotube

The structure factor of a nanotube with radius  $r_0$ , whose atoms are located on discrete points on a helix with radius  $r_0$ , is given by:

$$F(R, \Phi, l) = \sum_{\nu} \exp \left[ i\nu \left( \Phi + \frac{\pi}{2} \right) \right] J_{\nu}(2\pi r_0 R) \sum_j f_j \exp \left[ i \left( -\nu \phi_j + \frac{2\pi l z_j}{c} \right) \right] \quad (2.36)$$

where the summation over  $j$  passes through all atoms of a unit cell and  $\nu$  through all integers, which are allowed by the selection rule (see section 2.2.4).

The structure factor can also be written as:

$$F(R, \Phi, l) = \sum_{\nu} B_{\nu}(R, \Phi) T_{\nu l} \quad (2.37)$$

with

$$B_{\nu}(R, \Phi) = \exp \left[ i \nu \left( \Phi + \frac{\pi}{2} \right) \right] J_{\nu}(2\pi r_0 R) \quad (2.38)$$

and

$$T_{\nu l} = \sum_j f_j \exp \left[ 2\pi i \left( \frac{\nu x_j}{A} + \frac{l z_j}{c} \right) \right] \quad (2.39)$$

Here  $A$  describes the perimeter of the tube and  $(x_j, z_j)$  the coordinates of the atoms in the radial projection in horizontal and axial direction. The diffraction effects of a nanotube can be seen more clearly by looking at the physical meaning of the two terms in equation 2.37:

- The structure factor in radial projection is given by  $T_{\nu l}$ . This term generates the typical hexagonal diffraction pattern of graphene.

- The function  $B_\nu(R, \Phi)$  takes the cylindrical curvature into account. The modifying Bessel function shifts the diffraction peaks in the diffraction image, whereas the shift depends on the order of the Bessel function.

### 2.2.4 Selection rule

For a discrete distribution of scatterers, which are located on a helix, the scattering potential can be written as the product of a continuous helix and a set of equally spaced planes with distance  $\Delta$ . The Fraunhofer diffraction can be calculated by convolution of the structure factor of the continuous helix and the equally spaced planes [4]. Since the structure factor of the planes consists of points located along the tube axis with equal spacing  $1/\Delta$ , the result is a set of diffraction patterns of single continuous helices, whose particular origin lies in the points along the axis. With  $c$  characterizing the new structural period along the axis of a single helix and  $C$  describing the pitch length of a continuous helix, an allowed reflection on layer line  $l$  has to fulfill the following relation:

$$\frac{l}{c} = \frac{\nu}{C} + \frac{\mu}{\Delta} \quad (2.40)$$

with  $\nu, \mu \in \mathbb{Z}$ . For a given layer line  $l$ , the allowed orders of the Bessel function  $J_\nu(2\pi r_0 R)$  are determined by the combinations of  $\nu$  and all possible integers  $\mu$ , which fulfill equation 2.40. The selection rule can also be written as

$$l = \nu t + \mu p \quad (2.41)$$

where  $t = c/C$  describes the number of turns per unit periodicity and  $p = c/\Delta$  the number of scattering objects per complete periodicity of the helix.

Also from the geometry in radial projection follows:

$$C = A \tan(\alpha) = a_0 \frac{m\sqrt{3(n^2 + m^2 + nm)}}{2n + m} \quad (2.42)$$

$$\Delta = a_0 \sin(\alpha) = a_0 \frac{3m}{2\sqrt{3(n^2 + m^2 + nm)}}$$

Expressed by  $(n, m)$  the parameter  $t$  is given by

$$t = \frac{c}{C} = \frac{2n + m}{Mm} \quad (2.43)$$

where  $M$  is the greatest common divisor of  $(2n + m)$  and  $(n + 2m)$ . The parameter  $p$  is given by:

$$p = \frac{c}{\Delta} = \frac{2(n^2 + m^2 + nm)}{Mm} \quad (2.44)$$

The selection rule for a nanotube  $(n, m)$  can then be written as

$$l = \nu \frac{2n + m}{Mm} + \mu \frac{2(n^2 + m^2 + nm)}{Mm} \quad (2.45)$$

The same selection rule holds for a tube, which possesses rotational symmetry, if  $c$  is defined as the periodicity of a special helix. The additional rotational symmetry leads to erasure of layer lines. For a nanotube with  $N$ -fold rotational symmetry only layer lines with index  $l = kN$  are valid ( $k \in \mathbb{Z}$ ). This supplemental condition can be added to the selection rule. Using the structural periodicity, the new periodicity is divided by  $N$  and is given by  $c/N$ . The selection rule  $l = \nu t + \mu p$  permits only multiples of  $N$  for  $\nu$  and  $\mu$ , whereas  $l$  may assume all possible integers.

### 2.2.5 Structure factor of a carbon nanotube

To calculate the scattering amplitude of a carbon nanotube  $(n, m)$ , it is practicable to describe the atomic structure by  $m$  pairs of atomic helices located at  $(x_j^{(1,0)}, z_j^{(1,0)})$  and  $(x_j^{(1,1)}, z_j^{(1,1)})$ . These positions are

$$\begin{aligned} x_j^{(1,0)} &= -ja_0 \cos(30^\circ - \alpha) \\ z_j^{(1,0)} &= ja_0 \sin(30^\circ - \alpha) \\ \text{with } j &= 0, 1, 2, \dots, m - 1 \end{aligned} \quad (2.46)$$

respectively

$$x_j^{(1,1)} = x_j^{(1,0)} + \frac{a_0}{\sqrt{3}} \cos(30^\circ + \alpha) \quad (2.47)$$

$$z_j^{(1,1)} = z_j^{(1,0)} - \frac{a_0}{\sqrt{3}} \sin(30^\circ + \alpha)$$

$$\text{with } j = 0, 1, 2, \dots, m - 1 \quad (2.48)$$

The scattering amplitude of  $m$  pairs of helices is then

$$\begin{aligned}
T_{\nu l} &= \sum_k^{\text{atoms}} f \exp \left[ 2\pi i \left( \frac{\nu x_k}{A} + \frac{l z_k}{c} \right) \right] \\
&= f \sum_{j=0}^{m-1} \exp \left[ 2\pi i \left( \frac{\nu x_j^{(1,0)}}{A} + \frac{l z_j^{(1,0)}}{c} \right) \right] \\
&\times \left( 1 + \exp \left[ \frac{2\pi i a_0}{\sqrt{3}} \left( \frac{\nu \cos(30^\circ + \alpha)}{A} - \frac{l \sin(30^\circ + \alpha)}{c} \right) \right] \right)
\end{aligned} \tag{2.49}$$

Setting

$$\cos(30^\circ - \alpha) = \frac{\sqrt{3}(n+m)}{2\sqrt{n^2+m^2+nm}} \tag{2.50}$$

$$\sin(30^\circ - \alpha) = \frac{n-m}{2\sqrt{n^2+m^2+nm}}$$

$$\cos(30^\circ + \alpha) = \frac{\sqrt{3}n}{2\sqrt{n^2+m^2+nm}} \tag{2.51}$$

$$\sin(30^\circ + \alpha) = \frac{2n+m}{2\sqrt{n^2+m^2+nm}}$$

and the selection rule

$$\frac{l}{c} = \frac{\nu}{C} + \frac{\mu}{\Delta} = \frac{1}{a_0} \left( \frac{\nu}{\sqrt{n^2+m^2+nm}} \frac{2n+m}{\sqrt{3}m} + \mu \frac{2\sqrt{n^2+m^2+nm}}{\sqrt{3}m} \right) \tag{2.52}$$

into equation 2.49, we get:

$$\begin{aligned}
T_{\nu l} &= f \sum_{j=0}^{m-1} \exp \left[ 2\pi i \left( \frac{\nu x_j^{(1,0)}}{A} + \frac{l z_j^{(1,0)}}{c} \right) \right] \\
&\quad \times \left( 1 + \exp \left[ 2\pi i \left( -\frac{\nu + (n+2m)\mu}{3m} \right) \right] \right) \\
&= f \sum_{j=0}^{m-1} \exp \left[ 2\pi i j \frac{\nu + (n+m)\mu}{m} \right] \left( 1 + \exp \left[ 2\pi i \left( -\frac{\nu + (n+2m)\mu}{3m} \right) \right] \right) \\
&= f \frac{1 - \exp[2\pi i(\nu + (n+m)\mu)]}{1 - \exp[2\pi i(\nu + (n+m)\mu)/m]} \left( 1 + \exp \left[ 2\pi i \left( -\frac{\nu + (n+2m)\mu}{3m} \right) \right] \right) \\
&= \begin{cases} mf \left( 1 + \exp \left[ 2\pi i \left( -\frac{\nu + (n+2m)\mu}{3m} \right) \right] \right) & , \text{ if } (\nu + (n+m)\mu)/m = N \\ 0 & , \text{ else} \end{cases}
\end{aligned} \tag{2.53}$$

The structure factor can be written as

$$F_{nm}(R, \Phi, l) = \sum_{\nu, \mu} f \chi_{nm}(\nu, \mu) \psi_{nm}(\nu, \mu) J_{\nu}(\pi dR) \exp \left[ i\nu \left( \Phi + \frac{\pi}{2} \right) \right] \tag{2.54}$$

whereas

$$\chi_{nm}(\nu, \mu) = 1 + \exp \left[ 2\pi i \left( -\frac{\nu + (n+2m)\mu}{3m} \right) \right] \tag{2.55}$$

and

$$\psi_{nm}(\nu, \mu) = \begin{cases} m, & \text{ if } (\nu + (n+m)\mu)/m = N \\ 0, & \text{ else} \end{cases} \tag{2.56}$$

holds. The parameters  $\nu$ ,  $\mu$ ,  $l \in \mathbb{Z}$  are determined by the selection rule for the carbon nanotube  $(n, m)$ :

$$l = \frac{(2n+m)\nu + 2(n^2 + m^2 + nm)\mu}{Mm} \tag{2.57}$$

Equations 2.56 and 2.57 confine the possible values of the parameter  $\nu$ , which defines the orders of the Bessel functions of layer line  $l$ .

Above equations are valid for X-ray radiation as well, if  $V(\vec{r})$  is substituted by the electron density function  $\rho(\vec{r})$  and  $f$  by the atomic scattering amplitude for X-ray radiation  $f^x$  [4].

### 2.2.6 Cylindrical correction

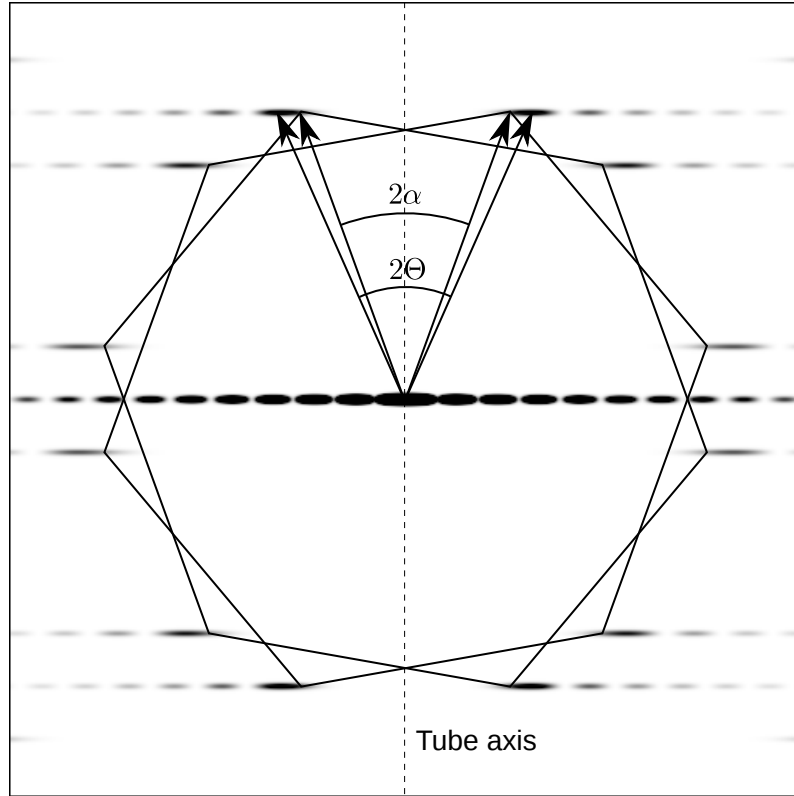


Figure 2.2: Comparison of the measured angle  $\Theta$  in the diffraction pattern and the actual helical angle  $\alpha$ . The cylindrical curvature causes an increase of the aperture angle  $\Theta$  (image adapted from [4]).

As can be seen in equation 2.37, the diffraction of a cylindrical tube differs from the one of the plane radial projection, which is the graphene lattice, due to the presence of the Bessel function. As a result of the cylindrical curvature and the small diameter of the nanotube the graphene reflections become lines in the direction perpendicular to the tube axis. Measuring the angle  $\Theta$  between the graphene (01)-reflections and the tube axis, the angle is larger than the true tilt angle of the helix (cf. figure 2.2). To understand the effect of the geometry of a cylindrical nanotube, here, without loss of generality, a single helix of scattering objects is assumed. In this case, the diffraction intensity on layer line  $\nu$  is proportional to  $|J_\nu(2\pi r_0 R)|^2$ . In radial projection the helix is the diagonal of a rectangle with width  $A$  and height  $C$ . The relation between the angle  $\Theta$ , measured in the experimental diffraction image, and the true helical angle  $\alpha$  is given by [5]:

$$\tan(\Theta) = \frac{R_\nu}{\nu/C} \quad (2.58)$$

Using

$$\frac{R_\nu}{\nu/C} = 2\pi r_0 R_\nu \frac{C}{2\pi r_0 \nu} = \frac{u_\nu}{\nu} \tan(\alpha) \quad (2.59)$$

one gets the relation between the experimental angle  $\Theta$  and the true angle  $\alpha$ :

$$\tan(\Theta) = \frac{u_\nu}{\nu} \tan(\alpha) \quad (2.60)$$

where  $u_\nu$  denominates the first maximum of the Bessel function  $J_\nu(m)$  for  $m \neq 0$ . The shift for  $\nu = 1$  is about 80% and for  $\nu = 2$  about 50%. The size of the correction factor shows, that the cylindrical correction may not be omitted.

### 2.2.7 Multi-walled nanotubes

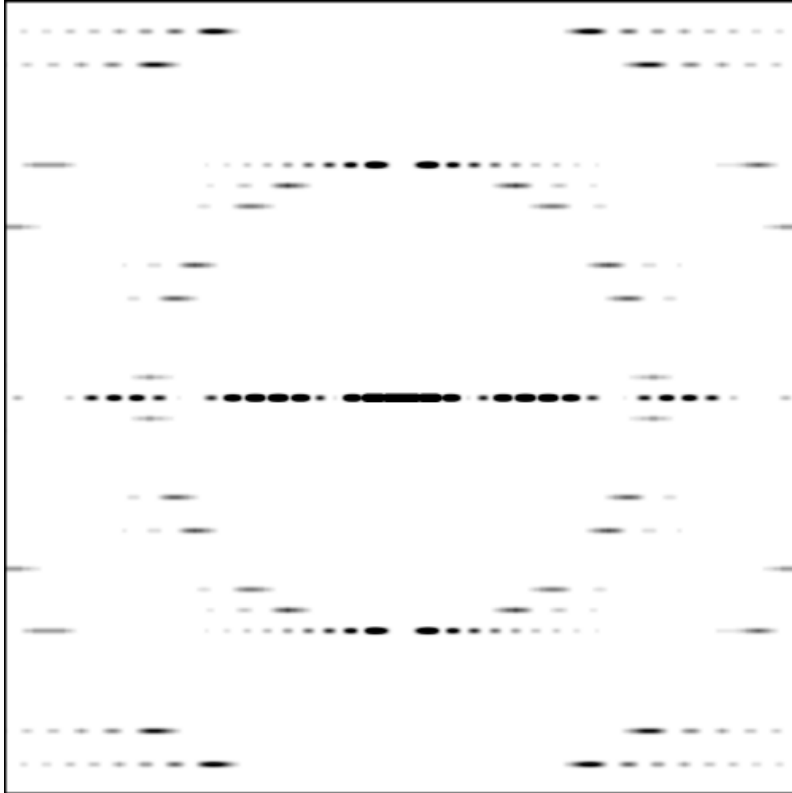


Figure 2.3: Simulated diffraction pattern of a double-walled carbon nanotube. The helical indices of the shells are (30, 3) and (15, 11).

An ideal multi-walled carbon nanotube consists of multiple concentric shells, whereas

the distance between the tubes is roughly the distance between graphite layers ( $\approx 0,335$  nm). The structure factor of a multi-walled nanotube with  $N$  shells can be written as the coherent sum of the scattering amplitudes of each single shell of the multi-walled nanotube [6]:

$$F(R, \Phi, Z) = \sum_{j=1}^N f \delta \left( Z - \frac{l_j}{c_j} \right) \sum_{\nu, \mu} \chi_j(\nu, \mu) \psi_j(\nu, \mu) J_\nu(\pi d_j R) \quad (2.61)$$

$$\times \exp \left[ i \nu \left( \Phi + \frac{\pi}{2} \right) \right] \exp [i \varphi_j]$$

where  $j$  describes the  $j$ th nanotube  $(n_j, m_j)$  with axial periodicity  $c_j$  and diameter  $d_j$ . The angle  $\varphi_j$  denotes the phase shift of the  $j$ th tube with respect to the reference shell in real space. The parameters  $\chi_j(\nu, \mu)$  and  $\psi_j(\nu, \mu)$  are given by the following relation:

$$\chi_j(\nu, \mu) = 1 + \exp \left[ -2\pi i \frac{\nu + (n_j + 2m_j)\mu}{3m_j} \right] \quad (2.62)$$

$$\psi_j(\nu, \mu) = \frac{1 - \exp \left[ -2\pi i (\nu + (n_j + m_j)\mu) \right]}{1 - \exp \left[ -2\pi i \frac{(n_j + m_j)\mu}{m_j} \right]} = \begin{cases} m_j & , \text{ if } \frac{\nu + (n_j + m_j)\mu}{m_j} \in \mathbb{Z} \\ 0 & , \text{ else} \end{cases} \quad (2.63)$$

where  $\nu$ ,  $\mu$  and  $l_j$  take all values, which are allowed by the selection rule of the  $j$ th shell of the nanotube:

$$l_j = \frac{(2n_j + m_j)\nu + 2(n_j^2 + m_j^2 + n_j m_j)\mu}{M_j m_j} \quad (2.64)$$

The greatest common divisor of  $(n_j + 2m_j)$  and  $(2n_j + m_j)$  is called  $M_j$ . The intensity distribution of the electron diffraction is  $I(R, \Phi, Z) = |F(R, \Phi, Z)|^2$ . A simulated diffraction pattern of a double-walled carbon nanotube is shown in figure 2.3. The electron diffraction of a single-walled nanotube is simply a special case of these equations.

## 2.3 Determination of the chiral indices of carbon nanotubes

The chiral indices of a nanotube can be determined by measuring the diameter  $d$  in a real space image of the tube and reading out the chiral angle  $\alpha$  from a diffraction pattern. Since this method has some drawbacks, a technique is described here, which uses the distances of the layer lines to the equatorial line [9] to evaluate the chiral indices.

### 2.3.1 Principal layer lines

For given chiral indices  $(n, m)$ , which determine the diameter and the helicity, the atomic structure of the carbon nanotube is also known. If a Transmission Electron Microscope (TEM) is used, the diameter is usually measured directly in the real space image. The helicity is derived from the diffraction pattern. As described above, the primary graphene reflections are the brightest intensity peaks (see figure 2.4). These reflections form three pairs of layer lines, called  $l_1$  (generated by the graphene-(01)-reflections),  $l_2$  (generated by the  $(\bar{1}0)$ -reflections) and  $l_3$  (generated by the (11)-reflections). The distances between these layer lines and the equatorial line are denominated  $D_1$ ,  $D_2$  and  $D_3$ . These are used to characterize the structure of the nanotube.

### 2.3.2 Direct method

It is important to notice that the diffraction intensity on a specific layer line is dominated by only one order of the Bessel function, although the scattering amplitude is described by summation of multiple orders of Bessel functions. All other orders contribute insignificantly to the intensity. This can be deduced from the selection rule. With respect to the constraints, which arise from the selection rule, all possible values for  $\nu$  of a layer line  $l$  have to fulfill [8]:

$$\nu = \nu_0 + \frac{2P(n^2 + m^2 + nm)}{M} \quad (2.65)$$

with  $P \in \mathbb{Z}$ . The smallest positive value  $\nu$  of a layer line  $l$  is called  $\nu_0$ . Mostly

$$(n^2 + m^2 + nm)/M \gg 1 \quad (2.66)$$

is valid [4]. Due to the fact that the magnitude of the maxima of the Bessel function

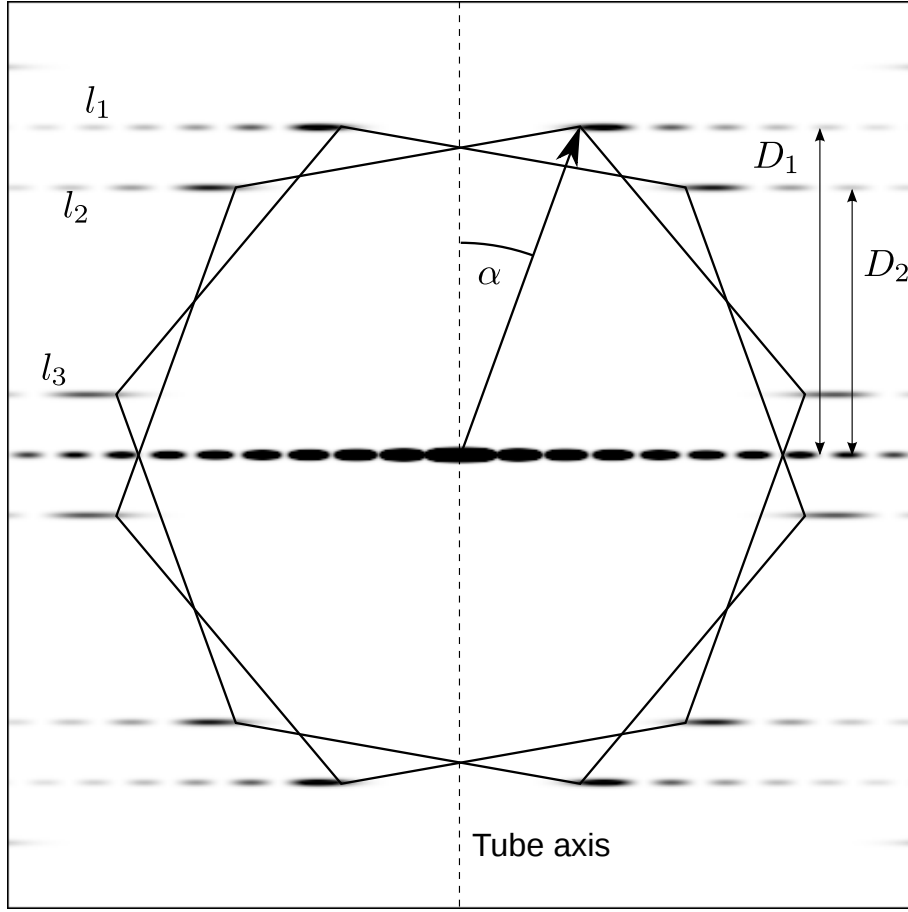


Figure 2.4: Schematic illustration of a diffraction pattern of a nanotube with helical angle  $\alpha$ . The graphene reflections are broadened perpendicular to the tube axis and form the layer lines  $l_i$ . The distances between the layer lines and the equatorial line are denominated  $D_i$ . They are independent of the cylindrical curvature.

decreases significantly with increasing order, the diffraction intensity of a specific layer line is mainly dominated by a Bessel function of the lowest order  $\nu_0$ . For example for a (14, 9) nanotube (diameter  $d = 1.572$  nm and helicity  $\alpha = 22.85^\circ$ ) the lowest possible order is  $\nu_0 = 9$  for layer line  $l_1$  ( $l = 37$ ). The next allowed order is  $\nu = -797$ . With  $x_\nu^{(1)}$  denoting the first maximum of the Bessel function  $J_\nu(x)$ , following inequation is valid:  $|J_9(x_9^{(1)})|^2 \geq 20|J_{-797}(x_{-797}^{(1)})|^2$  and  $x_9^{(1)} \approx 75x_{-797}^{(1)}$ . Therefore the diffraction intensity in the region where significant experimental data can be measured for a (14, 9) nanotube on layer line  $l = 37$  is only given by  $|J_9(x)|^2$ . The orders of the dominating Bessel functions for a given nanotube  $(n, m)$  can be determined by considering the crystallographic indices of the graphene reflections using the extended cell of the nanotube in radial projection which is related to the index  $\nu$ . In the Fraunhofer diffraction pattern the allowed Bragg reflections are

described by

$$\vec{g} = h\vec{a}_1^* + k\vec{a}_2^* \quad (2.67)$$

with  $h, k \in \mathbb{Z}$ . For a given nanotube with chiral indices  $(n, m)$  the reflections can be indexed by the crystallographic indices  $(\nu, l)$ , which are related to the radial projection lattice. Therefore the selection rule should be formed in such a way that the reflection

$$\vec{G} = \nu\vec{A}^* + l\vec{B}^* \quad (2.68)$$

indexed by the radial projection lattice, coincidences with the reciprocal lattice vector  $\vec{g}$ , indexed by the graphene lattice. The vectors  $\vec{A}^*$  and  $\vec{B}^*$  denote the basis vectors of the reciprocal lattice on the radial projection net (a rectangle with sides  $\vec{A}$  and  $\vec{B}$ ):

$$\begin{aligned} \vec{A}^* &= \frac{1}{n^2 + m^2 + nm}(n\vec{a}_1 + m\vec{a}_2) \\ \vec{B}^* &= \frac{1}{n_c^2 + m_c^2 + n_cm_c}(n_c\vec{a}_1 + m_c\vec{a}_2) \end{aligned} \quad (2.69)$$

The selection rule can be expressed as

$$\vec{G} = \vec{g} \quad (2.70)$$

or

$$\nu\vec{A}^* + l\vec{B}^* = h\vec{a}_1^* + k\vec{a}_2^* \quad (2.71)$$

Multiplying both sides of equation 2.71 with  $\vec{a}_1$ , we get

$$\nu\vec{A}^* \cdot \vec{a}_1 + l\vec{B}^* \cdot \vec{a}_1 = h \quad (2.72)$$

or equivalent

$$\frac{\nu a \cos(\alpha)}{A} - lB^* \sin(\alpha) = h \quad (2.73)$$

Using (figure 2.5)

$$lB^* = g \sin(\beta - \alpha) \quad (2.74)$$

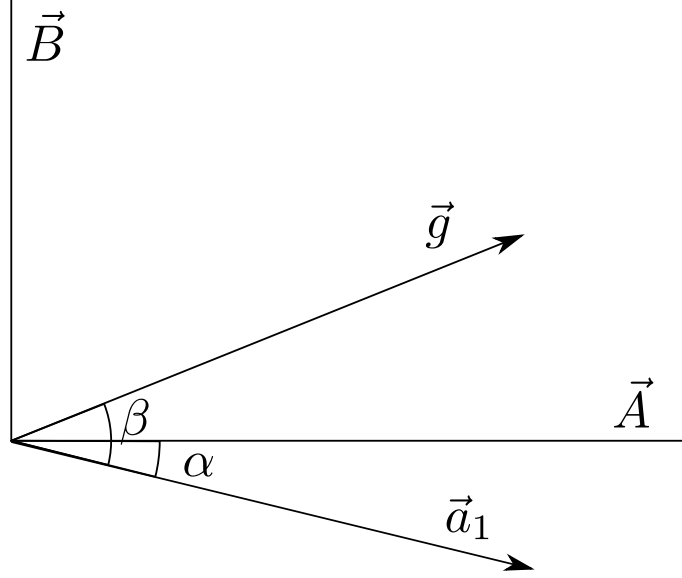


Figure 2.5: Schematic illustration of the radial projection of a carbon nanotube.  $\vec{a}_1$  describes the basis vector and  $\vec{g}$  the vector of the observed reflection. The vector  $\vec{A}$  denotes the perimeter,  $\vec{B}$  the axis. The helical angle is called  $\alpha$  and the angle between the basis vector  $\vec{a}_1$  and  $\vec{g}$  is called  $\beta$  (image adapted from [4]).

with  $\beta$  denoting the angle between the basis vector  $\vec{a}_1$  and the examined graphene reflection  $(hk)$ , we get the following relation [7]:

$$\nu = hn + km \quad (2.75)$$

As shown in figure 2.4, the principal layer lines  $l_1$ ,  $l_2$  and  $l_3$  are formed by the graphene reflections  $(01)$ ,  $(\bar{1}0)$  and  $(11)$ . Choosing the graphene reflection  $(01)$ , i.e.  $h = 0$  and  $k = 1$ , the order of the dominating Bessel function is

$$\nu = m \quad (2.76)$$

For the reflection  $(\bar{1}0)$  the order is

$$\nu = -n \quad (2.77)$$

and for the  $(11)$  reflection

$$\nu = n + m \quad (2.78)$$

Therefore the orders of the dominating Bessel functions of the three principal layer lines are  $m$ ,  $-n$  and  $n + m$ .

Using the chiral indices  $(n, m)$  the intensities on the three principal layer lines, denoted  $l_1$ ,  $l_2$  and  $l_3$ , are given by

$$I_{l_1}(R) \propto |J_m(\pi dR)|^2 \quad (2.79)$$

$$I_{l_2}(R) \propto |J_n(\pi dR)|^2 \quad (2.80)$$

and

$$I_{l_3}(R) \propto |J_{n+m}(\pi dR)|^2 \quad (2.81)$$

The order  $\nu$  of a Bessel function can also be determined by the positions of the maxima, which are unique for each Bessel function. An efficient method to obtain the order of a Bessel function  $J_N(X)$  is to measure the ratio  $X_2/X_1$  of the first two maxima at positions  $X_1$  and  $X_2$  or an arbitrary pair of maxima. With known orders of the Bessel functions the chiral indices  $n$  and  $m$  can be identified directly. Therefore the chiral indices  $(n, m)$  can be obtained by the distribution of the diffraction intensity on layer lines  $l_1$  and  $l_2$ , whose intensities are proportional to  $|J_m(\pi dR)|^2$  respectively  $|J_n(\pi dR)|^2$ . The ratio of the peak positions  $R_1/R_2 = X_1/X_2$  is independent of the settings of the used electron microscope. However the peak positions change with the angle between the incidence electron beam and the tube axis.

For non-helical nanotubes, i.e. “zigzag” and “armchair” nanotubes with chiral indices  $(n, 0)$  respectively  $(n, n)$ , the layer lines overlap. For a “zigzag” nanotube with indices  $(n, 0)$  the layer lines  $l_2$  and  $l_3$  coincide. The intensity distribution of the first layer line  $l_1$  is proportional to  $|J_0(\pi dR)|^2$ , whereas the second layer line  $l_2$  is proportional to  $|J_n(\pi dR)|^2$ . For an “armchair” nanotube  $(n, n)$  the first layer line  $l_1$  and the second layer line  $l_2$  overlap with an intensity proportional to  $|J_n(\pi dR)|^2$ . The third layer line  $l_3$  coincides with the equatorial line.

### 2.3.3 Ratio of indices $m/n$

Due to the periodicity of the atomic structure of a carbon nanotube  $(n, m)$  in axial direction, the layer lines are sharp, so that the distances  $D_1$ ,  $D_2$  and  $D_3$  between the layer lines and the equatorial line can be measured easily and exactly in the diffraction image. Even though the cylindrical curvature causes a significant deformation of the hexagonal diffraction pattern, the distances of the layer lines do not change. The axial distances between the reflections and the equatorial line, which

are equal to the distances of the layer lines, are obtained by the use of trigonometrical relations:

$$D_1 = a^* \sin(90^\circ - \alpha) = a^* \cos(\alpha) \quad (2.82)$$

$$D_2 = a^* \sin(30^\circ + \alpha) \quad (2.83)$$

$$D_3 = a^* \cos(30^\circ - \alpha) \quad (2.84)$$

Then the helical angle  $\alpha$  can be deduced from the ratios of the layer line distances [9]:

$$\alpha = \tan^{-1} \left( \frac{2D_2 - D_1}{\sqrt{3}D_1} \right) \quad (2.85)$$

The ratio of the chiral indices  $m$  and  $n$  is given by:

$$\frac{m}{n} = \frac{2D_2 - D_1}{2D_1 - D_2} \quad (2.86)$$

This method has advantages over the method described above:

- The ratio is independent of the angle between the incident electron beam and the nanotube axis.
- Even for a low signal to noise ratio, the distances can often be measured.
- The method is independent of the tube length of the electron microscope.

The disadvantage of this technique is its ambiguity, because nanotubes with different indices can possess the same ratio.

## 2.4 Symmetry of the electron diffraction from single-walled carbon nanotubes

When the tube axis is perpendicular to the incident electron beam, the axis is located in the diffraction plane, which intersects the reciprocal space of the nanotube. Under normal incidence the cutting edge (figure 2.6 right) passes through the center of concentric corona, which depict the diffraction intensities. Along this line the contributing Bessel functions  $\nu$  are either even or odd [8]. The intensity distribution (cf. equation 2.54) depends on the angle  $\Phi$  and fulfills the following equation [8]:

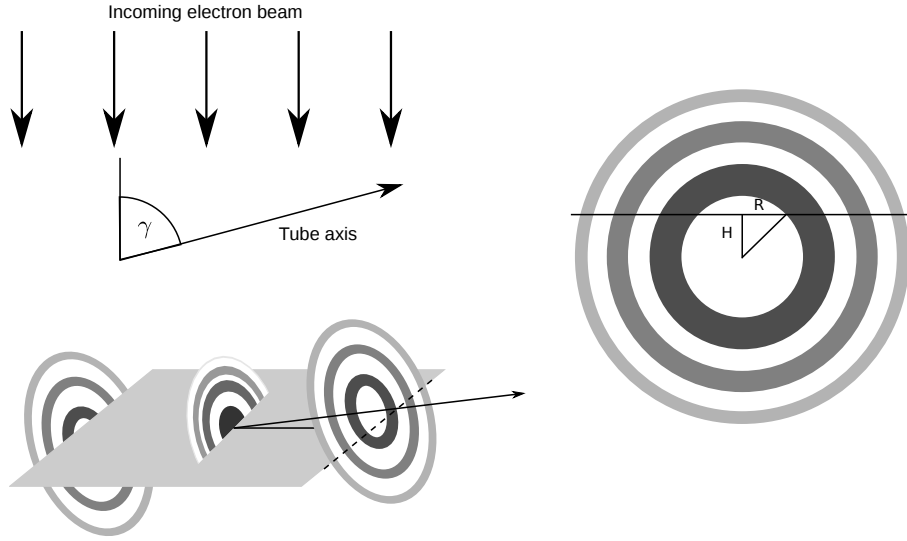


Figure 2.6: *Top left:* The tilt angle between the tube axis and the incoming electron beam is named  $\gamma$ . *Bottom left:* The corresponding relation in the reciprocal space, where the diffraction intensities, caused by the nanotube, are described by equidistant concentric rings around the tube axis. *Right:* View on a set of rings: The horizontal line is the intersection line with the diffraction plane. With decreasing angle  $\gamma$  the distance  $R$  of the intensity peaks to the tube axis increases. The vertical distance of the intersection line to the diffraction rings is called  $H$  (image adapted from [8]).

$$I(R, \Phi + \pi, l) = I(R, \Phi, l) \quad (2.87)$$

This holds for all layer lines of the diffraction pattern. This equation shows that the electron diffraction of a carbon nanotube is mirror symmetric due to the tube axis. Together with Friedel's Law this shows, that the electron diffraction pattern of a single-walled carbon nanotube under perpendicular incidence has always  $2mm$  symmetry [8].

When the incoming beam is not normal on the tube axis, i.e.  $\gamma \neq 90^\circ$ , the tube axis in the reciprocal space does not lie in the diffraction plane of the nanotube, even though it passes through the center of the central diffraction corona. The intersection points with the diffused corona, which represent the diffraction intensities, are related to the incidence angle  $\gamma$  and the positions of the layer line planes in reciprocal space. For inclined incidence the diffraction intensities on the layer line  $l$  are modulated by the same Bessel functions as for perpendicular incidence. The measured scattering amplitude in the diffraction plane is [8]:

$$F_{nm}(R, \Phi, l) = \sum_{\nu, \mu} f \chi_{nm}(\nu, \mu) \psi_{nm}(\nu, \mu) J_{\nu} \left( \pi d \sqrt{R^2 + \left( \frac{l \tan(90^\circ - \gamma)}{c} \right)^2} \right) \times \exp \left[ i n \left( \Phi + \frac{\pi}{2} \right) \right] \quad (2.88)$$

Since the intensity of the electron diffraction also fulfills equation 2.87, the complete electron diffraction image of a single-walled carbon nanotube under incline incidence possesses  $2mm$  symmetry.

Figure 2.7 shows a simulated electron diffraction pattern of a single-walled carbon nanotube (14, 9) under various tilt angles. When the tilt angle  $\gamma$  is decreased from  $90^\circ$  to  $80^\circ$ , the layer line peaks shift towards the tube axis. Simultaneously the layer line distances to the equatorial line increase by a factor  $1/\sin 80^\circ$ . When the tilt angle  $\gamma$  is decreased to  $70^\circ$ , the distance between the first peaks on the layer lines decrease further until they overlap at a critical angle  $\gamma_c = 90^\circ - \tan^{-1}((m_\nu/\nu)\tan(\alpha)) = 73.2^\circ$ , where  $m_\nu = 10.7$  describes the position of the first maximum of the Bessel function  $J_9(m)$ . When  $\gamma < \gamma_c$  the diffraction plane does not cross the first ring of the corona. The  $2mm$  of the diffraction image is preserved throughout the whole tilting process.

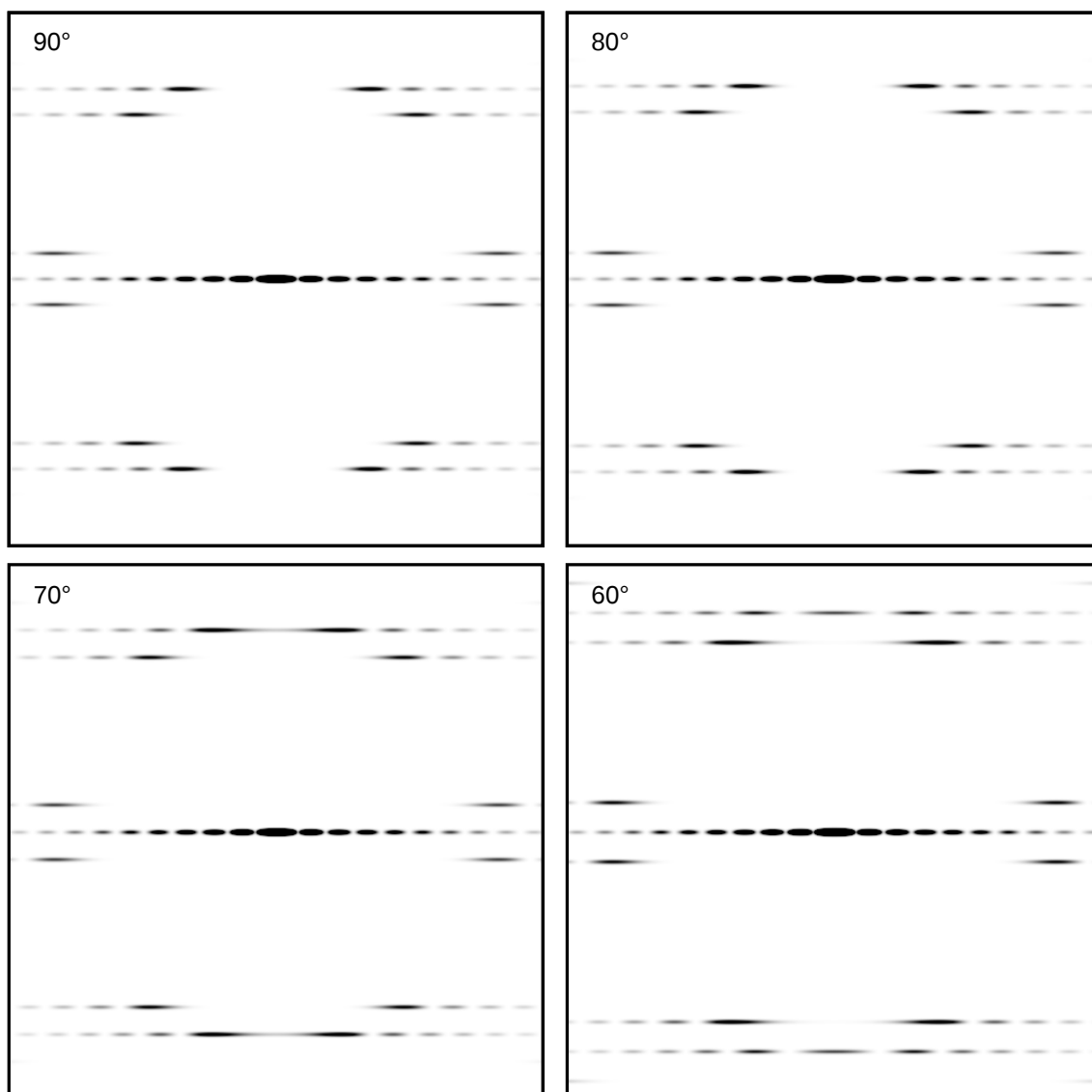


Figure 2.7: Simulated electron diffraction pattern of a single-walled carbon nanotube (14,9) under various incidence angles: a)  $\gamma = 90^\circ$ , b)  $\gamma = 80^\circ$ , c)  $\gamma = 70^\circ$  and d)  $\gamma = 60^\circ$ . The diffraction image changes under various angles, but the  $2mm$  symmetry is preserved.



# Chapter 3

## Auxiliary algorithms for the (pre)processing

### 3.1 Generalized Linear Least Squares

In order to estimate values at arbitrary points between a discrete set of points  $(x_i, y_i)$ , if the generating function of that discrete set is not known, it is often useful to approximate the underlying function globally or at least locally. This could be done by interpolation with a polynomial. This method however tends to develop strong unwanted oscillations between the data points. The reason for this behavior originates from a too tight binding of the interpolating function to the data points. Since every data point has to be matched by the function, noise, which is existent in all experimental data, leads to overfitting. For real, noisy data it is often more useful to minimize the quadratic error of the interpolating function with respect to the measured data. So one gets a function, which has the closest course to the data points in the sense of the mean square deviation. The Generalized Linear Least Squares (GLLS) algorithm offers a solution to this problem.

There are  $N$  data points  $(x_i, y_i)$  with their standard deviation  $\sigma_i$  given with respect to the  $y$ -axis. If  $M$  is the number of used basis functions and  $\Phi_k$  and  $a_k$  are the parameters to be estimated, we get the following ansatz for the approximating function:

$$y(x; a_1, \dots, a_M) = \sum_{k=1}^M a_k \Phi_k(x) \quad (3.1)$$

Usually for the basis functions an orthonormal system is used (for example polynomials with  $\Phi_1 = 1$ ,  $\Phi_2 = x$ ,  $\Phi_3 = x^2$ , ...).

To find the wanted coefficients  $a_k$ , the following cost function is introduced [11]:

$$\Xi^2 = \sum_{i=1}^N \left( \frac{y_i - \sum_{k=1}^M a_k \Phi_k(x_i)}{\sigma_i} \right)^2 \quad (3.2)$$

This equation complies with the quadratic error weighted with the standard deviations. One gets the wanted minimum of the cost function (cf. equation 3.2) by setting the partial derivatives to zero with respect to the  $a_k$ . This yields an under-determined system of equations  $M < N$  with  $M$  equations:

$$0 = \frac{\partial \Xi^2}{\partial a_k} = - \sum_{i=1}^N \frac{2}{\sigma_i^2} \left( y_i - \sum_{j=1}^M a_j \Phi_j(x_i) \right) \Phi_k(x_i), \quad k = 1, \dots, M \quad (3.3)$$

After algebraic transformation of the equation one gets:

$$\sum_{j=1}^M \sum_{i=1}^N \frac{a_j}{\sigma_i^2} \Phi_j(x_i) \Phi_k(x_i) = \sum_{i=1}^N \frac{y_i}{\sigma_i^2} \Phi_k(x_i), \quad k = 1, \dots, M \quad (3.4)$$

With

$$\mathbf{A} = \begin{pmatrix} \frac{\Phi_1(x_1)}{\sigma_1} & \dots & \frac{\Phi_M(x_1)}{\sigma_1} \\ \vdots & \ddots & \vdots \\ \frac{\Phi_1(x_N)}{\sigma_N} & \dots & \frac{\Phi_M(x_N)}{\sigma_N} \end{pmatrix}, \quad \tilde{\mathbf{b}} = \begin{pmatrix} \frac{y_1}{\sigma_1} \\ \vdots \\ \frac{y_N}{\sigma_N} \end{pmatrix}, \quad \tilde{\mathbf{a}} = \begin{pmatrix} a_1 \\ \vdots \\ a_M \end{pmatrix} \quad (3.5)$$

equation 3.4 can be written as a matrix equation [11]:

$$\begin{aligned} (\mathbf{A}^T \mathbf{A}) \vec{a} &= \mathbf{A}^T \tilde{\mathbf{b}} \\ \Rightarrow \vec{a} &= (\mathbf{A}^T \mathbf{A})^{-1} \mathbf{A}^T \tilde{\mathbf{b}} \end{aligned} \quad (3.6)$$

To yield an optimal parameter vector  $\vec{a}$ , in the sense of the mean quadratic error, a matrix inversion of  $(\mathbf{A}^T \mathbf{A})$  has to be performed. The matrix  $\mathbf{A}$  is called “design-matrix” and  $(\mathbf{A}^T \mathbf{A})^{-1} \mathbf{A}^T$  is the pseudo inverse, which is needed to solve the undetermined system of equations.

A manipulation of the shape of the approximating function is additionally possible by the standard deviations  $\sigma_i$ . Points with a relatively small standard deviation are approximated better, since they deliver a larger contribution to the error function.

### Regression of exponential function

However there are functions which cannot be described elegantly by a finite set of polynomials. An exponential decline represents such a case. The parameters  $b$  and  $c$  in function

$$y = b \exp(cx) \quad (3.7)$$

do not contribute linearly. To linearize the equation we can take the logarithm

$$\ln y = \ln b + cx \quad (3.8)$$

For this equation the ansatz (3.1) with  $\Phi_1 = 1$ ,  $\Phi_2 = x$  and  $a_1 = \ln b$ ,  $a_2 = c$  can be used. The parameters  $a_1$  and  $a_2$  then contribute linearly to the equation.

Looking at a non-squared summand of equation 3.2 with standard deviation  $\sigma_i = 1$  we get:

$$\xi_i = \ln y_i - (a_1 + a_2 x) \quad (3.9)$$

Now we want to have a look on the consequences of a disturbance  $\epsilon_i$  on  $y_i$ , which may be caused by noise. The disturbed value is  $\tilde{y}_i(\epsilon_i) = y_i + \epsilon_i$ . Using linear approximation for the error  $\xi_i$  at the point  $y_i$  leads to:

$$T_1(\tilde{y}_i(\epsilon_i)) = (\ln(y_i) - (a_1 + a_2 x)) + \frac{1}{y_i}(y_i - \tilde{y}_i) = (\ln(y_i) - (a_1 + a_2 x)) + \frac{1}{y_i}(\epsilon_i) \quad (3.10)$$

This means, that the effect of the disturbance  $\epsilon_i$  in the error function  $\xi_i$  depends on the value of  $y_i$ . In the linear approximation this dependency is  $1/y_i$ .

For additive noise the probability distribution for the intensity of the disturbance  $\epsilon_i$  is independent of the intensity of the measured value  $y_i$ . But in case of the factor  $1/y_i$  a disturbance is weighted more heavily for small measured values than for large ones. This leads to unwanted strong weighting of small values.

This effect can approximately be compensated by multiplying the error terms with the measured value, so that the factor  $1/y_i$  is neutralized:

$$\xi_i = y_i(\ln y_i - (a_1 + a_2 x)) \quad (3.11)$$

## 3.2 Snake algorithm

The active contour, also called “Snakes”, is a method in image processing to determine the contour of an object. It is called snakes, since the way it is fitting itself to the contour is similar to the movement of a snake. If the shape of an object is approximately known to initialize the algorithm, the active contour could be used to determine the exact borders of the object. This is realized by minimization of the sum of the so called “inner and outer energy”. The algorithm presented here is based on the work of Blair Mackiewich [12].

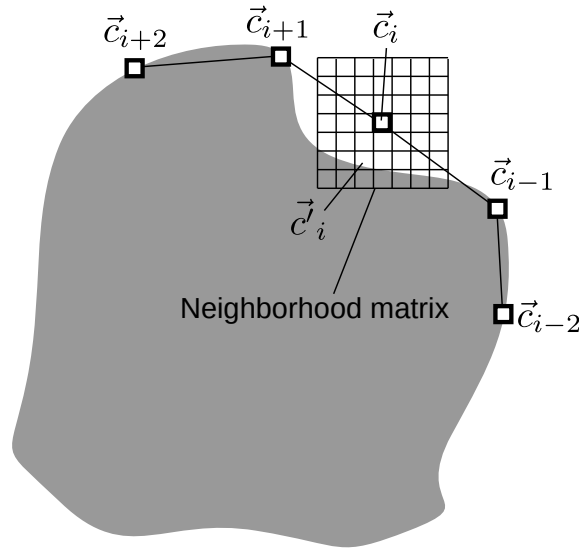


Figure 3.1: An example for the movement of a point  $\vec{c}_i$  of an active contour. At the point  $\vec{c}_i$  an energy minimum is located in cause of the high contrast (image adapted from [12]).

### 3.2.1 Overview

An active contour consists of an ordered set of  $n$  points in the image plane:

$$C = \{\vec{c}_1, \dots, \vec{c}_n\} \quad (3.12)$$

$$\vec{c}_i = (x_i, y_i), \quad i = 1, \dots, n$$

The points  $\vec{c}_i$  of the contour approach iteratively the border of the object by minimization of an energy function (cf. figure 3.1). For each point of the neighborhood of  $\vec{c}_i$  the following energy term is calculated [12]:

$$E_i = \alpha E_{int}(\vec{c}_i) + \beta E_{ext}(\vec{c}_i) \quad (3.13)$$

The inner energy  $E_{int}(\vec{c}_i)$  only depends on the shape of the contour, whereas the outer energy  $E_{ext}(\vec{c}_i)$  depends only on the properties of the image in the environment of  $\vec{c}_i$ . The constants  $\alpha$  and  $\beta$  weigh the energy terms relatively to each other.

The value in the center of the matrices  $E_i$ ,  $E_{int}$  and  $E_{ext}$  indicates the energy of the contour at the point  $\vec{c}_i$ . The other entries of the matrices correspond to the contour-energies of the points in the neighborhood of  $\vec{c}_i$  (cf. figure 3.1).

In each learning step a point of the contour is moved to the point  $\vec{c}_i$ , where the energy  $E_i$  has its minimum. The more appropriate the parameters of the energy function are chosen, the exacter the contour follows the object.

### 3.2.2 Inner energy

The assignment of the inner energy is to give a shape to the active contour and assure that the distances between points are similar. The used function for the inner energy is defined as follows [12]:

$$\alpha E_{int}(\vec{c}_i) = \omega_c E_{con}(\vec{c}_i) + \omega_b E_{bal}(\vec{c}_i) \quad (3.14)$$

The continuity energy  $E_{con}(\vec{c}_i)$  forces the contour to assume an ordered shape. The balloon energy  $E_{bal}(\vec{c}_i)$  takes a balloon force into account, which expands or shrinks the contour. The parameters  $\omega_c$  and  $\omega_b$  cause a relative weighting of the energy terms.

#### Continuity energy

Without other influences, the continuity energy forces an open contour to form a straight line. A closed contour is forced to take the shape of a circle. The energy of each element  $e_{jk}(\vec{c}_i)$  of the matrix  $E_{con}(\vec{c}_i)$  is defined by [12]

$$e_{jk}(\vec{c}_i) = \frac{1}{l(C)} |p_{jk}(\vec{c}_i) - \omega_\gamma(\vec{c}_{i-1} + \vec{c}_{i+1})|^2 \quad (3.15)$$

where  $p_{jk}(\vec{c}_i)$  denotes the point in the image, which corresponds spatially to the matrix entry  $e_{jk}(\vec{c}_i)$  and  $l(C)$  is the average distance of the nodes of  $C$ . For an open contour  $\omega_\gamma = 0.5$ . So the point with the lowest energy is located precisely in the center of  $\vec{c}_{i-1}$  and  $\vec{c}_{i+1}$ . In a closed contour  $C$  has a period of  $n$ , so that  $\vec{c}_{i+n} = \vec{c}_i$  is valid. In this case  $\omega_\gamma$  is given by

$$\omega_\gamma = \frac{1}{2 \cos\left(\frac{2\pi}{n}\right)} \quad (3.16)$$

Thereby the minimum of the energy  $E_{con}(\vec{c}_i)$  is pushed outwards, so that  $C$  becomes a circle (cf. figure 3.2).

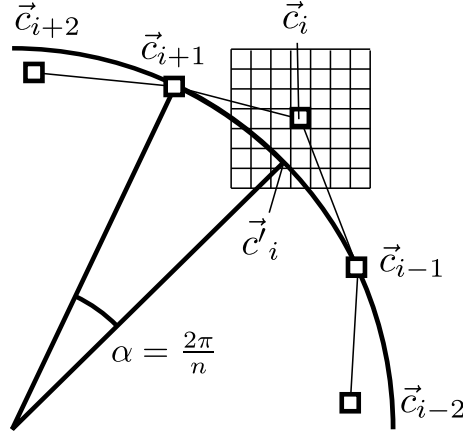


Figure 3.2: Influence of the continuity energy on the active contour: The energy minimum is located on a circle through  $\vec{c}_{i-1}$  and  $\vec{c}_{i+1}$  (image adapted from [12]).

The normalization factor  $l(C)$  in equation 3.15 is the average Euclidean distance between neighboring points of  $C$ :

$$l(C) = \frac{1}{n} \sum_{i=1}^n |\vec{c}_{i+1} - \vec{c}_i| \quad (3.17)$$

The normalization is needed to get an energy  $E_{con}(\vec{c}_i)$ , which is independent of the size of the contour, the position and the orientation.

### Balloon energy

To let the contour grow (or shrink) independently of external influences, a balloon force is used. If a contour is initialized inside a homogeneous region of an image, the balloon force causes a growing of the active contour until the borders of the region are reached. There the external forces start to influence the contour (cf. figure 3.3). A variable balloon force is used, which is indirectly proportional to the magnitude of the image gradient. Therefore the force is strong in homogeneous regions and weak in areas where edges or object boundaries are located.

The energy term of each element  $e_{jk}(\vec{c}_i)$  of the matrix  $E_{bal}(\vec{c}_i)$  is described by the following inner product:

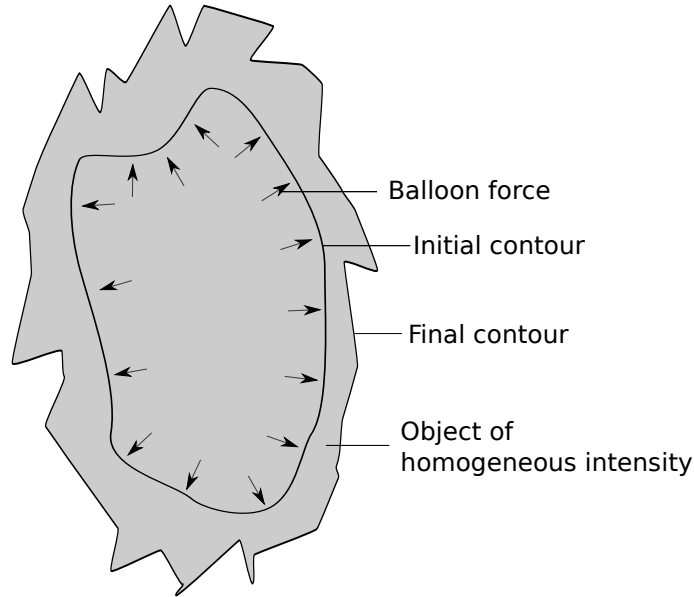


Figure 3.3: Movement of the active contour due to the balloon force: Inside an object with homogeneous intensity the balloon force pushes the contour towards the object boundaries (image adapted from [12]).

$$e_{jk}(\vec{c}_i) = \vec{n}_i \cdot (\vec{c}_i - p_{jk}(\vec{c}_i)) \quad (3.18)$$

Here  $\vec{n}_i$  denotes the outwards faced normal vector of  $C$  at the point  $\vec{c}_i$  and  $p_{jk}(\vec{c}_i)$  is the point in the environment of  $\vec{c}_i$ , which corresponds to the entry  $e_{jk}(\vec{c}_i)$  of the energy matrix. The balloon energy has its minimum at those points, which have the largest distances to  $\vec{c}_i$  in the direction of  $\vec{n}_i$ .

We get the normal vector  $\vec{n}_i$  by rotating the tangential vector by  $90^\circ$ , which is defined by:

$$t_i = \frac{\vec{c}_i - \vec{c}_{i-1}}{|\vec{c}_i - \vec{c}_{i-1}|} + \frac{\vec{c}_{i+1} - \vec{c}_i}{|\vec{c}_{i+1} - \vec{c}_i|} \quad (3.19)$$

So  $\vec{n}_i$  is the unit vector which is perpendicular to  $\vec{t}_i$ .

The balloon force can also be influenced by the gradient of the image (cf. section 3.2.4).

### 3.2.3 Outer energy

The outer energy function pushes the active contour towards the interesting features of an image like object boundaries. Each energy expression, which possesses this property, can be used.

The intensity and the gradient are characteristics, which can be observed easily. Therefore the energy function can be written as follows [12]:

$$\beta E_{ext}(\vec{c}_i) = \omega_m E_{mag}(\vec{c}_i) + \omega_g E_{grad}(\vec{c}_i) \quad (3.20)$$

The energy  $E_{mag}(\vec{c}_i)$  moves the contour to regions of higher or lower intensities and the energy  $E_{grad}(\vec{c}_i)$  to edges in the image. The parameters  $\omega_m$  and  $\omega_g$  weigh the energy terms relatively to each other.

### Intensity energy

Each point of the intensity matrix  $E_{mag}(\vec{c}_i)$  is set to the value of the intensity at the corresponding image point in the environment of  $\vec{c}_i$ :

$$e_{jk}(\vec{c}_i) = I(p_{jk}(\vec{c}_i)) \quad (3.21)$$

For a positive  $\omega_m$  the contour moves towards regions of high intensity, for negative  $\omega_m$  towards regions of low intensity.

### Gradient energy

The gradient energy pulls the contour to edges in the image. An energy term, which is proportional to the absolute value, shifts the contour towards an arbitrary edge:

$$e_{jk}(\vec{c}_i) = -|\nabla I(p_{jk}(\vec{c}_i))| \quad (3.22)$$

When an active contour is used to find object boundaries, an energy function is wanted, which can distinguish between edges of neighboring objects. A function, which regards the different directions of the gradients of the objects, offers this feature. Therefore the direction of the gradient of the object boundary should be similar to the direction of the normal vector of the contour (cf. figure 3.4).

The value of each element of the directed energy matrix of the gradient  $E_{grad}(\vec{c}_i)$  can therefore be written as the inner product of the normal vector of the contour and the image gradient:

$$e_{jk}(\vec{c}_i) = -\vec{n}_i \cdot \nabla I(p_{jk}(\vec{c}_i)) \quad (3.23)$$

where  $n_i$  denotes the normal vector of the contour at  $\vec{c}_i$  as defined above.

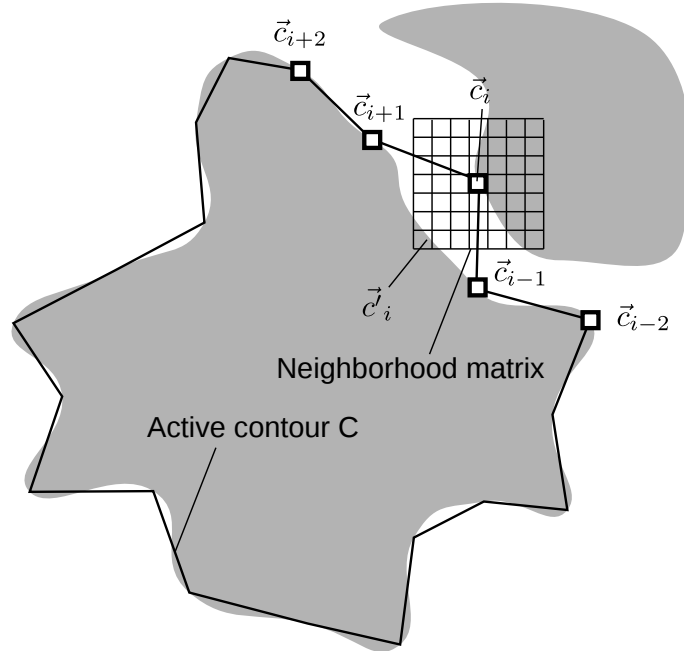


Figure 3.4: Movement of the contour due to the gradient energy: Since the direction of the gradient at the edge of the interesting object is similar to the direction of the normal vector of the contour, the algorithm moves the contour from  $\vec{c}_i$  to  $\vec{c}'_i$ , though the absolute value of the gradient at both points is the same (image adapted from [12]).

### 3.2.4 Normalizations

The energy functions introduced in the previous section are scaled, so that the neighborhood matrices contain comparable values.

The balloon energy is adjusted to the image gradient. To improve the robustness of the algorithm, furthermore normalization parameters are added to the intensity and gradient energy terms. This leads to the following changes for the energies [12]:

#### Continuity energy

At each point of the contour the elements of the neighborhood matrix of the continuity energy are scaled to the range  $[0, 1]$ .

$$e'_{jk}(\vec{c}_i) = \frac{e_{jk}(\vec{c}_i) - e_{\min}(\vec{c}_i)}{e_{\max}(\vec{c}_i) - e_{\min}(\vec{c}_i)} \quad (3.24)$$

Here  $e_{\min}(\vec{c}_i)$  respectively  $e_{\max}(\vec{c}_i)$  denote the smallest respectively largest entry of the matrix  $E_{con}(\vec{c}_i)$ .

**Balloon energy**

The balloon energy is scaled to the range  $[0, 1]$  and adjusted to the image gradient, whereupon  $|\nabla I|_{max}$  denotes the maximum absolute value of the gradient in the whole image:

$$e'_{jk}(\vec{c}_i) = \frac{e_{jk}(\vec{c}_i) - e_{min}(\vec{c}_i)}{e_{max}(\vec{c}_i) - e_{min}(\vec{c}_i)} \left( 1 - \frac{|\nabla I(\vec{c}_i)|}{|\nabla I|_{max}} \right) \quad (3.25)$$

**Intensity energy**

To regularize the intensity energy term, the parameter  $\omega_{\delta I}$  is added:

$$e'_{jk}(\vec{c}_i) = \frac{e_{jk}(\vec{c}_i) - e_{min}(\vec{c}_i)}{\max\{(e_{max}(\vec{c}_i) - e_{min}(\vec{c}_i)), \omega_{\delta I} \cdot I_{max}\}} \quad (3.26)$$

where  $I_{max}$  is the maximum intensity in the whole image and  $\omega_{\delta I}$  is in the range  $[0, \infty]$ . The sensitivity of the active contour to local fluctuations in the intensity is determined by  $\omega_{\delta I}$ .

**Gradient energy**

The gradient energy is regularized analogously to the intensity energy:

$$e'_{jk}(\vec{c}_i) = \frac{e_{jk}(\vec{c}_i) - e_{min}(\vec{c}_i)}{\max\{(e_{max}(\vec{c}_i) - e_{min}(\vec{c}_i)), \omega_{\delta G} \cdot G_{max}\}} \quad (3.27)$$

The parameter  $\omega_{\delta G}$  is in the range  $[0, \infty]$ . A large  $\omega_{\delta G}$  results in an active contour, which is insensitive to smooth edges.

# Chapter 4

## The analysis algorithm

The goal of this work was to develop an algorithm which is able to analyze electron diffraction patterns of carbon nanotubes automatically and to estimate the chiral indices. To evaluate the results such an algorithm achieves, it is necessary to compare the estimated chiral indices to the real chiral indices during the testing phase of the algorithm.

This can of course only be done, if the chiral indices are known. For the diffraction patterns available for this thesis, that is not the case (except for one pattern, which was also analyzed by hand cf. section 6.1).

Since the theory of electron diffraction from carbon nanotubes is well known (cf. chapter 2 and [4]) a program to simulate diffraction patterns was written. If a simulated image is analyzed, the results can be evaluated, since naturally the chiral indices of the simulated image are known.

Another advantage of simulated images is the fact, that the limitations of the algorithm can be tested. For example the influence of the noise amplitude, the distance between layer lines, the broadening of the lines, etc. can be reviewed. Special cases of the chiral indices (for example “armchair” and “zigzag” tubes) can be simulated as well as multi-walled tubes and bundles of tubes. The effort for such a simulation is less than the effort of taking a real image. And, of course, the number of tubes and the chiral indices cannot be chosen freely for real nanotubes.

In this chapter, the preprocessing steps and the actual analysis of a diffraction pattern are shown exemplified with a simulated image of a (15, 8) carbon nanotube.

## 4.1 Simulation of diffraction patterns

The simulation used is based on the theory in chapter 2 and the work of Phillippe Lambin and Luc Henrard [13].

Since the simulation is an idealized diffraction pattern it strongly differs from an experimentally taken diffraction image. Software, which is supposed to be able to analyze realistic images, should be tested with simulations, which are similar to experimental data. The steps which are necessary to adapt the simulation to the real situation are described in the following paragraphs.

### Layer line broadening

In theory the layer lines and the equatorial line are sharp in the direction of the tube axis, which is perpendicular to the equatorial line. In a real image this is not the case.

To adjust the simulation to real patterns, the simulated reflections are convoluted with a Gaussian function. The FWHM (full-width-half-maximum) of the used Gaussian function for the image in figure 4.1 amounts to 10 pixels.

### Intensity

The values of the intensities in the simulation have to be scaled to the range of the brightness of the image format. To scale the intensities in a way, that the maximum intensity corresponds to the maximum brightness is not practicable, because the highest intensity appears at the center of the equatorial line. But this point of the image is not interesting, because it is covered with the undiffracted electron beam or the beam stopper.

The intensity on the layer lines is of much more interest, hence the scale is calculated by setting the point of the highest intensity on the layer lines to a tunable fractional amount of the maximum brightness of the image.

### Undiffracted electrons

The theory only covers the diffracted electrons, but in reality the electrons pass the scattering object undiffracted for the most part. This causes an area of very high intensity in the center of the diffraction image. The intensity decreases with increasing distance to the center. This intensity caused by the undiffracted electrons is emulated in the simulation by a two-dimensional Gaussian function. The peak intensity and the standard deviation of this Gaussian function are tunable.

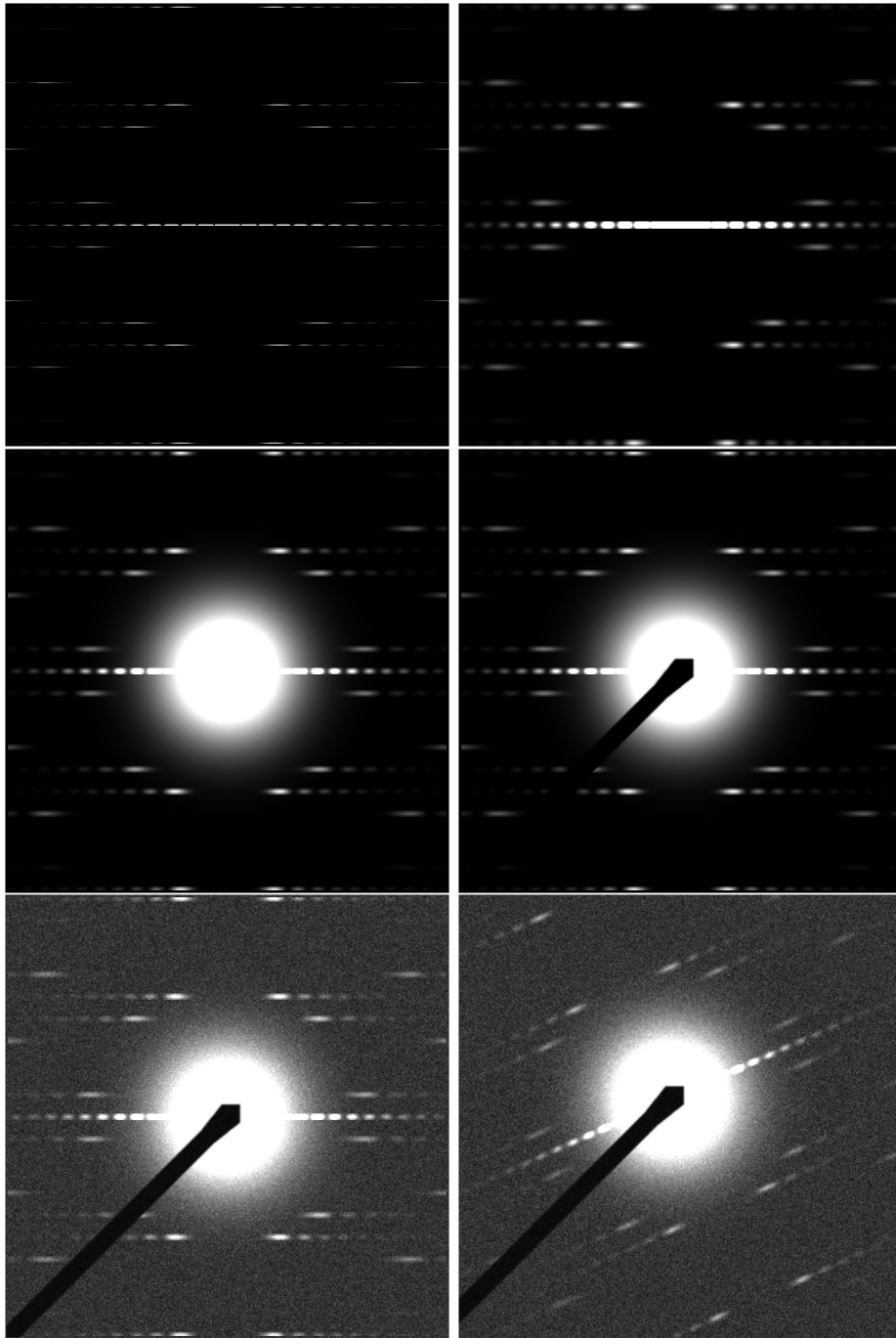


Figure 4.1: *Top left*: Simulated diffraction pattern of a (15, 8) carbon nanotube under incidence angle  $\gamma = 85^\circ$ . *Top right*: The simulation with broadened layer lines (FWHM 10 pixels). *Middle left*: Undiffracted electron beam added. *Middle right*: The simulation with a beamstopper. *Bottom left*: Noise with  $\sigma = 20\%$  of maximum intensity and ground 10% added. *Bottom right*: The image after shifting and rotating. The maximum intensity on the layer lines is reduced to 50% of the maximum image intensity.

### **Beamstopper**

The intensity in the center of the diffraction plane is very high, thus a TEM usually possesses a beamstopper, which blocks the central beam to beware the camera of damage.

To enhance the realism of the simulated image, a beamstopper is added. The shape varies in different TEMs. In the simulation a shape is used which is similar to the shape in some of the available experimental diffraction patterns.

The angle of the beamstopper can be adjusted, so different cases can be studied, where the beamstopper covers various parts of the layer lines.

In order to obtain a more realistic image, the boundaries of the beamstopper are blurred slightly.

### **Center of diffraction pattern**

The center of the diffraction pattern and the center of the image generally do not match in experimental data. In the simulation the diffraction center can also be shifted.

Also the tube axis is not parallel to the  $y$ -axis of the image in general. In the simulation the tube axis (and therefore the equatorial line and the layer lines) can be rotated.

### **Noise**

In all experimental data, and thus also in diffraction patterns, noise occurs. The noise added to the simulation is Gaussian distributed. The peak position (which can be interpreted as background intensity of the image) and the standard deviation  $\sigma$  of the noise can be adjusted.

For pixels which are covered by the beamstopper, the noise level is reduced which affects the peak as well as the standard deviation.

Since the level of the noise is not independent of that of the neighboring pixels, the noise is smoothed with a  $3 \times 3$  rectangular filter.

## **4.2 Approximate determination of the diffraction pattern center**

To analyze a diffraction image, the center of the diffraction pattern, which in general does not match the center of the image, has to be estimated. This is done by an

algorithm which works as follows.

First the row and the column with the highest average intensity are located. Since some images have increased brightness near the borders, the index  $i$  of the brightest row respectively column additionally has to fulfill the following condition:

$$\kappa w \leq i \leq (1 - \kappa)w \quad (4.1)$$

Here  $w$  denotes the image size in  $x$ - respectively  $y$ -direction. The factor  $\kappa \in [0, 0.5]$  determines, which fractional part of the image at the borders is ignored. If  $\kappa$  is chosen too large, it is possible that the center cannot be found, because it lies in the border area. A too small chosen  $\kappa$  may lead to evaluation of incorrect boundary values. For  $\kappa = 0.25$  good results were found. Since the beamstopper reduces the intensity, a row respectively column is found, which includes the central undiffracted electron beam but not the beamstopper.

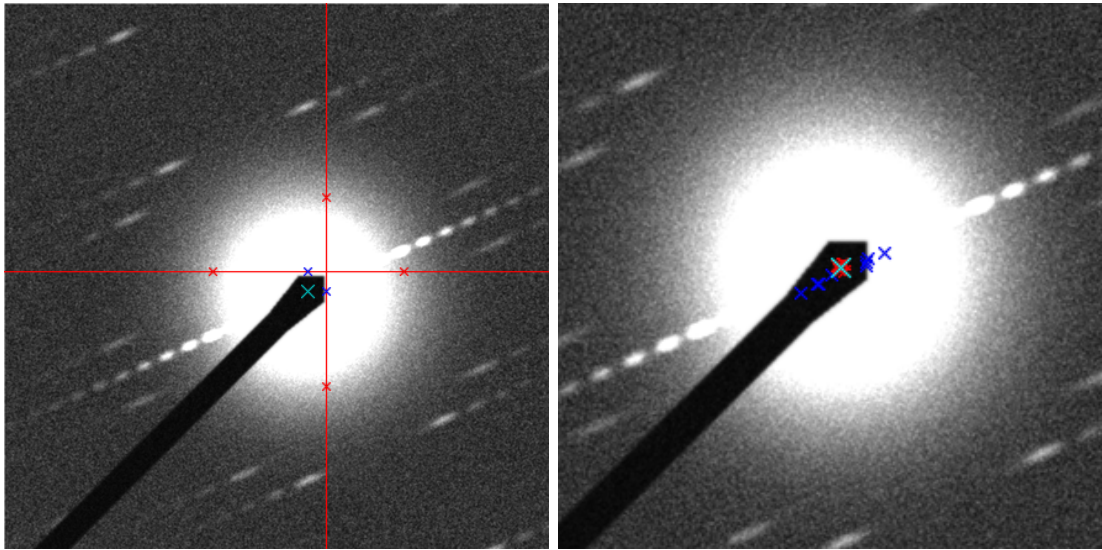


Figure 4.2: *Left:* The red lines (row respectively column) denote the highest average intensity in  $x$ - respectively  $y$ -direction. The crosses on these lines mark the points, where 80 % of the maximum intensity is exceeded for the first time. The blue crosses label the middle between these points. The cyan cross marks the estimated center for  $\beta = 0^\circ$ . *Right:* Centers estimated for various angles are shown in red and blue. Outliers are blue, used points are red. The cyan cross marks the average of the used centers.

The intensity distribution on this line is processed with a Gaussian filter ( $\sigma = 2$ ) to reduce the influence of noise. In this distribution the points with the lowest and highest index are searched for, whose intensity value exceed 80 % of the maximum intensity on this line. The center of the interval between these two points is defined

as the center of the diffraction pattern in  $x$ -direction. The center in the  $y$ -direction is estimated analogously (cf. figure 4.2 on the left).

This estimation is not only done for lines which are parallel to the  $x$ -axis but also for lines tilted by an angle  $\beta$  relatively to the  $x$ -axis. The column is always perpendicular to this line. The estimate for 20 different angles are shown in figure 4.2 in the right image.

Taking the mean of all calculated centers would be a problematic approach, as the estimation might be falsified for example when a line crosses the equatorial line or a reflection of high intensity. The mean is sensitive to such outliers. In this work, the median is used to detect, which centers may be outliers. Just estimations which have a maximum distance of 5 pixels in  $x$ - as well as in  $y$ -direction to the median are used to calculate the mean (cf. figure 4.2 on the right).

This method yields results of sufficient quality for the simulations and most of the available real patterns. If this step fails, the user has the opportunity to easily set the estimation of the center by hand.

In the following sections, “center” always means the center of the diffraction pattern not the center of the image.

## 4.3 Delineation of the beamstopper

In the available experimental diffraction images the central electron beam is partly covered by a beamstopper. Since that changes the image significantly (for example reflections may be covered) the modified pixels have to be known. Simply marking the darkest part of the image is not sufficient, because near the image borders the intensity of the rest of the image may also be low and even on the beamstopper may be bright artifacts.

So in this work the delineation of the beamstopper is realized by the use of the snake algorithm, which was described in section 3.2.

### 4.3.1 Initialization of the snake algorithm

Before the active contour can start to learn the shape of an object it has to be initialized. This could be done by a rough delineation of the user. Since the program should work as autonomously as possible the initialization is done automatically.

The starting point for the initialization is the center determined in the previous section, because the center of the diffraction pattern is always supposed to be covered by the beamstopper. Also the direction of the beamstopper should be known. This

can be estimated by calculating the average intensity on lines of various angles relative to the  $x$ -axis starting at the center. The angle with the lowest average intensity should be the angle of the beamstopper.

A rectangle is a good approach for the shape of the initialization. The length of the rectangle in the direction of the beamstopper is limited by the image borders. In the opposite direction the intensity distribution is measured depending on the distance to the center. The lowest value of this distribution is subtracted from all values to remove the baseline and a Gaussian filter with  $\sigma = 3$  is applied for smoothing (cf. figure 4.3). The point where the intensity exceeds 50 % of the maximum intensity of this distribution for the first time determines the length of the rectangle in the opposite direction of the beamstopper. The width of the rectangle is set to 40 pixels.

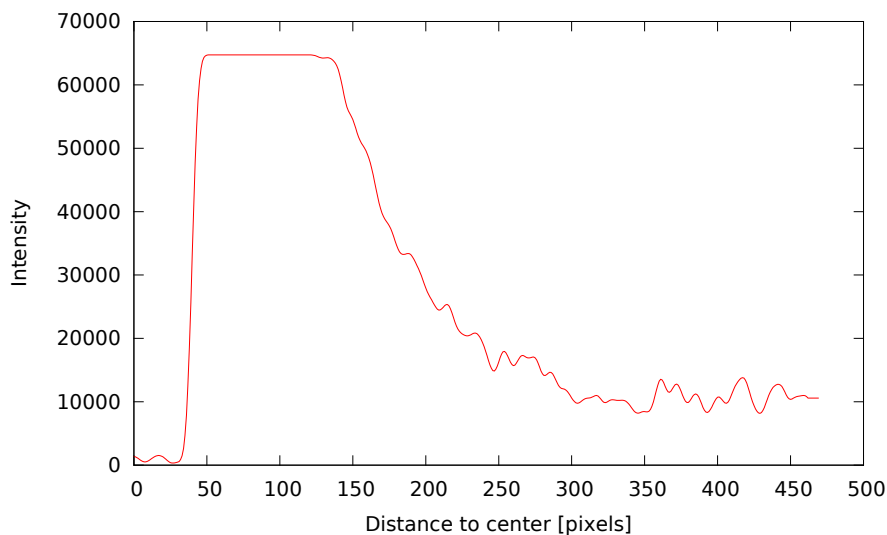


Figure 4.3: Intensity distribution versus distance to the center measured in the opposite direction of the beamstopper: The point where the intensity exceeds 50 % of the maximum intensity of this distribution for the first time determines the length of the rectangle in the opposite direction of the beamstopper.

Another parameter which has to be chosen is the distance between the nodes of the snake. This parameter is set to 6 pixels. The initialization for the simulated image is shown in figure 4.4.

### 4.3.2 Application of the snake algorithm

To apply the snake algorithm the intensity gradient in the image has to be known. The horizontal gradient at the point  $\vec{p} = (x, y)$  is calculated by the following formula:

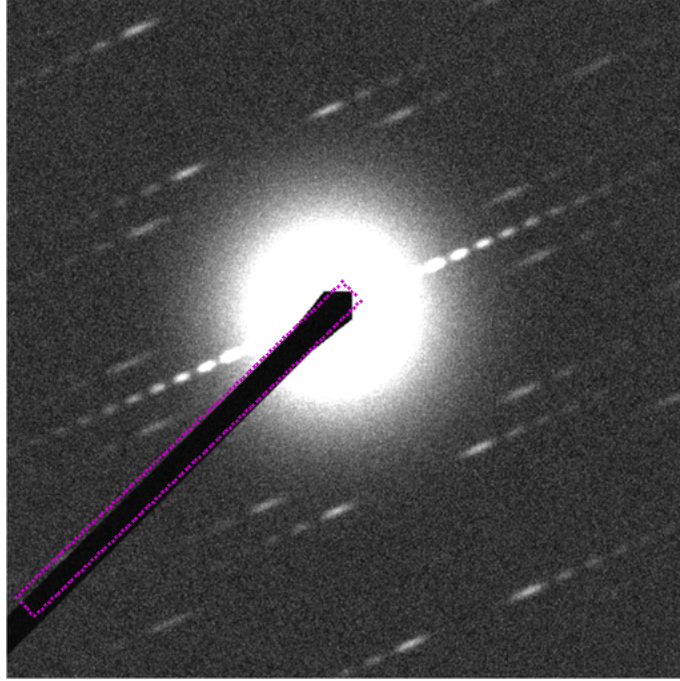


Figure 4.4: The initialization of the snake-algorithm for the beamstopper detection is realized by a rectangle. The red points show the nodes of the active contour.

$$\nabla p_{hor} = \sum_{n=1}^N \sum_{m=1}^M F_{n,m}^{hor} I \left( \begin{array}{c} x + m - (M + 1)/2 \\ y + n - (N + 1)/2 \end{array} \right) \quad (4.2)$$

The function  $I(x, y)$  denotes the intensity at the point  $\vec{p} = (x, y)$ . The  $N \times M$  matrix  $F^{hor}$  is called filter. The number of rows and columns in this filter is always odd. Because the diffraction image contains no information at the borders and the filter cannot be applied there, the gradient in this area is set to zero. The vertical component of the gradient is calculated analogously.

Using the simple form of the filter in the horizontal direction

$$F^{hor} = (-1, 0, 1) \quad (4.3)$$

may yield reasonable results for some images. But in many cases the gradient is dominated by noise and not by the edge of the beamstopper. To reduce the noise influence for the calculation of the horizontal component of the gradient a filter of the following form is used [10]:

$$F^{hor} = \begin{pmatrix} 0 & 0 & -1 & 0 & 1 & 0 & 0 \\ 0 & -1 & -2 & 0 & 2 & 1 & 0 \\ -1 & -2 & -4 & 0 & 4 & 2 & 1 \\ -2 & -4 & -8 & 0 & 8 & 4 & 2 \\ -1 & -2 & -4 & 0 & 4 & 2 & 1 \\ 0 & -1 & -2 & 0 & 2 & 1 & 0 \\ 0 & 0 & -1 & 0 & 1 & 0 & 0 \end{pmatrix} \quad (4.4)$$

The filter for the vertical component is given by:

$$F^{vert} = \begin{pmatrix} 0 & 0 & -1 & -2 & -1 & 0 & 0 \\ 0 & -1 & -2 & -4 & -2 & -1 & 0 \\ -1 & -2 & -4 & -8 & -4 & -2 & -1 \\ 0 & 0 & 0 & 0 & 0 & 0 & 0 \\ 1 & 2 & 4 & 8 & 4 & 2 & 1 \\ 0 & 1 & 2 & 4 & 2 & 1 & 0 \\ 0 & 0 & 1 & 0 & 1 & 0 & 0 \end{pmatrix} \quad (4.5)$$

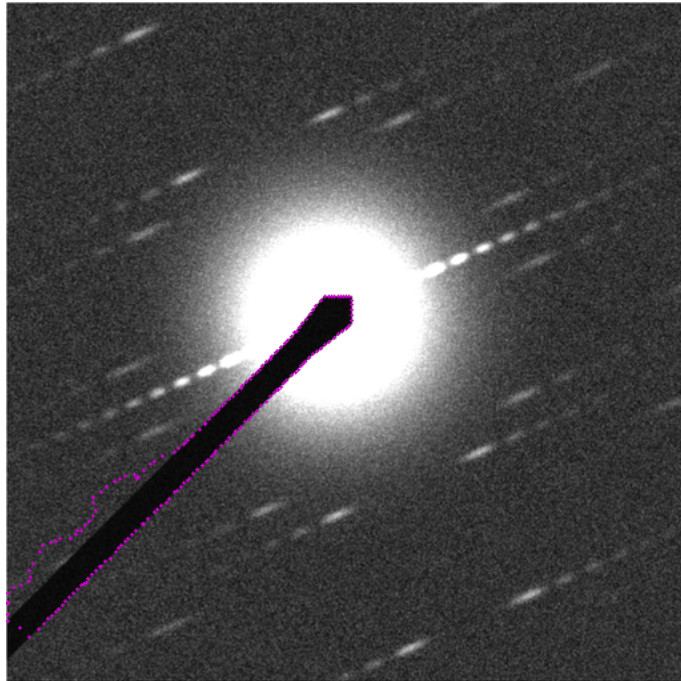


Figure 4.5: The red points show the active contour after learning. The used parameters are given in table 4.1.

Using these filters and the values in table 4.1 for the parameters defined in section

3.2 leads to the shape of the snake shown in figure 4.5.

$\omega_m$	$\omega_{\delta I}$	$\omega_g$	$\omega_{\delta G}$	$\omega_c$	$\omega_b$	<i>size</i>
1.85	0.001	7.0	0.0	10.0	6.5	10

Table 4.1: Parameters of the snake algorithm for the beamstopper detection. The parameter *size* denotes the size of the neighborhood.

In the next step the nodes of the snake are connected and the enclosed pixels are marked as corrupted, which means that they will be disregarded in the following analysis steps. Also points which are closer than 3 pixels to the active contour are marked as invalid. This is necessary because due to the blurring of the beamstopper the active contour might not move exactly to the outer object boundaries.

The beamstopper is in general not circular in the center. In the subsequent analysis steps average intensities dependent on the distance to the center are calculated. Hence in some directions the beamstopper makes the pixels invalid and in other directions not. This leads to a very small number of valid values for some distances. A small number of valid pixels also means, that the average in this interval is very sensitive to noise.

Here the used solution to this problem is to add a circle around the center to the beamstopper. The radius of the circle is calculated by measuring the largest distance from the center to the pixels, which are identified to belong to the beamstopper in the directions which differ at least  $75^\circ$  from the beamstopper direction.

The layer lines are not affected by this circle since the radius of the circle is smaller than the distances of the center to the reflections.

## 4.4 Normalization of the intensity

The determination of the diffraction spots positions is complicated by the undiffracted electron beam which has a by far higher intensity than the features in the image and therefore prohibits the identification on the basis of the intensity.

In a first step the average intensity of the image dependent on the distance to the center is calculated. Pixels, which are identified to be covered by the beamstopper, do not contribute to this calculation.

There are two possibilities for the normalization of the brightness: On the one hand the intensity of each pixel is divided by the corresponding value in the radial intensity distribution. On the other hand the new brightness can be obtained by subtraction of the corresponding intensity. The subtraction yields slightly better results, so it is

used here.

An unwanted feature of this method is, that a group of bright points, which are located on a circle around the center, cause a maximum in the radial intensity distribution and therefore are unduly strongly diminished. The brightest maxima on the layer lines form such a group of points and are consequently darkened. This effect is small for a diffraction pattern with few reflections, which are sharp and of low intensity. But it becomes significant when there are many layer lines or the reflections are broad. Then this causes a dark circle through the reflection maxima (cf. figure 4.6).

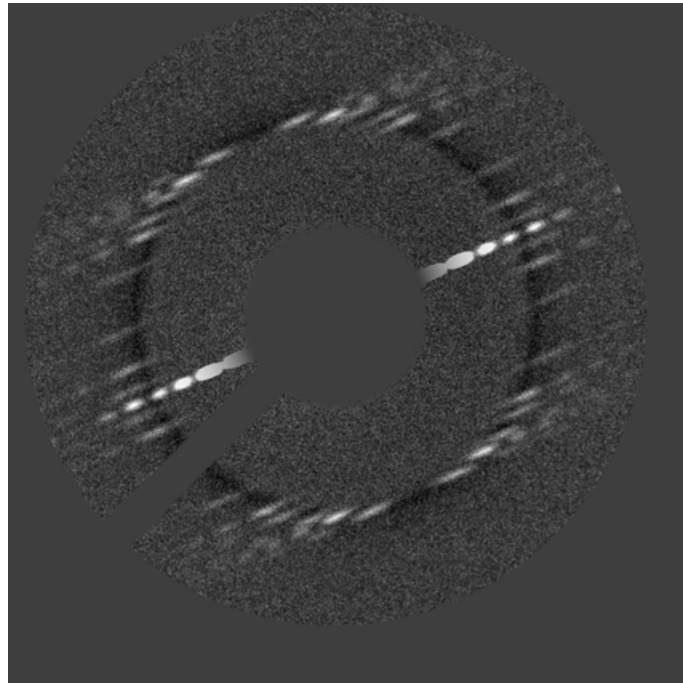


Figure 4.6: A simulated diffraction pattern of a bundle of a (15, 8), a (10, 2) and a (9, 7) nanotube: Since the highest intensities on the layer lines are located nearly on a circle, a black circle through these reflections appears after the normalization.

To get rid of the maximum in the intensity distribution, the curve is approximated with an exponential function of the form:

$$y = a \exp(bx) + c \quad (4.6)$$

Keeping  $c$  constant and using  $y' = y - c$  we obtain the equation

$$y' = a + \exp(bx) \quad (4.7)$$

The parameters  $a$  and  $b$  can be determined as described in section 3.1.

The quadratic error between the fit and the measured curve is also used to optimize the parameter  $c$  numerically.

To reduce the effect of the maxima on the fitted curve, only points  $i$  are used, whose intensity  $I(i)$  is lower than the intensity of all points with smaller distance to the center:

$$I(i) < I(j) \quad \forall j < i \quad (4.8)$$

If this condition is not fulfilled, the point  $i$  is not used for the approximation. Points with intensity zero are ignored. Figure 4.7 shows the measured curve, the used points and the fitted curve.

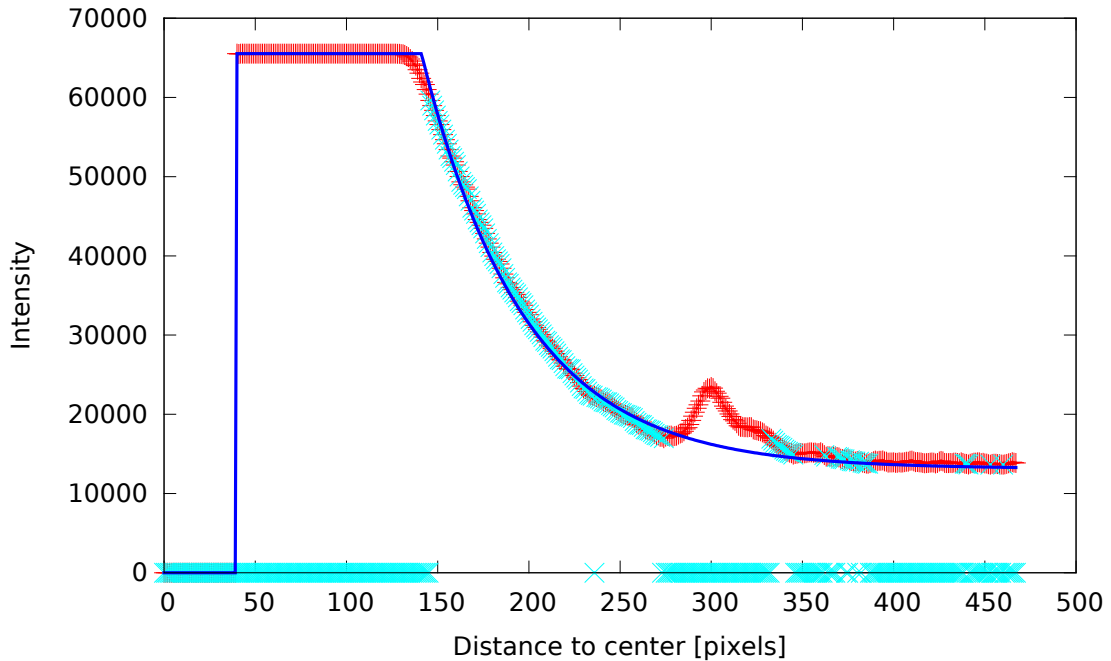


Figure 4.7: The red points show the measured intensity distribution, cyan are the points used for the fit. The blue curve marks the fitted curve. The analyzed pattern is the same as in figure 4.6.

If the fitted curve is used for the subtraction of the radial intensity, no dark circle is noticeable as can be seen in figure 4.8. This means, that the intensities of the interesting diffraction maxima are not diminished above average.

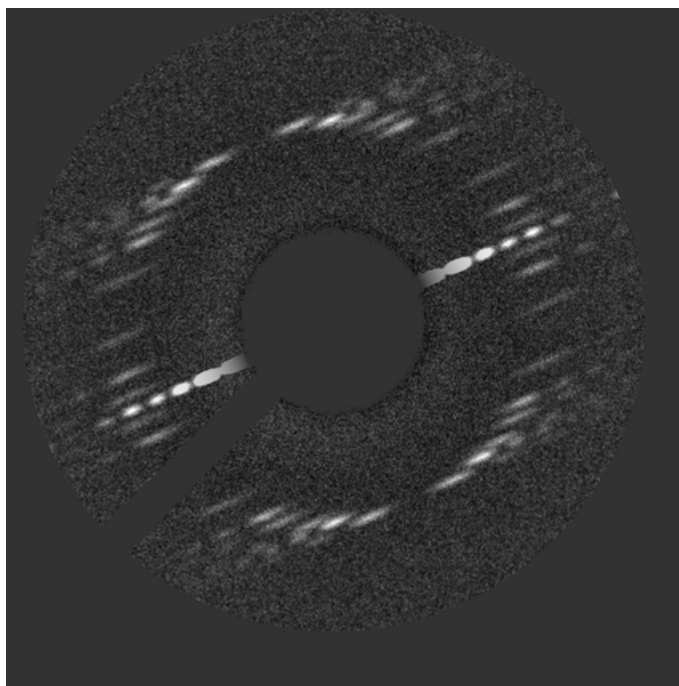


Figure 4.8: Image after subtracting the fitted radial intensity distribution: The black circle of figure 4.6 vanishes. The analyzed pattern is the same as in figure 4.6.

## 4.5 Determination of the layer line distances to the equatorial line

To determine the ratio of the chiral indices  $n$  and  $m$  (and therefore the helical angle  $\alpha$ ) it is sufficient (cf. section 2.3.3) to know the distances of the layer lines to the equatorial line. These distances can be measured relatively exact even in images of low quality.

Additionally, to use this method for the determination of the helical angle, the angle  $\gamma$  between the nanotube axis and the incoming electron beam is not needed.

### 4.5.1 Determination of the equatorial line

To determine the distances of the layer lines to the equatorial line, the course of the equatorial line has to be located first. Since it always crosses the center of the diffraction pattern, which was already identified in section 4.2, only its direction has to be detected.

For that purpose the average intensity on a straight line through the center is calculated for various angles. Pixels, which are corrupted by the beamstopper, are ignored. Since the equatorial line possesses a high intensity, the angle with the

highest average intensity is considered the angle of the equatorial line.

### 4.5.2 Radius of the first reflection spots

The distance of the layer lines to the equatorial line is obtained by the distribution, which measures the average intensity with respect to the distance to the equatorial line. If all pixels of the image are taken into account, a disadvantage is, that the ratio between the number of pixels which actually contain information and the number of pixels evaluated is small.

Since the wanted reflections are located near a circle around the center, it is more convenient to take only the intensities of pixels near this circle into account.

For this purpose the radius of this circle has to be detected first. The reflections are supposed to cause a maximum in the radial intensity distribution of the image obtained in section 4.4. But due to the fact that the equatorial line and also artifacts might produce maxima, it would be hard to identify the maximum corresponding to the diffraction reflections. So further preprocessing is needed.

First, the intensity  $I_{10\%}$  is estimated, which only 10% of all pixels exceed. Analogously the intensity  $I_{20\%}$  is obtained. All pixels in the image are set to zero, whose intensity is lower than  $I_{10\%}$ . All eight neighbors of those points, whose intensity is still not zero, are checked, if their original intensity exceeds  $I_{20\%}$ . If this is the case for a neighbor, its intensity is set back to its original intensity and the eight neighbors of this point are checked as well.

This method, which is also known as region growing [10], leads to connected areas of high intensity. This favors diffraction spots over noise, since the diffraction spots form connected areas.

In the next step, the  $2mm$  symmetry of the pattern is used (cf. section 2.4). For pixels, which possess non-vanishing intensity values, the intensity at the three corresponding symmetry positions is checked. If at one of the corresponding positions the intensity value is zero everywhere in a small neighborhood, the initial pixel is also set to zero. Pixels which are identified as being corrupted by the beamstopper are not evaluated (cf. figure 4.9).

The radial intensity distribution of this image is calculated (cf. figure 4.10), whereby pixels are omitted which have a distance of less than 10 pixels to the equatorial line. Otherwise the equatorial line would cause disturbing maxima in the intensity distribution. The curve is smoothed with a Gaussian filter with  $\sigma = 10$ .

In this simulated image it would be sufficient to determine the position of the highest maximum, which roughly represents the distance of the primary diffraction spots to

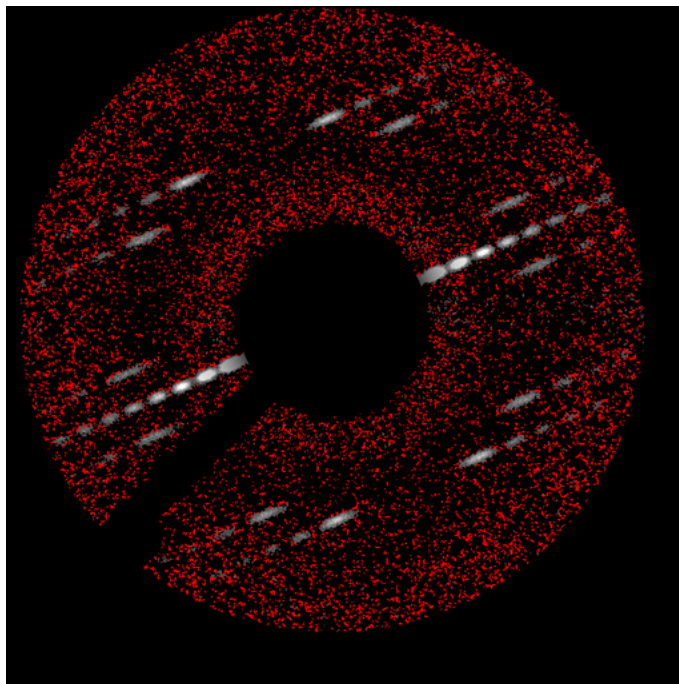


Figure 4.9: Image after the region growing: Pixels, which have non-zero intensity after the region growing but do not pass the symmetry check, are red. The symmetry check reduces the noise significantly.

the center and therefore the radius of the circle, in this plot.

In real patterns that often is not sufficient (for example for the image in section 6.1), since the removal of the undiffracted electron beam works not perfect. So the algorithm uses a different measure to determine the height of a maximum. The latter is calculated with respect to the lowest intensity that occurs in the distribution for smaller distances to the center. Distances which are dominated by pixels corrupted by the beamstopper are not evaluated. The position of the maximum which has the highest amplitude in this sense is taken as the radius of the circle.

Now the average intensity is calculated only with the use of pixels, which have a distance of at most 10 pixels to this circle in the direction parallel to the equatorial line. The amplitude of the maxima, which corresponds to the distances of the layer lines to the equatorial line, is much higher than in the curve calculated for the whole image (cf. figure 4.11).

### 4.5.3 Correction of center and angle

If the center of the diffraction pattern or the angle of the equatorial line is not located exactly, this has severe consequences for the determination of the layer line

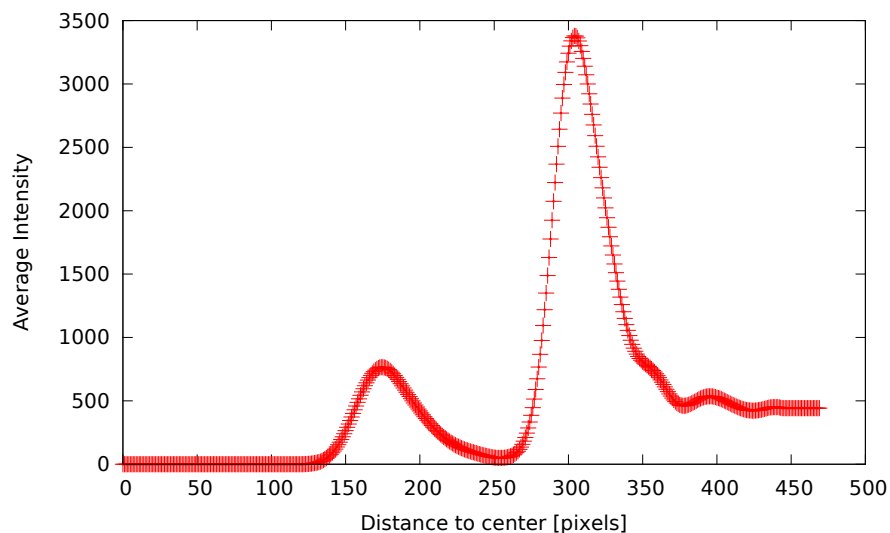


Figure 4.10: The radial intensity distribution of the image in figure 4.9: The position of the maximum indicates the radius of the circle through the primary diffraction spots. The curve is smoothed with a Gaussian filter with  $\sigma = 10$ .

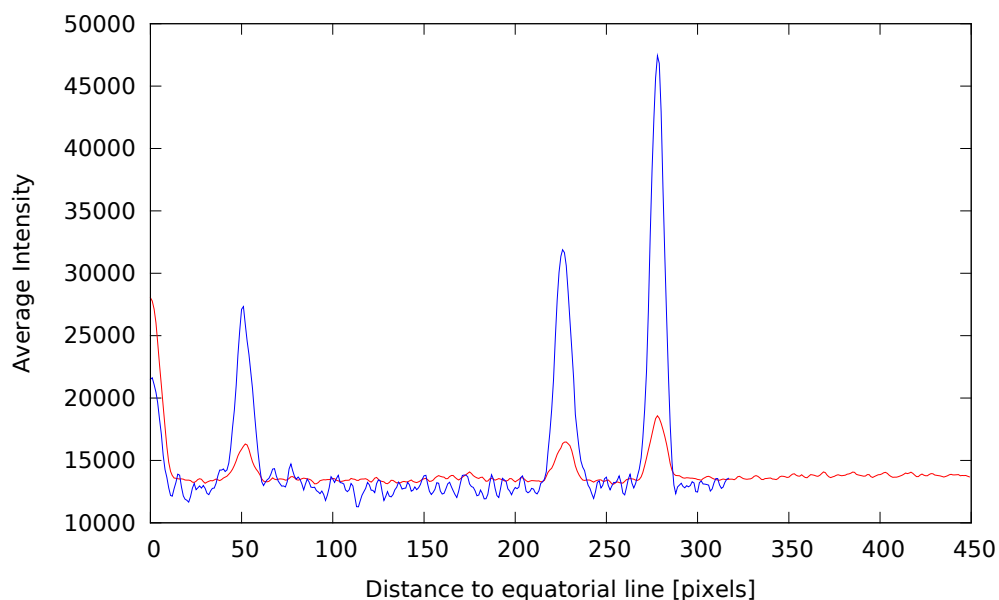


Figure 4.11: Average intensity with respect to the distance to the equatorial line: The red curve is measured with the use of the whole image. For the blue curve just pixels near a circle through the reflections are used. The advantage gets clearer for images of low quality.

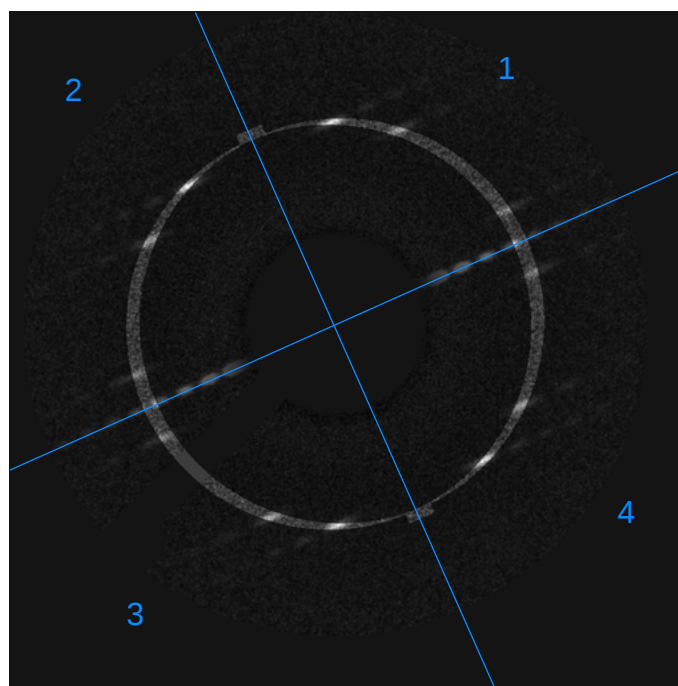


Figure 4.12: Pixels which are used for the calculation of figure 4.11 are highlighted. The blue lines and numbers denote the numbering of the quadrants.

distances to the equatorial line. Even if the center of the undiffracted electron beam is identified correctly by the algorithm described in section 4.2, that is not necessarily the center of the diffraction pattern (cf. section 6.2).

In the following the “quadrants” of the diffraction pattern are used. These are defined analogously as in a coordinate system, where the equatorial line represents the  $x$ -axis. The first quadrant is above the equatorial line and on the right side of the tube axis. The others are numerated counter clockwise (cf. figure 4.12).

For an estimated angle, which is smaller than the real angle of the equatorial line, the layer line distances in the individual quadrants do not match. The distances in quadrants one and three are too large and in quadrants two and four too small. If the center is above the real equatorial line, the distances in quadrants one and two are too small, in quadrants three and four too large.

The differences might be compensated by averaging over the quadrants, but still the maxima would be broadened. This could also cause that layer lines with similar distances to the equatorial line cannot be distinguished in the averaged intensity distribution.

Therefore a correction of the center and the angle of the equatorial line is necessary. Figure 4.13 shows the intensity distribution with respect to the distance to the

equatorial line measured in the four quadrants for an image, where the estimation of the center was set 5 pixels away from the real center to demonstrate the effect.

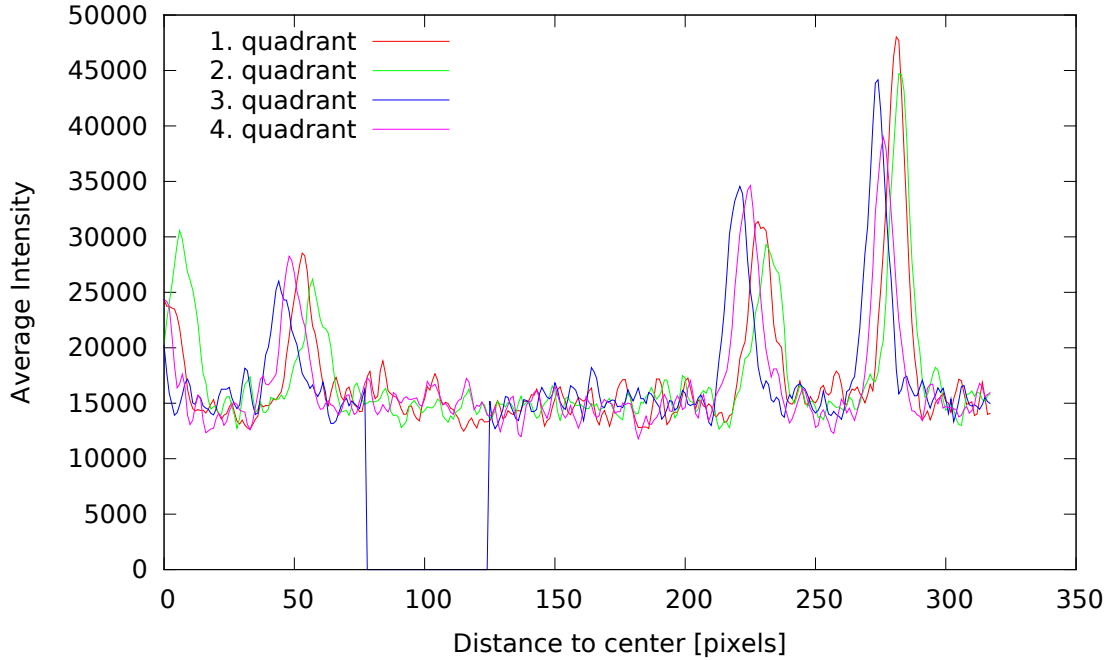


Figure 4.13: Intensity distribution measured separately in the four quadrants: The center was manually moved 5 pixels away from the real center for demonstration purposes. The undefined values in the third quadrant are caused by the beamstopper.

Due to the symmetry of the diffraction pattern, the intensity distribution in all quadrants is supposed to be the same. This can be used to correct the position of the center and the angle of the equatorial line.

To detect a more suitable center respectively angle, the position of the center respectively the angle is changed in small steps with the goal to maximize the congruence of the intensity distributions in the quadrants.

The measure of congruency is defined in the following:

For all pairs of quadrants the correlation  $C_{ij}$  for various offsets  $o$  of the  $x$ -axis relative to each other is calculated (cf. figure 4.14):

$$C_{ij}(o) = \sum_n^N I_i(n) \cdot I_j(n + o) \quad (4.9)$$

where  $N$  denotes the number of values of the intensity distributions and  $I_i(n)$  is the value in the intensity distribution of the  $i$ th quadrant at point  $n$ .

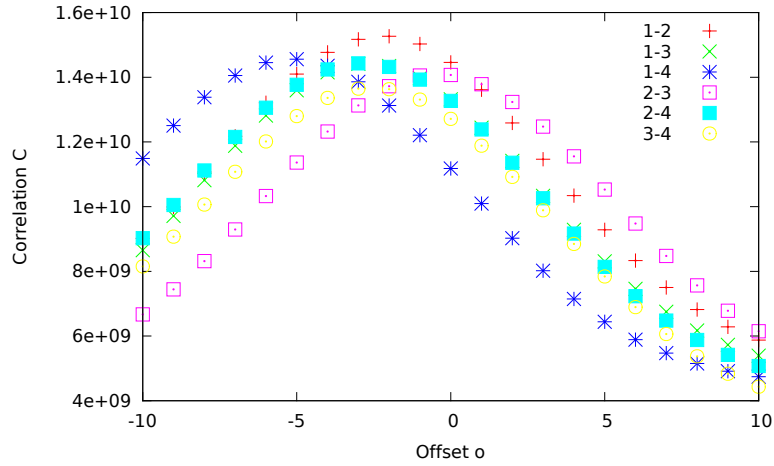


Figure 4.14: The correlation between the intensity distributions of pairs of quadrants related to the offset  $o$  by which the curve was shifted: For the calculation the baseline of the distributions was removed. The center and angle would be found well, if the maximum of each curve was located near zero.

For the calculation of the correlations the baseline is removed from the intensity distributions in each quadrant. The intensity of the baseline is given by the lowest intensity value, which was not labeled to belong to the beamstopper. By the removal of the baseline the influence of the higher intensities, which represent the layer lines, is increased relatively to the noise.

The exact maximum of the curves is interpolated by fitting a parabola to the curves in figure 4.14. This maximum corresponds to an optimal offset  $p_{ij}$  for each combination of the quadrants.

The measure of congruency  $M_{cor}$  is the square of the optimal offsets of all combinations of the quadrants:

$$M_{cor} = \sum_{i=1}^3 \sum_{j=i+1}^4 p_{ij}^2 \quad (4.10)$$

The correction of the center position and the angle of the equatorial line is done by the following algorithm:

1. Calculate  $M_{cor}$  for the current center and for a center moved by  $dx$  respectively  $-dx$  along the tube axis. Take the point with minimum  $M_{cor}$  as the new center.
2. Calculate  $M_{cor}$  for the current center and for a center moved by  $dy$  respectively  $-dy$  along the equatorial line. Take the point with minimum  $M_{cor}$  as the new center.

3. Calculate  $M_{cor}$  for the current angle of the equatorial line and for an angle tilted by  $d\alpha$  respectively  $-d\alpha$ . Take the angle with minimum  $M_{cor}$  as the new angle.
4. If in any of the steps 1-3 the new value was not equal to the old value, go back to step 1.
5. Decrease  $dx$ ,  $dy$  and  $d\alpha$  by multiplying with a predefined factor  $\beta \in [0, 1]$ .
6. If  $dx > dx_{min}$  respectively  $dy > dy_{min}$ , whereas  $dx_{min}$  and  $dy_{min}$  are predefined, go back to step 1, else stop.

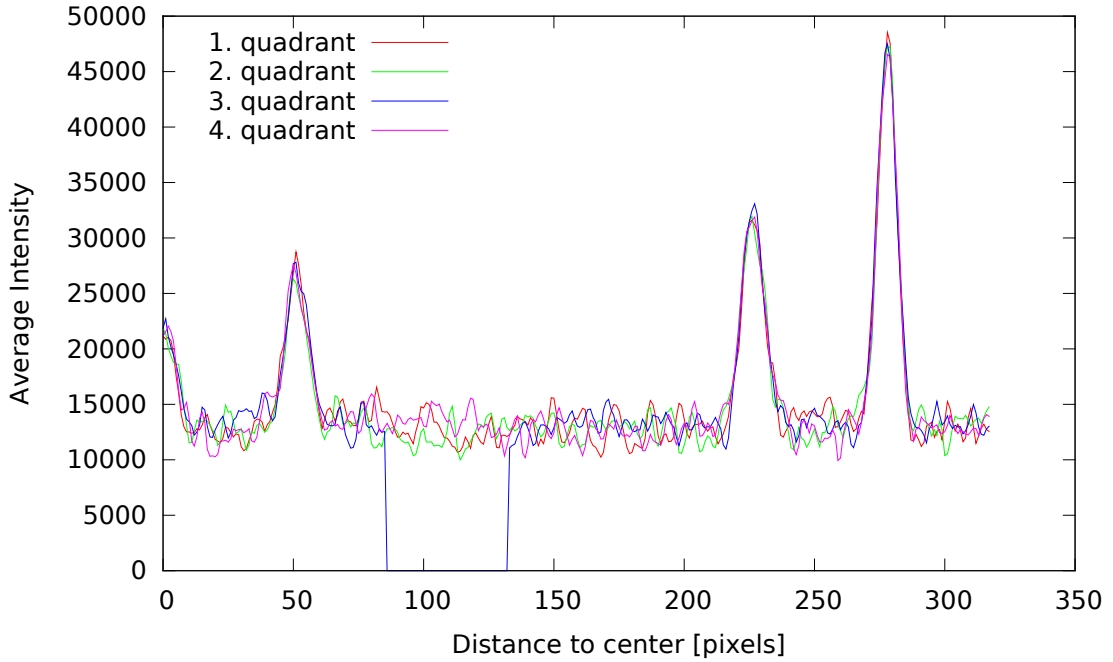


Figure 4.15: Intensity distribution measured separately in the four quadrants after the correction of the center and the angle of the equatorial line: The positions of the maxima in the four quadrants are very similar. The undefined values in the third quadrant are caused by the beamstopper.

Figure 4.15 shows the intensity distributions related to the distance to the center in each quadrant after the correction of the center position and the angle of the equatorial line. The positions of the maxima in the four quadrants are very similar. The parameters were set to:  $dx = dy = 1$  pixel,  $d\alpha = 0.1^\circ$ ,  $\beta = 0.1$  and  $dx_{min} = dy_{min} = 0.09$ .

The simple approach to move the center along the tube axis corresponding to the offset in the correlation would be insufficient, because the intensity is measured on

a circle. This leads to a nonlinear dependency of the offset on the center position. The same holds for the angle.

#### 4.5.4 Determination of the ellipse parameters

However the diffraction spots are not located on an exact circle, particularly when the incidence of the electron beam is not  $90^\circ$ . Especially in that part of the circle, which is far from the equatorial line, it is possible, that the diffraction spots are not crossed perfectly. This leads to a deviation in the measurement of the layer line distances.

A more proper approximation of the positions of the diffraction spots is given by an ellipse. The parameters  $e_a$  respectively  $e_e$  here denote the major axis respectively the eccentricity of the ellipse. These parameters are optimized such, that the wanted diffraction spots are matched as well as possible. The measure of the quality of the match is the average intensity of the curve measured near the ellipse, as described in the last section. This means all pixels are used, whose distance to the ellipse is less or equal than 10 pixels in the direction parallel to the equatorial line.

In this example the values  $e_a = 308$  and  $e_e = 0.22$  were estimated, which leads to a minor axis of size 300.5 pixels. By the usage of the ellipse especially in case of the real image in section 6.2 the diffraction spots are matched better.

Afterwards again a correction of the center and the angle is performed as described in the previous section, but now with the usage of the curves measured near the ellipse.

#### 4.5.5 Determination of the layer line distances

To get the distances of the layer lines to the equatorial line from the obtained curve, the maxima have to be determined as exactly as possible. This is done by a method described by Harald Broll [11]. According to this technique, a point  $i$  is a maximum if it fulfills three criteria:

- Change of the sign of the local slope:

$$y(i) - y(i + 1) > 0 \quad \wedge \quad y(i) - y(i - 1) > 0 \quad (4.11)$$

- Maximum value in an environment  $d$ :

$$y(i) - y(i + j) > 0 \quad \wedge \quad y(i) - y(i - j) > 0 \quad \forall j = 1, \dots, d \quad (4.12)$$

- Average slope  $\bar{s}$  fulfills  $\bar{s} > s_{min}$  with

$$\bar{s} = \frac{1}{2d} \left( |y(i) - y(i+d)| + |y(i) - y(i-d)| \right) \quad (4.13)$$

- Additionally the value has to be larger than the mean:

$$y(i) > \bar{y} \quad (4.14)$$

Equation (4.11) describes a change in the sign of the first derivative, at which the first positive and then negative slope defines a local maximum. This condition alone is not sufficient, since due to local fluctuations many points fulfill it.

The second criterion excludes the points, which are not extremal in a neighborhood  $d$ . Here  $d$  is set to 4 pixels which also means, that the distance between layer lines has to be at least 4 pixels.

For the third criterion the average slope in the neighborhood  $d$  of a potential maximum is calculated. With the parameter  $s_{min}$  the number of maxima found can be regulated.

The fourth criterion avoids that points with low intensities are identified as maxima. The shape of the maxima may be deformed, so that the point with the highest intensity does not represent the real maximum. Furthermore a higher accuracy than 1 pixel is desirable for the determination of the distances. Therefore the environment of a maximum is approximated by a GLLS-method of second order (cf. section 3.1). It is problematic, that approximating functions, which are calculated with constant standard deviations, average the error uniformly over the environment. Therefore the approximating function is influenced by the standard deviation  $\sigma_j$  which is calculated as follows:

$$\sigma_j = b + a(j - i)^2 \quad (4.15)$$

Here  $i$  denotes the coordinate of the found maximum,  $j$  the position of the points in the neighborhood and  $a$  is an appropriate slope parameter. The minimum standard deviation in the center  $i$  is denoted by  $b$ .

In this thesis  $b = 1$  and  $a = 0.1$  is used. With this method the maxima can be estimated fast and accurately. It is used in the following, wherever a maximum has to be determined.

Initially it is not known, how many tubes and therefore layer lines, which again correspond to the number of maxima in the intensity distribution, have to be found.

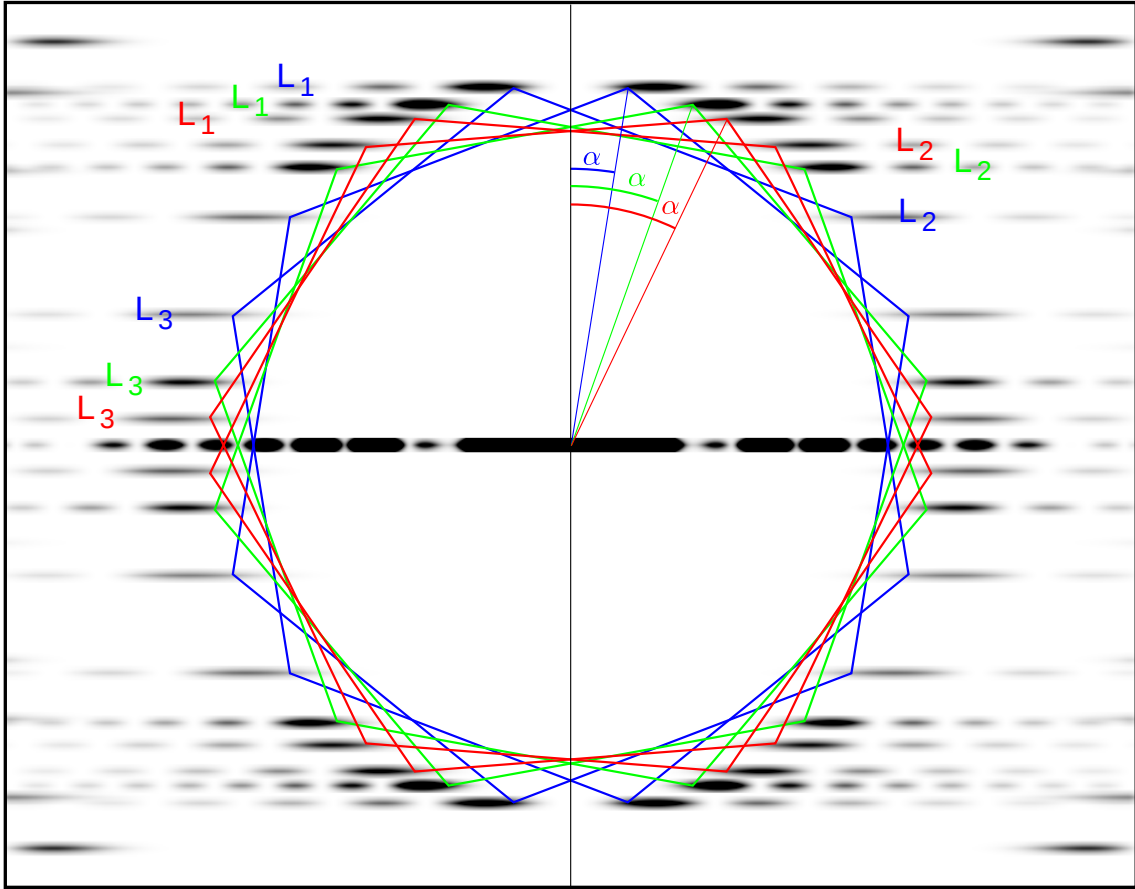


Figure 4.16: Schematic diffraction pattern of a bundle of three nanotubes: The principal diffraction spots lie near the edges of hexagons. With increasing helical angle  $\alpha$ , the distances of layer line 1 and 3 to the equatorial line decrease, for layer line 2 the distance grows.

The program now tries to find maxima for all possible numbers  $N$  of tubes with  $1 \leq N \leq N_{max}$ , which can be combined to layer lines of  $N$  tubes.

The algorithm to detect the layer lines for a given number of tubes  $N$  works as follows:

0. Initialize  $s_{min}$  with a high value (here  $s_{min} = 1000$ ).
1. If  $s_{min} < \epsilon$  stop.
2. Search for maxima which fulfill equations 4.11 - 4.14. The set  $M$  of the positions of the maxima is sorted in descendant order.

$$M_i > M_{i+1} \quad \forall i < K \quad (4.16)$$

where  $K$  is the number of located maxima.

3. If  $K < 2N$  decrease  $s_{min}$  and go back to 1.
4. If  $K > 3N$  stop.
5. Assume that the positions of the  $N$  maxima with the largest distance to the equatorial line represent the distances of the first layer lines of the tubes.

$$d_1^i = M_i \quad (4.17)$$

where  $d_1^i$  denotes the distance of the first layer line of the  $i$ th tube to the equatorial line.

6. The distances of the second layer lines are in reversed order in relation to the distances of the first layer lines (cf. figure 4.16). Therefore the following distances can be assigned:

$$d_2^i = M_{2N+1-i} \quad (4.18)$$

where  $d_2^i$  denotes the distance of the second layer line of the  $i$ th tube to the equatorial line.

7. Check if

$$\frac{2d_2^i - d_1^i}{2d_1^i - d_2^i} \geq 0 \quad \forall i \quad (4.19)$$

is valid. If not, decrease  $s_{min}$  and go back to step 1.

8. Calculate theoretical positions of third layer lines:

$$d_3^i = d_1^i - d_2^i \quad (4.20)$$

Try to assign the remaining maxima in  $M$  to the theoretical positions. The theoretical and measured positions may differ at most by 10 pixels. To each tube only one measured position may be assigned as third layer line. If any of the remaining maxima could not be assigned, decrease  $s_{min}$  and go back to step 1.

9. Set of layer lines for  $N$  tubes found.

Step 1 is necessary to avoid an infinite loop, because it is possible that a too small number of maxima is found even for very small  $s_{min}$ . Here  $\epsilon = 0.1$  is used.

Step 3 takes into account that for a given number  $N$  of tubes, at least  $2N$  maxima have to be found, since for the calculation of the ratio  $m/n$  of the chiral indices the distances of the first and second layer line of a tube have to be known. At most  $3N$  maxima may be found (cf. step 4), because the circle, on which the analysis takes place, only contains the first maxima of the three principal layer lines of each tube.

In step 5 the fact is used, that the distances of the first layer lines of all combinations of chiral indices are greater or equal than the distances of the second layer lines (cf. figure 4.16). The case, where the distance is the same for the layer lines, is the “armchair” tube. The distances of the first and second layer line of an armchair tube cannot be detected automatically by this algorithm (cf. section 5.3.2).

The distance of the first layer line decreases with a growing helical angle  $\alpha$ .

The second layer line adopts the opposite behavior. With a growing helical angle  $\alpha$  the distance to the equatorial line increases. Therefore the second layer lines have to be assigned to the tubes in reverse order relatively to the first layer lines (cf. figure 4.16). This is done in step 6.

Step 7 checks, if the found layer line positions yield chiral indices  $(n, m)$  which fulfill the conditions described in section 2.10. These conditions only allow  $m/n \in [0, 1]$ . Since values higher than 1 cannot appear, because  $D_1^i > D_2^i$  always holds, only the negative case has to be eliminated.

After the analysis that was described in this section the number of tubes is still not known. It is possible that appropriate combinations of layer lines are found for a smaller number of tubes and not all existent tubes are recognized. That happens for example when the layer lines of a certain tube are less distinct than those of the other tube(s). If noise is wrongly considered a maximum, a too high number of tubes would be indicated. To avoid that the steps 7 and 8 are applied, but this case cannot be completely obviated.

The correct number can therefore not be determined entirely automatically. Supposed layer lines that in fact consist of noise will perform badly in the following evaluation steps. Hence the true number is mostly the highest that still yields sensible results during the analysis. The ultimate decision however the user has to make.

For every possible quantity of tubes, the distances of the first two layer lines are known at any rate. The third layer line does not have to be detected, as it is not necessary to obtain the ratio of  $m/n$ . Since layer line three exhibits the smallest intensity, it is often not detected.

### 4.5.6 Improvement of the accuracy

To determine the measured ratio  $r_{meas} = m/n$  of the chiral indices, which already determines the helical angle  $\alpha$ , as accurately as possible, the distances of the layer lines to the equatorial line should be determined precisely.

The measurement of the intensity distribution relative to the equatorial line near an ellipse has advantages like reducing undesired effects of artifacts. Another positive effect is that the probability to distinguish maxima which overlap in their extent in the direction of the tube axis, is increased (cf. section 5.1 and section 6.2.7).

These advantages make the measurement near the ellipse a good choice for the estimation of the layer line distances and therefore the number of tubes.

The advantage that the intensity distribution is depending on the distance to the tube axis is also a disadvantage. The diffraction spots are not crossed perpendicularly by the ellipse and therefore the intensity distribution is not only dependent on the distance to the equatorial line but also on the distance to the tube axis.

To get rid of that dependency, for each layer line which was identified in the previous section an intensity distribution related to the distance to the equatorial line is calculated, which is independent of the distance to the tube axis. The measurement takes place in a small rectangle around the position of the spot, which is the point of intersection of the ellipse with a line parallel to the equatorial line in the distance determined before.

Figure 4.17 shows where the different measurement methods take place.

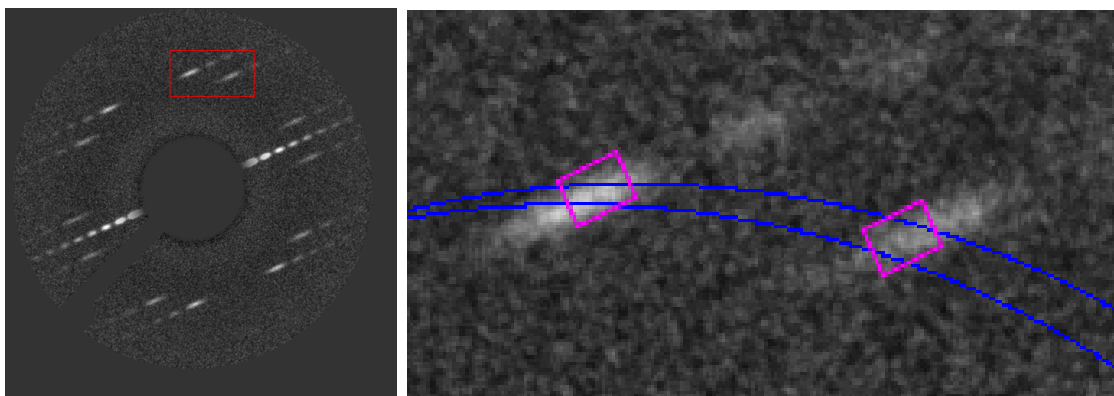


Figure 4.17: The right side shows a zoomed in view of the red rectangle in the left image. The measurement near the ellipse uses just the pixels between the blue lines. Which pixels are used depends on the distance to the tube axis. The measurement for the precise determination uses the pixels within the pink rectangles. This measurement is independent of the distance to the tube axis, which yields a more precise determination.

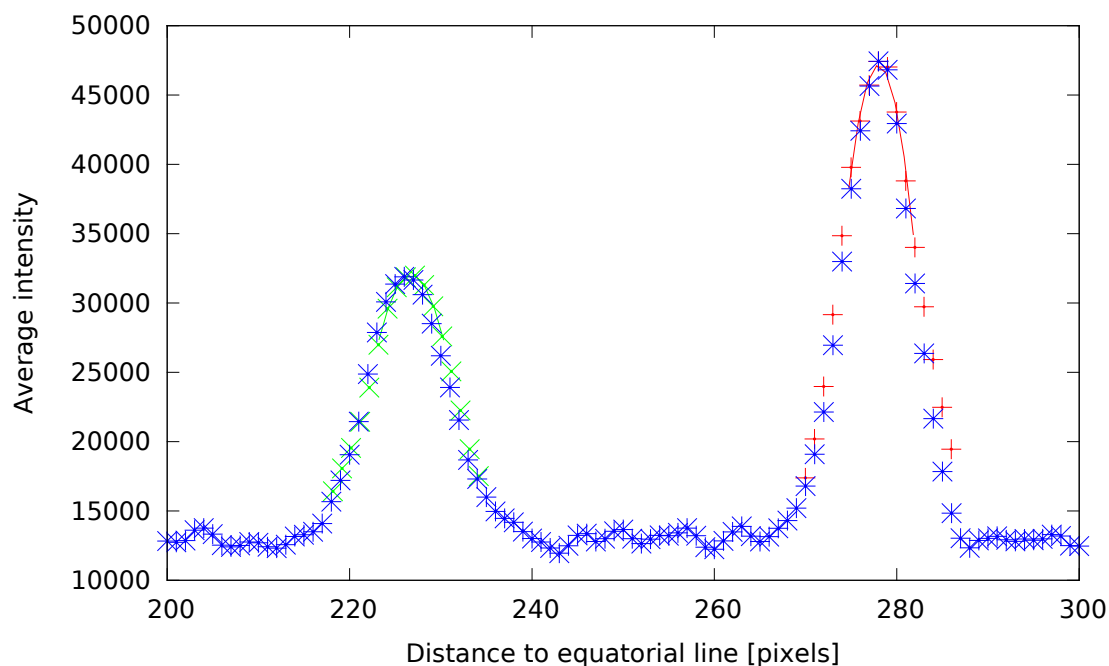


Figure 4.18: Average intensity related to the distance to the equatorial line measured in different ways: The blue points show the intensity measured between the blue lines in figure 4.17. The red and green points show the intensity measured in the pink rectangles in figure 4.17. The positions of the maxima differs slightly, however the effect is stronger in the images in section 5.1 and section 6.2. The lines show the fitted parabolas.

The intensity distributions are always averaged over the four quadrants. Pixels which are identified to be corrupted by the beamstopper are ignored.

Comparing the positions of the maxima in both measurement methods (cf. figure 4.18) show no significant deviations for this image. However in section 5.1 and section 6.2 images are presented, where the improvement of the accuracy is important.

## 4.6 Selection of the possible tubes

With the use of the distances of the layer lines to the equatorial line only the helical angle  $\alpha$  and therefore the ratio  $r = m/n$  of the chiral indices can be determined. Even for arbitrary precision of the distance determination, which is impossible for experimental data, the tube is not uniquely identified since different tubes may have the same helical angle (for example the (15, 8) and the (30, 16) tube possess the same helical angle).

The further analysis compares the diffraction pattern to simulation. But it is not

practical to simulate patterns for all tubes and parameters. Therefore the comparison is done only for tubes, which possess a ratio  $r_{theo}$  similar to the measured one.

#### 4.6.1 Estimation of the error of the measured $m/n$

To determine, which tubes have a “sufficiently similar” ratio  $r_{theo}$  to be simulated and compared to the experimental data, the error  $\Delta r$  in the measurement of the ratio  $r_{meas}$  has to be estimated. If the error is large, more tubes should be taken into account than for a ratio  $r_{meas}$  which could be determined very precisely.

At first the error in the determination of the layer line distances needs to be estimated to determine the uncertainty in the ratio. To obtain this error, the distances are determined for each quadrant separately. Therefore the intensity distribution for each spot using a rectangle (cf. figure 4.17) is calculated in each quadrant. The obtained intensity distributions for the spot of the first layer line are shown in figure 4.19.

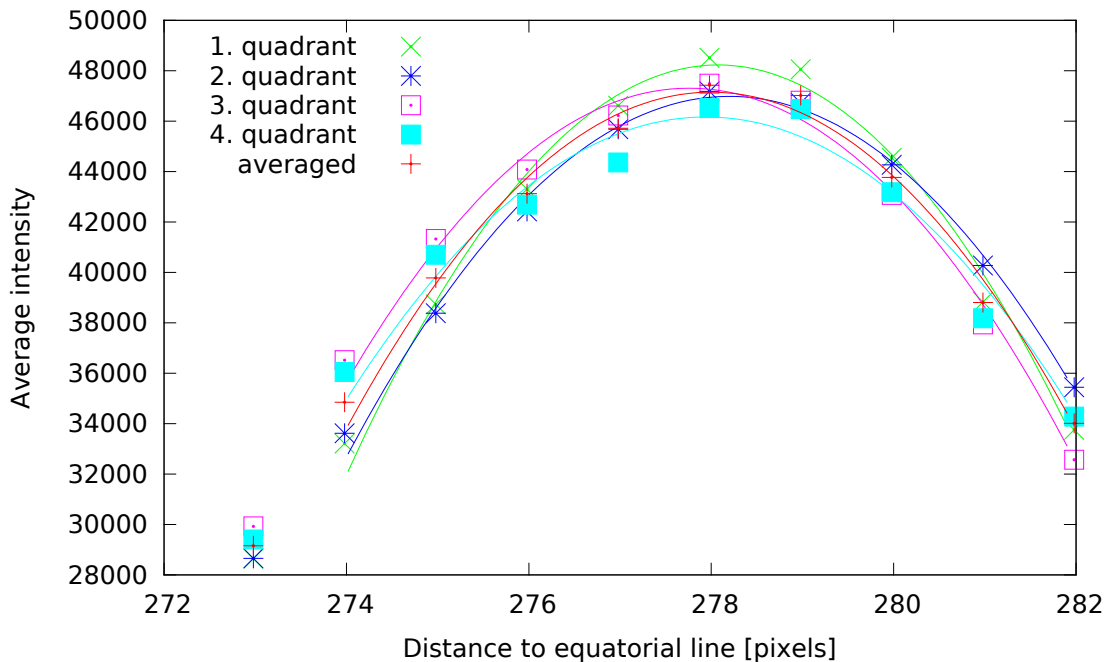


Figure 4.19: The intensities related to the distance to the equatorial line measured in rectangles at the spot of the first layer line of the image in figure 4.17 in the four quadrants and the mean of the quadrants are shown. The maxima of the fitted parabolas are not at the exact same position.

Now we have the distance measured in the averaged distribution and four values

from the quadrants. These are too few values for a statistical error estimation. Therefore the maximum deviation of the positions in the quadrants related to the position measured in the mean curve is taken as the error:

$$\Delta d_i = \max\{|d_i - d_i^q|\} \quad \text{with } q = 1, 2, 3, 4 \quad (4.21)$$

where  $d_i$  denotes the distance of layer line  $i$  measured in the mean and  $d_i^q$  denotes the distance of layer line  $i$  measured in the  $q$ th quadrant.

Then error propagation is applied which yields the following formula for the error  $\Delta r$  in the ratio  $r_{meas}$ :

$$\Delta r = \frac{\Delta d_2 + \Delta d_1}{2d_2 - d_1} \cdot \frac{\Delta d_1 + \Delta d_2}{2d_1 - d_2} \cdot r_{meas} \quad (4.22)$$

For the example discussed here the values in table 4.2 were obtained.

$d_1$	$\Delta d_1$	$d_2$	$\Delta d_2$	$r_{meas}$	$\Delta r$
278.02	0.26	226.76	0.17	0.5330	0.0020

Table 4.2: Measured values and their errors for the example of the simulated image.

#### 4.6.2 Score for the ratio

From table A.1 all combinations of chiral indices  $(n, m)$  are selected, whose ratio  $r_{theo} = m/n$  fulfills

$$|r_{theo} - r_{meas}| \leq 3\Delta r \quad (4.23)$$

The selected tubes are called ‘‘candidates’’ in the following.

Since the deviations between the theoretical ratio  $r_{theo}$  and the measured ratio  $r_{meas}$  vary for the candidates, it would be helpful to have a number, which takes these differences into account. This number is called ‘‘score’’  $S_r$  and is defined for the ratio as follows:

$$S_r = \exp\left(-0.5 \frac{(r_{theo} - r_{meas})^2}{(\Delta r)^2}\right) \quad (4.24)$$

The possible range for  $S_r$  is therefore  $[0, 1]$ . The value is higher for small deviations between the measurement and the theory. If the measured ratio could be determined quite accurately (small  $\Delta r$ ), the deviation is punished stronger than for imprecise measurements.

$n$	$m$	$d[\text{nm}]$	$\alpha[^\circ]$	$m/n$	$ r_{theo} - r_{meas} $	$S_r$
15	8	1.584	20.03	0.53333	0.00031	0.997
30	16	3.167	20.03	0.53333	0.00031	0.997
28	15	2.960	20.10	0.53571	0.00269	0.798
17	9	1.791	19.93	0.52941	0.00362	0.664
13	7	1.376	20.17	0.53846	0.00543	0.397
26	14	2.753	20.17	0.53846	0.00543	0.397

Table 4.3: Possible combinations for the chiral indices  $n$  and  $m$ .

Table 4.3 shows the candidates for the simulated example. Index combinations whose ratio is closest to the measured one have the highest score. The (15, 8) and the (30, 16) tube have the same ratio and therefore cannot be distinguished by measuring the layer line distances.

## 4.7 Comparison of the candidates to the simulation

In the following the set of possible tubes should be reduced further. This goal could be reached by analyzing the equatorial line as described by Hua Jiang *et al.* [15]. However that method is only valid for separate single-walled nanotubes, but not for bundles or multi-walled tubes, due to the fact that in these cases the equatorial lines interfere with each other. The herein introduced evaluation method is supposed to accomplish the analysis of bundles and multi-walled tubes though.

That is implemented by comparison of the intensity distribution of the measured layer lines and theoretically expected intensity distributions.

### 4.7.1 Correction of the center using the layer lines

The correction of the center of the diffraction pattern in section 4.5.3 works quite exactly in the direction of the tube axis. The precision in the direction of the equatorial line is lower, because the intensity distribution dependent on the distance to the equatorial line is changed only slightly by movement of the center along the equatorial line. That there is a change at all is caused by the measurement near the circle.

To improve the accuracy in the determination of the center along the direction of the equatorial line, here the intensity distribution on the layer lines is utilized. This cannot be done previously since the positions of the layer lines have to be known first.

Because for various tube numbers different layer lines are located, the correction of the center varies for differing numbers of tubes.

To obtain the optimal correction of the center, the intensity on the layer lines dependent on the distance to the tube axis is measured in all four quadrants separately. Now the correlations between the curves in the quadrants are calculated for various offsets of the  $x$ -axis to obtain the optimal offset. Thereby the curves of the quadrants “right” of the tube axis are compared to the “left” ones. This means, that the first quadrant is compared to the second and third and the fourth to the second and third as well.

Therefore one gets four estimations for the correction for each layer line. Since the estimations may vary strongly and contain outliers, for the optimum correction the median of all found estimates is chosen.

With this newly determined center the intensity on the layer lines is measured again. These intensity distributions are used for the following analysis steps.

### 4.7.2 Determination of the scale and the incidence angle

In order to be able to simulate the layer lines several parameters have to be known. On the one hand the chiral indices  $(n, m)$  for the candidates which are given by all means. On the other hand the scale, that connects the units in the simulation to sizes in pixels, and the angle  $\gamma$  between the tube axis and the incoming electron beam. These two parameters cannot be determined, respectively not with sufficient precision, by the experimenter in the TEM and therefore have to be obtained in the diffraction image.

As the distances of the layer lines to the equatorial line are already known, it is favorable to use them to determine the scale. Following the underlying theory the distance  $D$  in the reciprocal space of the first layer line and perpendicular incident is given by (cf. equation 2.82):

$$D_1 = a^* \cos \alpha \quad (4.25)$$

where  $a^*$  denotes the length of the reciprocal basis vector and  $\alpha$  the helical angle. The distance for the second layer line is (cf. equation 2.83)

$$D_2 = a^* \sin(30^\circ + \alpha) \quad (4.26)$$

and for the third (cf. equation 2.84)

$$D_3 = a^* \cos(30^\circ - \alpha) \quad (4.27)$$

The distances increase for non-perpendicular incidence (cf. section 2.4):

$$D_i^\gamma = D_i^{90^\circ} \frac{1}{\sin \gamma} \quad (4.28)$$

where  $\gamma$  denotes the angle between the incoming electron beam and the tube axis and  $D_i^{90^\circ}$  the distance of the  $i$ th layer line to the equatorial line for perpendicular incidence (i.e.  $\gamma = 90^\circ$ ).

The scale  $s$  of the image is therefore related to the incidence angle  $\gamma$  by the following formula:

$$s = \frac{D_i^{90^\circ}}{\sin(\gamma)d_i} \quad (4.29)$$

where  $d_i$  is the distance of the  $i$ th layer line to the equatorial line in the image in pixels, which was measured in the previous section.

However the angle is not known yet. But a second quantity is apparent in the images, which can be measured. The distance of the first maximum of a layer line to the tube axis can be obtained easily. Figure 4.20 pictures the intensity distribution in relation to the distance to the tube axis for the examined example, whereas it is averaged over the four quadrants, for all three layer lines.

Contrary to the measurement of the distances of the layer lines in this case a smoothing with a Gaussian filter is applicable to reduce noise. It can be done because the risk of maxima disappearing is only small, because the interval between the maxima on the layer lines is generally quite large. The filtering was accomplished by a Gaussian filter with  $\sigma = 7$ .

The distances of the said maxima to the tube axis moreover are dependent on the angle between the incident electron beam and the tube axis (cf. section 2.4). Figure 4.21 shows a simulated layer line for various angles.

For every given candidate one has two wanted parameters  $s$  and  $\gamma$  and for every layer line two measured parameters  $d_i$  and  $k_i$ , while  $k_i$  denotes the distance of the first maximum to the tube axis of the  $i$ th layer line, whereas the first maximum also constitutes the point of the highest intensity of the distribution.

For every layer line  $i$  the values for  $s_i$  and  $\gamma_i$  are numerically sought after in the following with the constraint, that the distances of the layer lines and the positions of the first maxima in the simulation have to concur with the measurement.

To be able to estimate the error of  $k_i$  one proceeds analogously to the error of  $d_i$ .

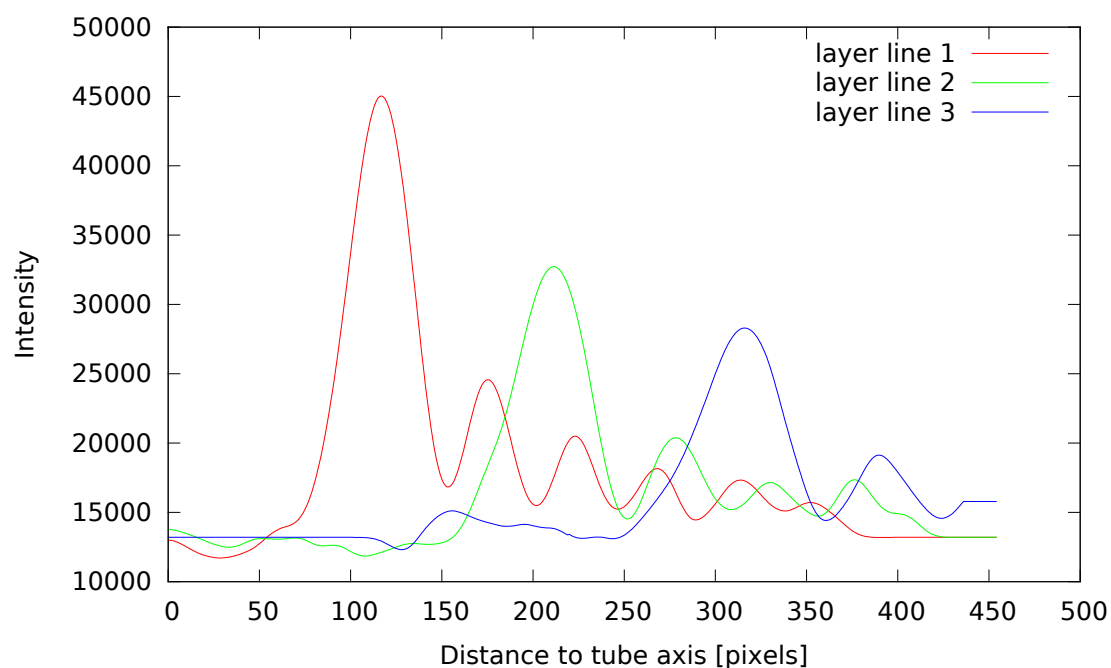


Figure 4.20: The intensities related to the distance to the tube axis on the layer lines measured in the preprocessed image averaged over the four quadrants. The curves were smoothed with a Gaussian filter with  $\sigma = 7$ .

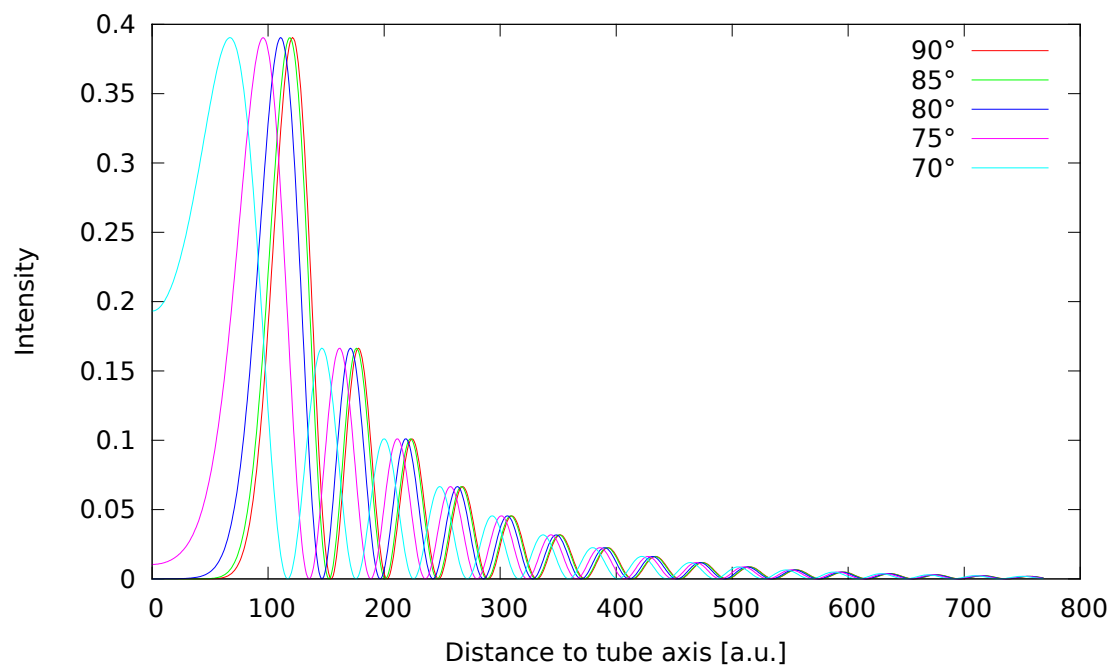


Figure 4.21: Simulated intensities on the first layer line of a (15,8) nanotube for various angles  $\gamma$  between the incoming electron beam and the tube axis.

The intensity distributions are measured separately in the four quadrants and the distances are determined in every quadrant. The error  $\Delta k_i$  equals then the largest discrepancy of one quadrant to the obtained position with the help of the averaged distribution. Figure 4.22 pictures the intensity curve of the second layer line in all four quadrants and the averaged graph.

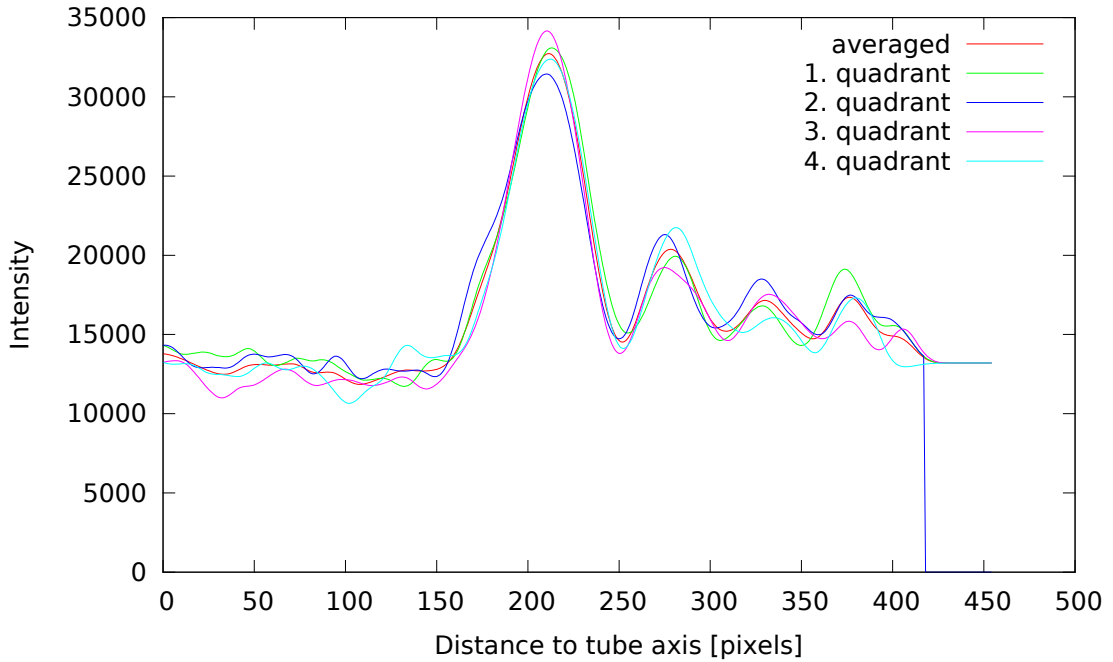


Figure 4.22: Intensity related to the distance to the tube axis on the second layer line measured in the four quadrants and the averaged curve. The curves were filtered with a Gaussian filter with  $\sigma = 7$ . The zero values in the second quadrant are caused by the beamstopper.

A parabola is fitted into the neighborhood of the highest point, to determine the maxima as precisely as possible. Table 4.4 shows the measured values for the distances of the diffraction spots on the layer lines to the tube axis with their errors.

$k_1$	$\Delta k_1$	$k_2$	$\Delta k_2$	$k_3$	$\Delta k_3$
117.0	1.1	211.5	0.9	315.9	2.1

Table 4.4: Measured distances to the tube axis and their errors for the simulated example image.

For every layer line the errors  $\Delta s_i$  and  $\Delta \gamma_i$  are estimated by calculating the angle  $\gamma$  and the scale  $s$  for  $d_i + \Delta d_i$  and  $k_i - \Delta k_i$  and  $d_i - \Delta d_i$  and  $k_i + \Delta k_i$ . The error is the largest divergence to the values calculated for  $d_i$  and  $k_i$ . One has to take into

account, that the scale  $s$ , the angle  $\gamma$  and also their errors are different for every candidate.

In order to evaluate the incidence angle for a candidate, the mean value is computed with the help of a weighting function. With the weights

$$w_i^\gamma = \frac{1}{(\Delta\gamma_i)^2} \quad (4.30)$$

one obtains the angle

$$\gamma = \frac{\sum_i \gamma_i w_i^\gamma}{\sum_i w_i^\gamma} \quad (4.31)$$

where  $i$  runs through all located layer lines. The error is then given by

$$\Delta\gamma = \sqrt{\frac{1}{\sum_i w_i^\gamma}} \quad (4.32)$$

Analogously the weights for the scale are defined:

$$w_i^s = \frac{1}{(\Delta s_i)^2} \quad (4.33)$$

The scale is given by

$$s = \frac{\sum_i s_i w_i^s}{\sum_i w_i^s} \quad (4.34)$$

and the error

$$\Delta s = \sqrt{\frac{1}{\sum_i w_i^s}} \quad (4.35)$$

Table 4.5 shows the estimated incidence angles and the scales and their errors for the candidates.

The specification of the error of the averaged angle and scale is only given to provide the user with information. It is not used in the following analysis.

### 4.7.3 Comparison of the maxima distances on the layer lines

All parameters to calculate simulated layer lines for the candidates are known now. The measured intensity distributions of the layer lines are to be compared to these in the following. For the comparison it is not the correlation that is utilized, as the intensity distributions of the real patterns are quite noisy very often (cf. section

Candidate	$\gamma_1[^\circ]$	$\Delta\gamma_1[^\circ]$	$s_1$	$\Delta s_1$	$\gamma_2[^\circ]$	$\Delta\gamma_2[^\circ]$	$s_2$	$\Delta s_2$
(13, 7)	82.1	0.7	0.1005	0.0001	82.9	1.1	0.1006	0.0002
(15, 8)	83.8	0.9	0.1003	0.0001	84.2	1.4	0.1002	0.0002
(17, 9)	85.5	1.4	0.1000	0.0001	85.5	2.2	0.0998	0.0002
(26, 14)	90.0	1.9	0.0996	0.0001	n.a.	n.a.	n.a.	n.a.
(28, 15)	90.0	1.0	0.0996	0.0001	n.a.	n.a.	n.a.	n.a.
(30, 16)	90.0	1.0	0.0997	0.0001	n.a.	n.a.	n.a.	n.a.

Candidate	$\gamma_3[^\circ]$	$\Delta\gamma_3[^\circ]$	$s_3$	$\Delta s_3$	$\gamma[^\circ]$	$\Delta\gamma[^\circ]$	$s$	$\Delta s$
(13, 7)	78.1	5.5	0.1008	0.0006	82.3	0.6	0.1005	0.0001
(15, 8)	87.2	7.6	0.1002	0.0008	83.9	0.8	0.1002	0.0001
(17, 9)	90.0	3.4	0.1011	0.0017	85.5	1.2	0.1000	0.0001
(26, 14)	90.0	14.4	0.0987	0.0002	90.0	1.9	0.0996	0.0001
(28, 15)	n.a.	n.a.	n.a.	n.a.	90.0	1.0	0.0996	0.0001
(30, 16)	n.a.	n.a.	n.a.	n.a.	90.0	1.0	0.0997	0.0001

Table 4.5: The estimated angles between the electron beam and the tube axis and the corresponding scales for the candidates and their errors.

6.1). Instead of that the distance between the first maximum – which is the highest at the same time – and the second maximum is evaluated.

The first maximum has been identified already in the last section. The second maximum  $o_i$  in the intensity distribution dependent on the distance to the tube axis has to fulfill the following conditions: First a change in the slope:

$$I_i(o_i) - I_i(o_i + 1) > 0 \quad \wedge \quad I_i(o_i) - I_i(o_i - 1) > 0 \quad (4.36)$$

where  $I_i(o_i)$  denotes the intensity with a distance of  $o_i$  to the tube axis. Moreover the distance to the tube axis has to be larger than for the first maximum:

$$o_i > k_i \quad (4.37)$$

The smallest possible value for  $o_i$  is the position of the second maximum on the  $i$ th layer line.

The probability remains small to find a maximum that in fact consists of noise by filtering with the broad Gaussian filter  $\sigma = 7$ .

The comparison between the simulation and the measurement is done between the distances of the second maxima to the first maxima not to the tube axis. Hereby the advantage is that this distance is less dependent on the incidence angle  $\gamma$  (cf. figure 4.21), therefore the error  $\Delta\gamma$  has less influence on this diagnose.

The interval  $p_i$  between the first and the second maximum on the  $i$ th layer line is

computed with use of the maxima, which were measured in the averaged graph:

$$p_i = k_i - o_i \quad (4.38)$$

To be able to evaluate the error, the gap between the maxima is also defined in the four quadrants individually.

$$p_i^q = k_i^q - o_i^q \quad (4.39)$$

The error  $\Delta p_i$  is the largest deviation between the distances, which were measured in the quadrants, and the distance, which was obtained in the averaged curve.

Analogously to the analysis of the distances of the layer lines also in this case a score is calculated for every candidate:

$$S_i^i = \exp\left(-0.5 \frac{(p_{i,theo} - p_{i,meas})^2}{(2\Delta p_i)^2}\right) \quad (4.40)$$

whereby  $S_i^i$  stands for the score for the  $i$ th layer line with reference to the analysis on the layer line.

The overall score of a candidate is computed via multiplication of the score for the layer line distances with the square root of the scores for the analysis on the layer lines:

$$S = S_r \prod_i \sqrt{S_i^i} \quad (4.41)$$

where  $i$  processes every layer line, for which the evaluation is supposed to be employed. The third layer line is not used by default, because the error is often very large in that case. The user however is able to decide which layer lines are to be utilized for the processing.

Candidate	$S_l^1$	$S_l^2$	$S_l^3$	$S_r$	$S$
(15, 8)	0.9747	0.9802	0.9997	0.9971	0.9746
(17, 9)	0.0388	0.3313	0.6125	0.6646	0.0753
(13, 7)	0.0211	0.3456	0.4865	0.3971	0.0339
(26, 14)	0.0000	0.0000	0.0009	0.3971	0.0000
(28, 15)	0.0000	0.0000	0.0002	0.7978	0.0000
(30, 16)	0.0000	0.0000	0.0000	0.9971	0.0000

Table 4.6: The scores of the candidates. The (15, 8) tube, which was used for the simulation, has the highest score. The score of the third layer line was not used for the calculation of the overall score.

Table 4.6 shows the scores for the candidates for the example. The (15, 8) tube gains the highest score, which is a good result since this tube was used for the simulation. The (30, 16) tube, which has a very high ratio score  $S_r$ , reaches a very low score in the comparison of the layer lines. This is caused by the fact, that  $S_r$  only takes the helical angle  $\alpha$  into account. This is equal for the (30, 6) and the (15, 8) tube. For the evaluation of the layer lines the diameter of the tube is important. Since the tubes differ strongly concerning this parameter, large differences in the score appear.

The example presented in this chapter was a diffraction pattern of quite high quality which could be analyzed easily for demonstration purposes.

# Chapter 5

## Test of the algorithm with various simulated images

In the previous chapter the functionality of the algorithm was presented with the help of a simple example. In this chapter it will be explained how the program behaves when images have low intensity layer lines, many tubes are present, the layer lines are broad and in special cases like “armchair” and “zig-zag” tubes.

### 5.1 Broad layer lines

In the following section a diffraction pattern is analyzed, in which the layer lines are relatively broad. Broad layer lines may cause problems, because they might overlap. In section 6.2 an experimental image with broad layer lines is shown. Table 5.1 shows the parameters utilized for the simulation.

Tube 1	Tube 2	$\gamma$	Noise $\sigma$	Noise ground	FWHM	$I_{max}$
(18, 12)	(21, 9)	85°	25 %	10 %	13.5 pixels	65 %

Table 5.1: Simulation parameters of the image in figure 5.1.

Figure 5.1 shows at the top a diffraction image of a bundle of two nanotubes with broad layer lines which could be challenging the algorithm.

The preprocessing described in the previous chapter works without any problems. The center is found well and also the radius of the circle, near which the intensity related to the distance to the equatorial line is measured, is found.

Due to the fact that for the normalization of the intensity, i.e. the removal of the undiffracted electron beam, the fitted curve of the intensity distribution is used (c.f. section 4.4), the diffraction spots are not diminished higher-than-average. This

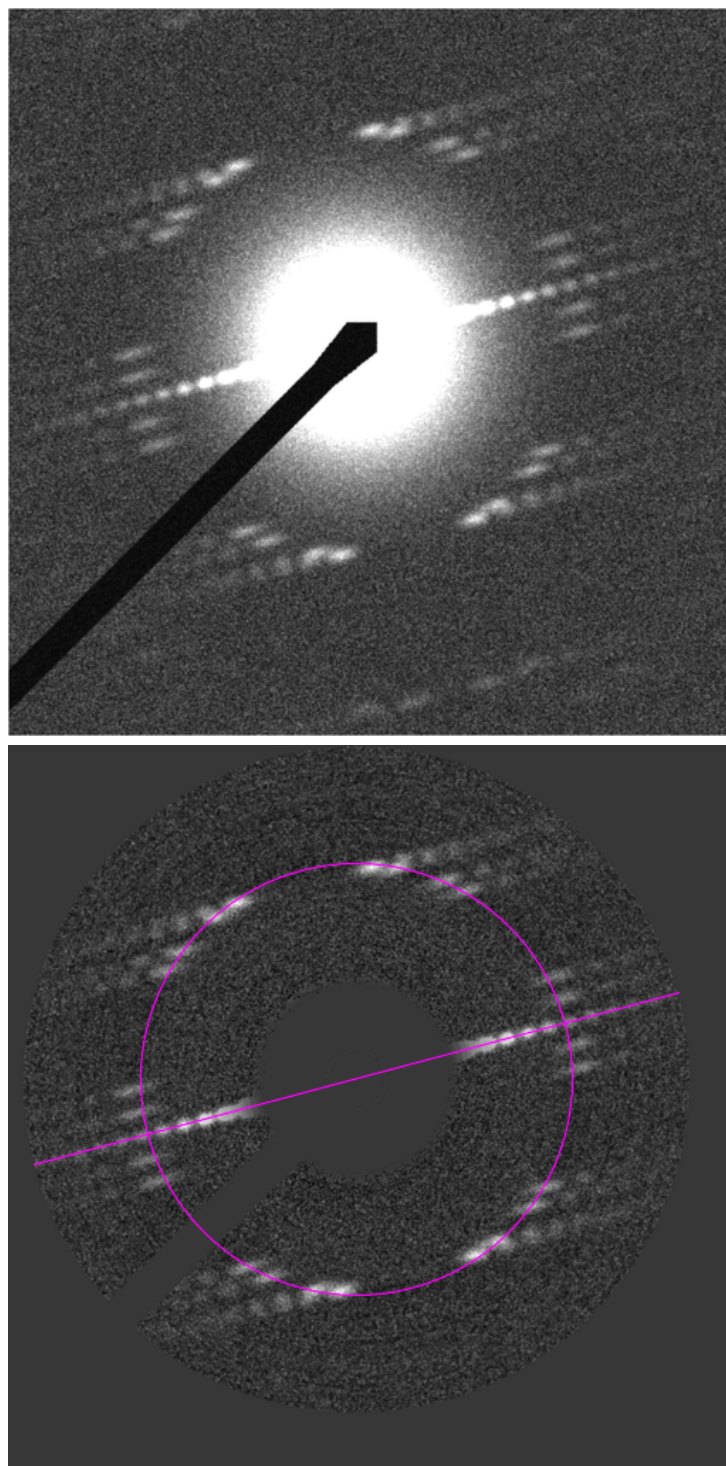


Figure 5.1: *Top*: Simulated image of a bundle of two carbon nanotubes (18, 12) and (21, 9) with broad layer lines. *Bottom*: The image after preprocessing: The pink line shows the position of the equatorial line found by the algorithm. The pink circle indicates where the measurement for the distances of the layer lines takes place.

would be the case for bright and broad spots, which are present in this example. Like in figure 4.6 a dark circle would appear.

The algorithm was able to delineate the beamstopper well. The angle of the equatorial line is found with an error of  $0.23^\circ$  with the rough method. After the correction the error amounts to  $0.1^\circ$ .

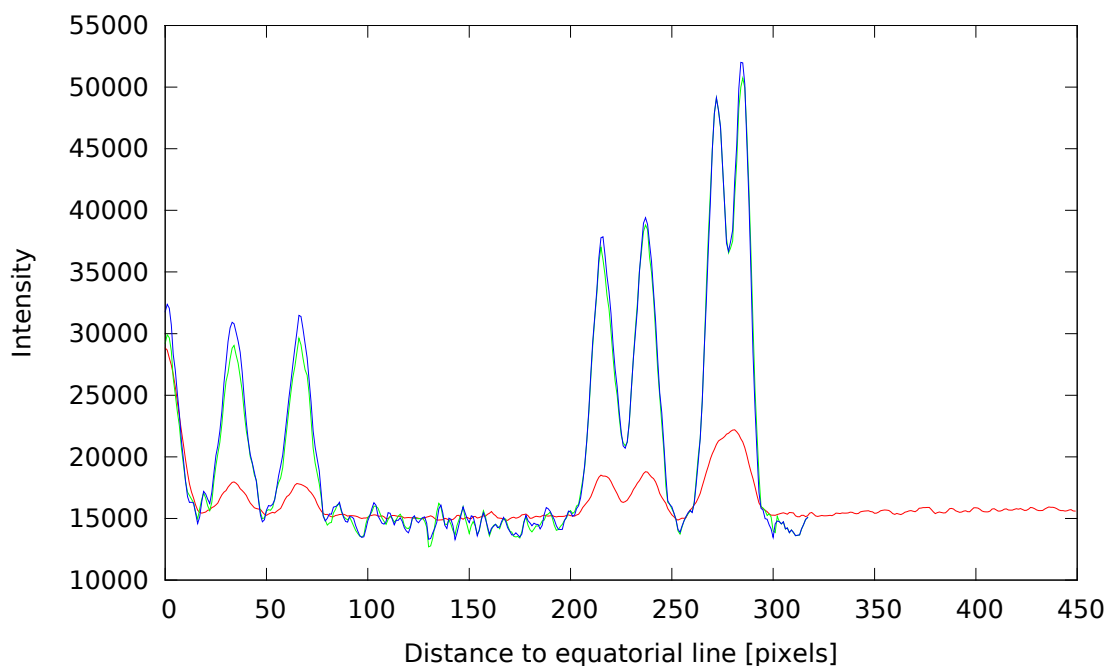


Figure 5.2: *Red*: The intensity related to the distance to the equatorial line measured in the whole image. The first layer lines of the two tubes cannot be distinguished. *Green*: Intensity measured near the circle in figure 5.1 (bottom). The first layer lines can be distinguished. *Blue*: The intensity of the maxima further increases using the measurement near an ellipse.

The red curve in figure 5.2 shows the intensity related to the distance to the equatorial line measured in the whole image. The second layer lines and the third layer lines of the tubes can be identified easily and are distinguishable. But the first layer lines are merged to one maximum due to their small difference in the distance and their width.

In the measurement near the circle in figure 5.1 (green curve in figure 5.2), the first layer lines generate two maxima and can be distinguished in the intensity distribution. With the measurement near the ellipse (blue curve) the maxima reach higher intensities.

Figure 5.3 shows, why the layer lines can be separated. Since the first maxima on the layer lines, which possess the highest intensity within the layer line, are located

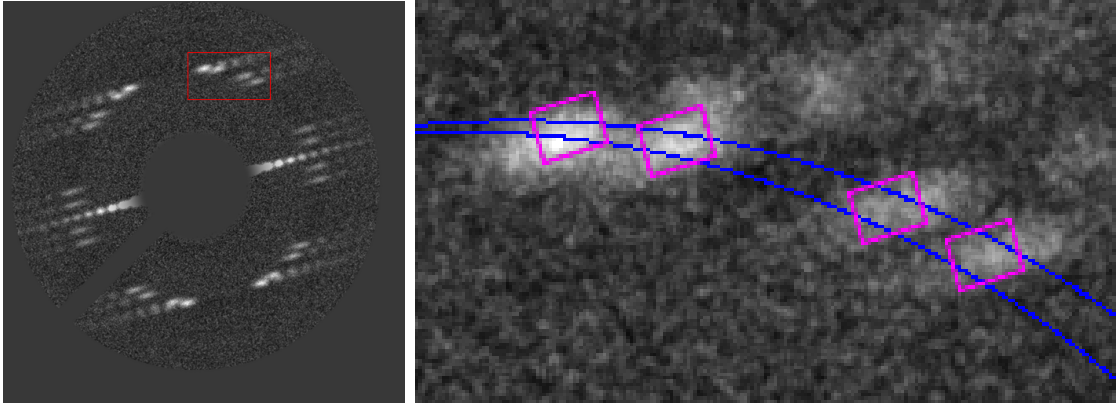


Figure 5.3: The right side shows a zoomed in view of the red rectangle in the left image. The diffraction spots overlap in the direction of the tube axis. The measurement near the circle uses just the pixels between the blue lines. Which pixels are used depends on the distance to the tube axis, which is helpful to distinguish the diffraction spots. The measurement for the precise determination uses the pixels within the red rectangles. This measurement is independent from the distance to the tube axis, which leads to a more precise determination.

at different distances to the tube axis, an intensity minimum between the spots occurs, when the measurement takes place along the circle respectively the ellipse. This example proves, that it is a big advantage to measure the intensity related to the distance to the equatorial line only near a circle respectively an ellipse through the diffraction spots.

The algorithm identifies six maxima in this curve. These can be combined to two tubes referring to the conditions in section 4.5.5. Table 5.2 shows the positions of the located maxima and their assignment to the layer lines.

Maximum	$M_1$	$M_2$	$M_3$	$M_4$	$M_5$	$M_6$
Distance	284.44	272.31	237.13	215.79	66.59	33.53
Layer line	$D_1^1$	$D_1^2$	$D_2^2$	$D_2^1$	$D_3^1$	$D_3^2$

Table 5.2: Positions of the maxima measured in the blue curve in figure 5.2 and their assignment to the tubes.  $D_i^j$  denotes the  $i$ th layer line of the  $j$ th tube.

To obtain the distances to the equatorial line more precisely, the intensity distribution related to the distance to the equatorial line is calculated in rectangles around the diffraction spots determined on the ellipse as shown in section 4.5.6. It can be seen in figure 5.3, that the areas of the rectangles for the determination of the distances of the first layer lines do not overlap, though the diffraction spots overlap in the direction of the tube axis.

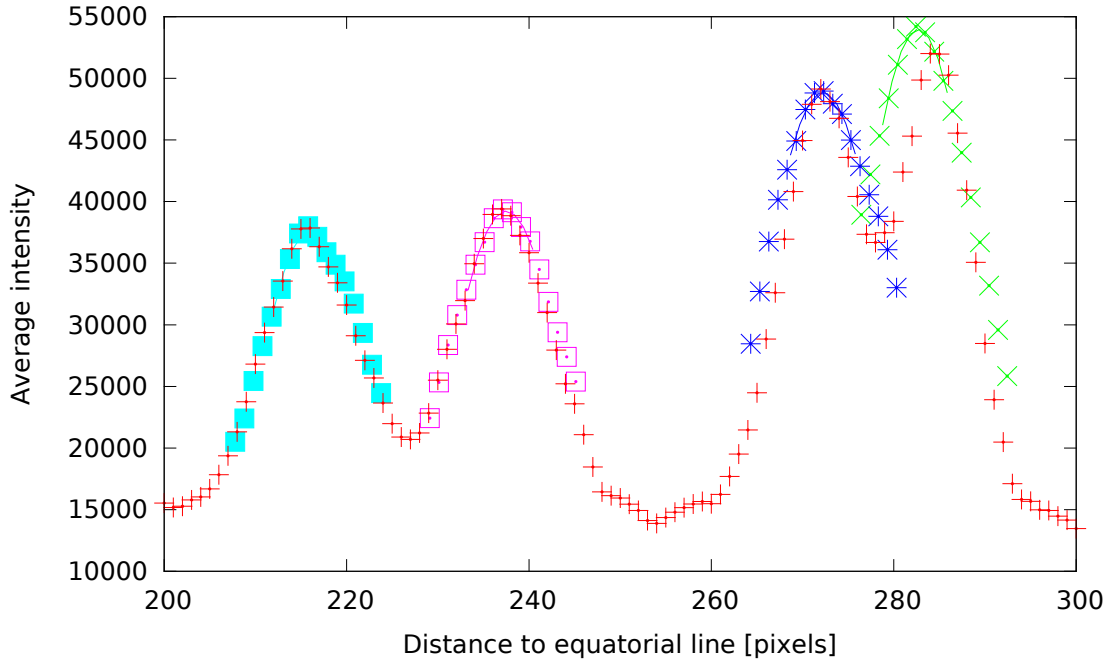


Figure 5.4: The intensity measured near the ellipse (red) and measured in the rectangles. Especially for the maximum with the largest distance (green), the aberration is big and cannot be omitted.

Figure 5.4 shows the intensity distribution measured with the use of the pixels near the ellipse and measured in rectangles. Especially for the maximum with the highest distance to the equatorial line a large discrepancy between the measurements appears, which cannot be omitted. Table 5.3 shows the values measured in the rectangles, the corresponding errors, which were determined by the distributions in each quadrant, and the obtained ratio  $r_{meas} = m/n$ .

Tube	$D_1$	$\Delta D_1$	$D_2$	$\Delta D_2$	$D_3$	$\Delta D_3$	$r_{meas}$	$\Delta r$
1	282.69	0.28	216.09	0.65	66.75	0.73	0.4280	0.0038
2	272.24	0.85	237.50	0.72	33.51	0.63	0.6606	0.0085

Table 5.3: Distances of the layer lines to the equatorial line with their errors and the measured ratios  $r_{meas} = m/n$  and their errors.

The possible tubes can be looked up in table A.1.

By comparison of the measured intensity distributions on the layer lines and simulated layer lines the scores for the tubes in table 5.4 and table 5.5 are obtained.

In spite of the large width of the layer line the (21, 9) and the (18, 12) tube, which were simulated, achieve by far the highest score compared to the other candidates. For these tubes an incidence angle of the incoming electron beam of  $84.7^\circ \pm 1.1^\circ$

Candidate	$S_l^1$	$S_l^2$	$S_l^3$	$S_r$	$S$
(21, 9)	0.9647	0.9025	0.9903	0.9974	0.9306
(23, 10)	0.4120	0.4661	0.9298	0.6736	0.2952
(19, 8)	0.0606	0.8938	0.9896	0.6574	0.1529
(24, 10)	0.1145	0.3538	0.9020	0.3283	0.0661
(26, 11)	0.0028	0.1149	0.8075	0.8097	0.0144
(28, 12)	0.0000	0.0327	0.7126	0.9974	0.0009
(30, 13)	0.0000	0.0085	0.6256	0.7836	0.0000
⋮	⋮	⋮	⋮	⋮	⋮

Table 5.4: Candidates and their scores for the first tube.

Candidate	$S_l^1$	$S_l^2$	$S_l^3$	$S_r$	$S$
(18, 12)	0.9583	0.9676	0.9990	0.9368	0.9021
(17, 11)	0.3947	0.9450	0.9554	0.7278	0.4445
(20, 13)	0.4319	0.6021	0.9549	0.8234	0.4199
(19, 13)	0.9146	0.7433	0.9810	0.3765	0.3105
(21, 14)	0.1435	0.3637	0.8848	0.9368	0.2140
(22, 15)	0.0411	0.1918	0.7905	0.4542	0.0403
(22, 14)	0.0372	0.2608	0.8297	0.3602	0.0355
⋮	⋮	⋮	⋮	⋮	⋮

Table 5.5: Candidates and their scores for the second tube.

respectively  $84.7^\circ \pm 1.5^\circ$  is obtained, which also matches the simulated angle of  $85^\circ$  well.

All in all one can say, that the algorithm is able to deal with diffraction patterns with broad layer lines, even in some cases where the layer lines overlap to some extent.

## 5.2 Low intensity of the reflections

In this section a diffraction pattern with layer lines of low intensity is analyzed. The used parameters are given in table 5.6. The diffraction spots in the diffraction pattern in figure 5.5 are barely visible to the naked eye.

Tube 1	$\gamma$	Noise $\sigma$	Noise ground	FWHM	$I_{max}$
(13, 7)	$80^\circ$	25 %	10 %	6 pixels	15 %

Table 5.6: Parameters of the simulation for the image in figure 5.5.

It is still no problem for the algorithm to find the radius of the circle for the distances measurement in this image.

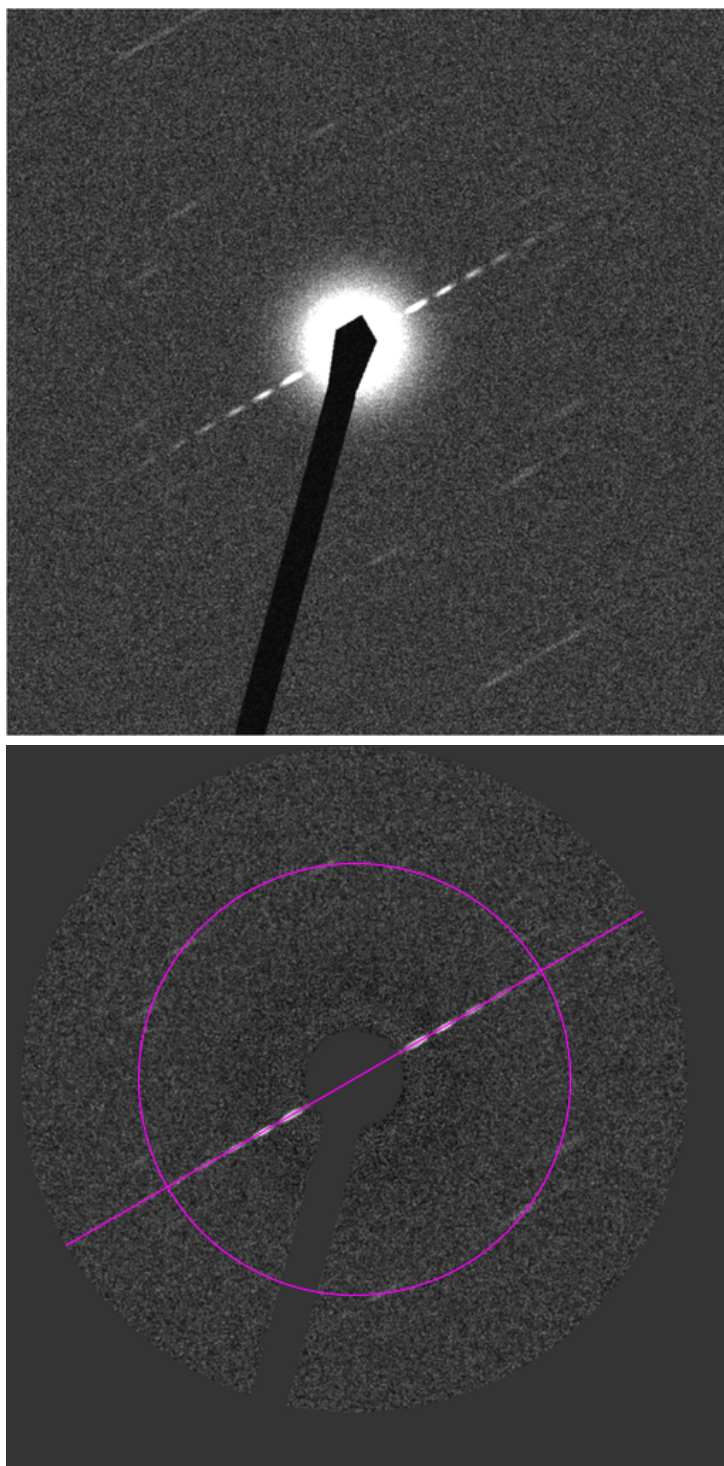


Figure 5.5: *Top*: Simulated image of a (13,7) carbon nanotube with low intensity. *Bottom*: The image after preprocessing. The pink line shows the position of the equatorial line found by the algorithm. The pink circle indicates where the measurement for the distances of the layer lines takes place.

The helical angle  $\alpha$  respectively the ratio  $m/n$  can be determined quite accurately, even though the main spot of the second layer line in the third quadrant is covered by the beamstopper. The measurement in the other quadrants is sufficient for the analysis.

The measurement of the distances of the maxima on the layer lines to the tube axis causes more problems than the detection of the distances of the layer lines to the equatorial line. Especially the measurement on the second layer line is imprecise since the intensity on this line is lower than on the first layer line.

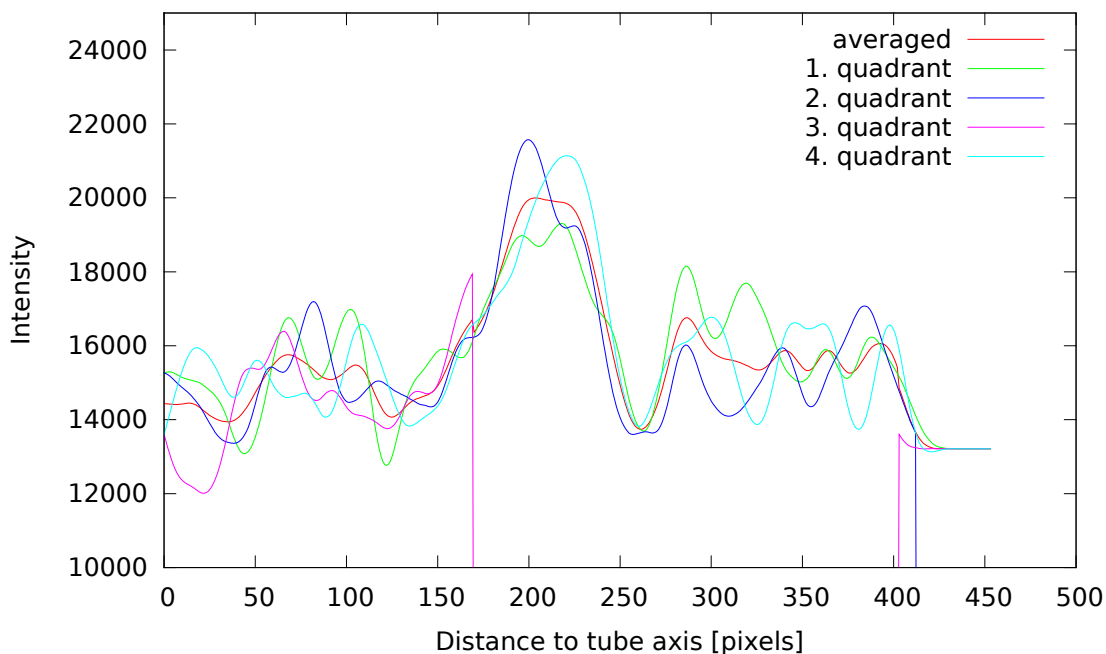


Figure 5.6: The intensity related to the distance to the tube axis measured on the second layer line in the four quadrants and the mean of the quadrants.

The first and second maxima can be identified in figure 5.6 at around 200 pixels respectively 280 pixels, but the positions vary strongly in the quadrants. This leads to a large error in the determination of the distances and therefore uncertainty in the comparison between simulation and measurement. Table 5.7 shows the candidates with the highest scores for the example. The (13, 7) tube, which was simulated, still has the highest score, but the gap to the other tubes is small.

For the chosen intensity and noise level the algorithm does not yield the correct result for all simulated images. Simulated images with the same parameters differ because the noise is generated randomly each time. Out of 20 simulated images the right tube reached the highest score 15 times. Even in the cases, where it did not

Candidate	$S_l^1$	$S_l^2$	$S_l^3$	$S_r$	$S$
(13, 7)	0.9451	0.6783	n.a.	0.9995	0.8003
(11, 6)	0.7361	0.9917	n.a.	0.8821	0.7537
(15, 8)	1.0000	0.2559	n.a.	0.9515	0.4813
(17, 9)	0.9687	0.0830	n.a.	0.8455	0.2397
(9, 5)	0.3720	0.3203	n.a.	0.4978	0.1718
(19, 10)	0.9033	0.0260	n.a.	0.7332	0.1124
(18, 10)	0.9318	0.0376	n.a.	0.4978	0.0932
(20, 11)	0.8520	0.0118	n.a.	0.7221	0.0723
$\vdots$	$\vdots$	$\vdots$	$\vdots$	$\vdots$	$\vdots$

Table 5.7: Candidates and their scores for the image in figure 5.5.

have the highest score, the right tube was in the top ten. In two of the five cases where the analysis failed, it gained the highest score, when only the first layer line was taken into account for the comparison between simulation and measurement. Additionally it should be noticed that the helical angle  $\alpha$  could be determined quite accurately each time for these parameters.

This example shows, that the algorithm is able to analyze images correctly, even when the layer lines are barely visible to the naked eye.

## 5.3 Special cases of nanotubes

This section describes the behavior of the algorithm for the special cases of a “zigzag” and an “armchair” nanotube. As mentioned in section 2.3.2 their diffraction patterns possess special features, therefore they are examined separately.

### 5.3.1 “Zigzag” nanotube

The simulated diffraction image shown in figure 5.7 can be analyzed by the algorithm completely automatically. Table 5.8 denotes the parameters used for the simulation.

Tube	$\gamma$	Noise $\sigma$	Noise ground	FWHM	$I_{max}$
(14, 0)	83.5°	20 %	10 %	10 pixels	50 %

Table 5.8: Parameters for the simulation of the image in figure 5.7.

The special characteristic is the overlapping of the second and third layer line. This can lead to extinction of these lines in some cases [4]. But the extinction can only occur in the case of perpendicular incidence of the electron beam. For example

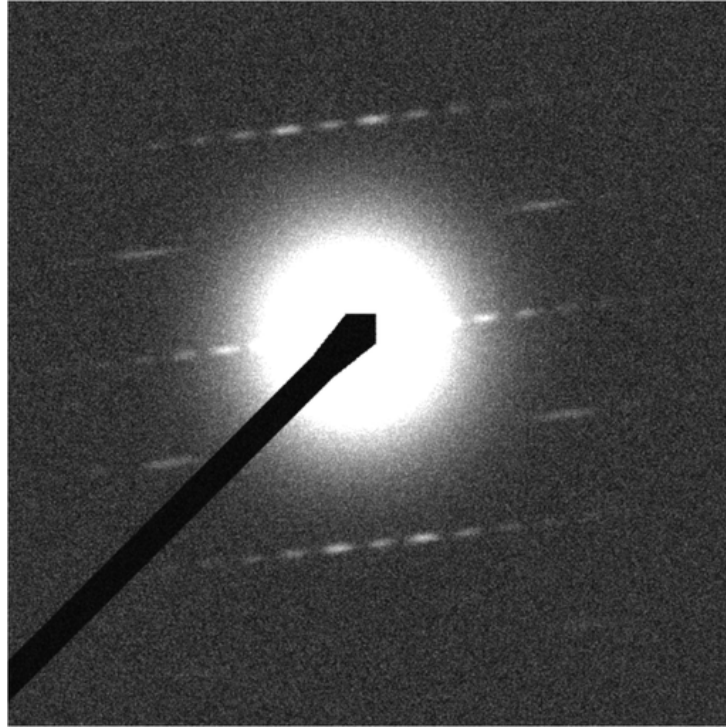


Figure 5.7: Simulated image of a  $(14, 0)$  “zigzag” tube: The second and the third layer line overlap but are observable. The first layer line possesses a maximum on the tube axis, whose intensity is decreased caused by the non perpendicular ( $\gamma = 83.5^\circ$ ) incidence angle.

for a  $(15, 0)$  tube the second layer line can easily be observed at an deviation of  $4^\circ$  from the perpendicular incidence. Therefore in practice an extinction is quite unlikely. For example the deviation from the perpendicular incidence amounts to  $23^\circ$  respectively  $10^\circ$  for the experimental images presented in chapter 6.

If the layer lines are not extinguished, the overlapping will cause no problem, since the third layer line is not needed for the analysis. Table 5.9 shows the measured distances of the layer lines to the equatorial line and the following ratio  $r_{meas}$ .

$D_1$	$\Delta D_1$	$D_2$	$\Delta D_2$	$D_3$	$\Delta D_3$	$r_{meas}$	$\Delta r$
296.79	0.45	148.15	0.24	n.a.	n.a.	-0.0011	0.0016

Table 5.9: Distances of the layer lines to the equatorial line with their errors and the measured ratio  $r_{meas} = m/n$  and its error.

It should be noted, that after this step of the analysis it is already evident, that the tube is a “zigzag” tube. Assuming a maximum chiral index  $n_{max} = 50$ , the tube  $(50, 1)$  has the closest ratio  $r = 0.02$  to the measured one, except for the “zigzag” tubes. Even this tube is far beyond the error limits. The determination whether it

is a “zigzag” tube can therefore be done quite unambiguously.

To decide which “zigzag” tube is observed, the intensity distribution on the layer lines is analyzed. Also here the “zigzag” tube is a special case, since the first layer line is dominated by a Bessel function of order zero, this means at perpendicular incidence ( $\gamma = 90^\circ$ ) the highest maximum has zero distance to the tube axis. When the incidence angle is reduced, the intensity of the maximum decreases until it completely vanishes but its position stays at the tube axis.

At the used incidence angle  $\gamma = 83.5^\circ$  the maximum is still visible, but the intensity of the second maximum is already higher. Since the position of the first maximum does not change for various incidence angles, the second maximum is used for the determination of the angle. The algorithm recognizes this case by the position of the first maximum (very close to the tube axis) and automatically uses the second maximum.

With that the angle can be detected well and a comparison between the simulation and the measurement can be done. This yields the results shown in table 5.10.

Candidate	$S_l^1$	$S_l^2$	$S_l^3$	$S_r$	$S$
(14, 0)	0.9943	0.9976	n.a.	0.9899	0.9859
(18, 0)	0.1157	0.8552	n.a.	0.9899	0.3114
(15, 0)	0.0453	0.9959	n.a.	0.9899	0.2104
(13, 0)	0.0339	0.9682	n.a.	0.9899	0.1793
(19, 0)	0.0010	0.8069	n.a.	0.9899	0.0280
$\vdots$	$\vdots$	$\vdots$	$\vdots$	$\vdots$	$\vdots$

Table 5.10: Candidates and their scores for the image in figure 5.7.

The simulated (14, 0) tube reaches the highest score with a large gap to the second best, therefore the analysis works well.

### 5.3.2 “Armchair” nanotube

In the case of a nanotube with “armchair” structure, the first and the second layer line overlap, the third layer line overlaps with the equatorial line. This means, that only one layer line can be detected.

The algorithm cannot deal with this case, since it always needs two layer lines for the analysis, because no ratio  $m/n$  can be calculated with the use of one layer line. Additionally the diffraction pattern depends on the orientation  $\phi$  of the nanotube in this case [4]. Therefore an additional degree of freedom appears. For these reasons the algorithm is not able to analyze diffraction patterns of “armchair” tubes.

Nevertheless the simulation, which is integrated in the program, might be useful to apply a manual comparison between an experimental diffraction pattern and the theoretical image.

## 5.4 Bundle of tubes

In this section it will be shown, that the algorithm is able to analyze diffraction patterns of bundles of many tubes, if the quality of the image is high. Figure 5.8 shows such an image. The used parameters are given in table 5.11.

Tube 1	Tube 2	Tube 3	Tube 4	Tube 5
(13, 7)	(17, 15)	(15, 11)	(26, 11)	(21, 3)
$\gamma$	Noise $\sigma$	Noise ground	FWHM	$I_{max}$
87°	10 %	10 %	4 pixels	200 %

Table 5.11: Parameters of the simulation for the image in figure 5.5.

Figure 5.9 shows the intensity distribution related to the distance to the equatorial line measured near an ellipse. Since the layer lines differ significantly in their intensity and not every diffraction spot is matched equally well by the ellipse, the height of the maxima in the intensity distribution varies strongly. This example shows, why it is reasonable to select the maxima not only by their absolute height but primarily by their slope.

In this example all tubes are detected correctly. Except for the (13/7) tube the gaps in the scores between the candidates with the highest respectively second highest scores are huge.

In [4] real pictures are presented, which possess similar quality.

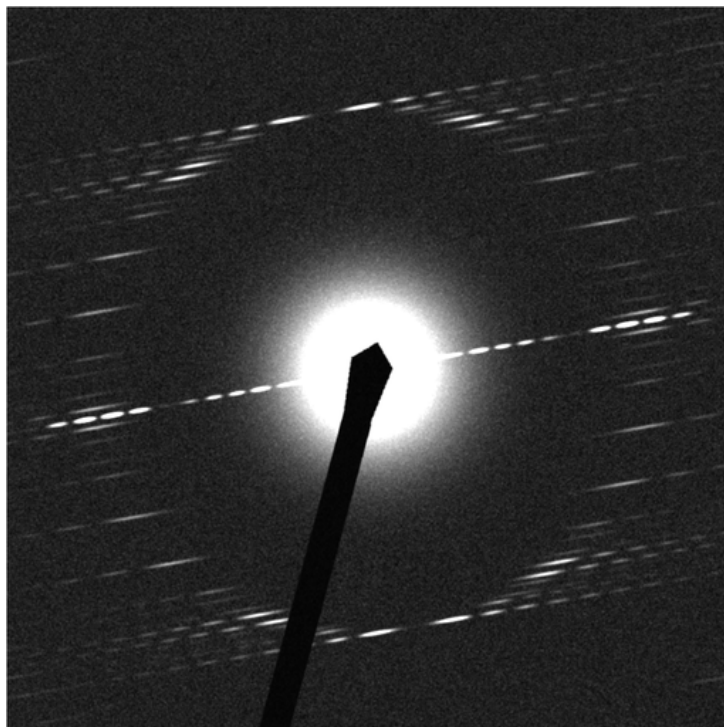


Figure 5.8: Simulated image of a bundle of  $(13, 7)$ ,  $(17, 15)$ ,  $(15, 11)$ ,  $(26, 11)$  and  $(21, 3)$  nanotubes of high quality.

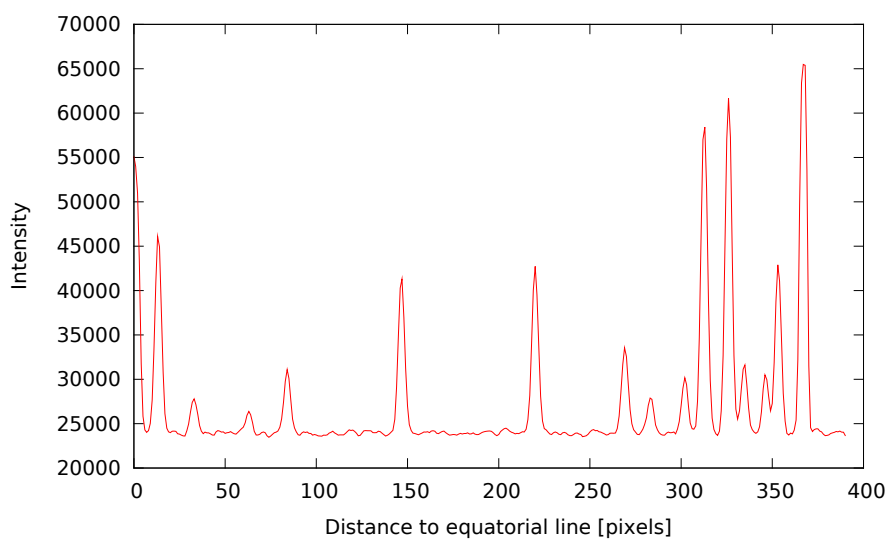


Figure 5.9: Intensity related to the distance to the equatorial line measured near an ellipse through the diffraction spots. The maxima vary strongly in their intensity.



# Chapter 6

## Analysis of experimental diffraction patterns

In this chapter the algorithm is applied to two experimental diffraction patterns. Experimental patterns may differ significantly depending on which electron microscope and parameters were used. The algorithm has to be able to analyze patterns with different properties, which is a main challenge for the algorithm design.

Though the simulation is similar to real images, there are still preprocessing steps, which have to be added for real images, since some features, which are treated, are not implemented in the simulation.

### 6.1 Single-walled tube

The image presented in this section (cf. figure 6.1) was taken at the University of Regensburg in the group of Professor Josef Zweck by Christian Huber. It is special because it was also analyzed by hand by Christian Huber in his diploma thesis [16] and the results can therefore be compared.

The size of the image is  $1024 \times 1024$  pixels. It was taken by a digital camera in the TEM.

#### 6.1.1 Noise reduction

In this image single points or small regions exist, which possess significantly higher or lower energy than their environment. These do not appear in the simulation since the noise is smoothed there with a Gaussian filter. These corrupted points and areas have to be detected to avoid perturbation of the further analysis steps.



Figure 6.1: Experimental diffraction pattern of a single-walled carbon nanotube taken at the University of Regensburg: The contrast and intensity are strongly enhanced, otherwise the diffraction spots are not visible.

To decide whether a pixel is corrupted, the number of neighbors  $nb_{dif}$ , which possess an intensity which differs from the intensity of the looked at pixel by at least a factor  $f_{min}$ , is estimated.

To detect single corrupted pixels, the four direct neighbors are evaluated. If the intensity of all of these neighbors differs at least by a factor  $f_{min} = 1.1$  from the intensity of the examined pixel, the intensity of the pixel is set to the average intensity of the neighbors.

To detect not just single pixels but also small areas, additionally the eight closest neighbors are taken into account. The number of  $nb_{dif}$  has to be at least five for a factor  $f_{min} = 1.3$  to detect the pixel as corrupted. Here the condition for the neighbors is relatively weak, but the difference in the intensity has to be huge.

To find also defects with a size of two pixels, again the neighborhood containing eight pixels is observed with a minimum  $nb_{dif}$  of seven using the factor  $f_{min} = 1.15$ . Since the image changes after a pixel was corrected, the search has to be done after the correction again, unless no more corrupted samples are found. Figure 6.2 shows

a detail of the image before and after the noise reduction. Many of the obviously corrupted points are removed.

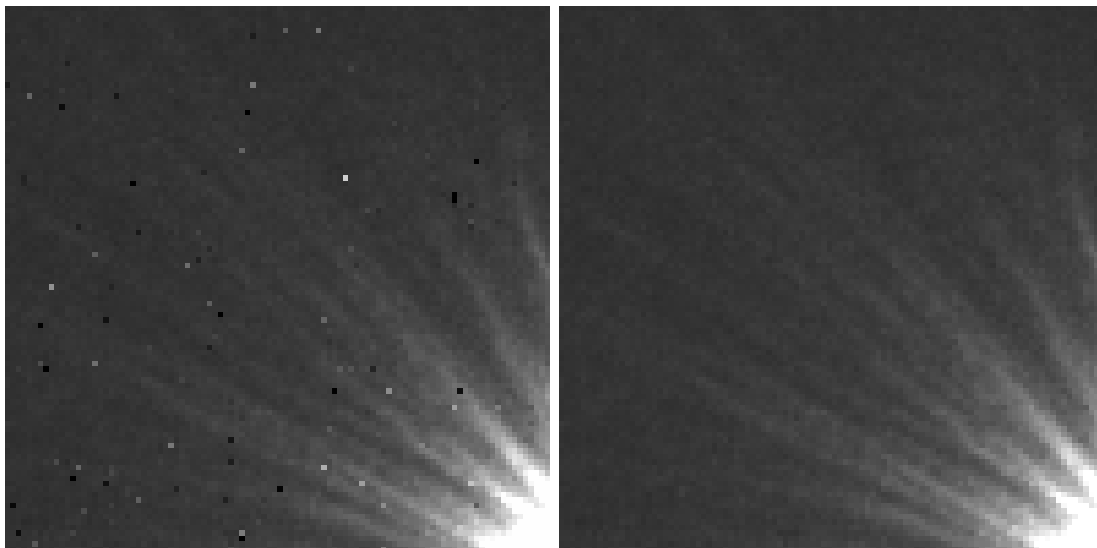


Figure 6.2: Enlarged part of figure 6.1: *Left*: The original image with corrupted pixels. *Right*: The image after the noise reduction.

### 6.1.2 Rough detection of the center

The automatic determination of the rough center of the diffraction pattern does not work correctly for this image. As described in section 4.2 the algorithm uses the undiffracted electron beam for the center estimation.

However the undiffracted electron beam almost disappears in this image at one side, because it is covered asymmetrically by the beamstopper. Moreover its shape is not uniform but star-shaped.

The failure of the automatic determination does not represent an unresolvable problem since the program allows the user to determine the rough center manually. For the estimation by hand the star-shape can be utilized since the rays should all direct to the center.

It is alright, if the determination is not absolutely exact since the correction of the center (cf. section 4.5.3) is done afterwards.

### 6.1.3 Parasitic stripe of high intensity

As can be seen in figure 6.1 the diffraction pattern contains a bright stripe. This stripe does not represent the equatorial line but is a consequence of parasitic diffracted

electrons. This stripe is not part of the simulation.

This stripe needs to be detected and removed otherwise it would be considered the equatorial line or a diffraction spot. For the detection of the stripe the snake algorithm (cf. section 3.2) is used.

For the initialization the rough position of the stripe has to be known. For this the extraordinary high intensity of the stripe near the image borders is utilized. The algorithm for the initialization works as follows.

0. Set  $q = 1$ , which describes the distance to the border of the image.
1. Calculate average intensity  $\bar{I}(q)$  of all pixels with distance  $q$  to the image borders.
2. Search for pixels  $(x, y)$  with distance  $q$  to the border, with intensity  $I(x, y) > 1.5 \bar{I}(q)$ .
3. Check for all found pixels  $(x, y)$  if two pixels in all four directions also exceed  $1.5 \bar{I}(q)$ . If not, reject pixel.
4. Search for direction of stripe by calculation of average intensity in all directions. The stripe direction is the angle with the highest average intensity measured on a line of length 150 pixels.
5. If average intensity on this line is smaller than  $1.5 \bar{I}(q)$ , reject pixel.
6. If no pixel was found, which fulfills all conditions, increase  $q$  by one and go back to step 1.

Step 3 should prevent the algorithm from assuming a noisy pixel as part of the bright stripe.

Then the active contour is initialized as a rectangle with the determined angle reaching from the image border to 20 pixels before the previously estimated image center. The distance between the nodes of the active contour is 5 pixels. The gradient is calculated as described in section 4.3.2.

$\omega_m$	$\omega_{\delta I}$	$\omega_g$	$\omega_{\delta G}$	$\omega_c$	$\omega_b$	<i>size</i>
-5.0	0.1	-8.0	3.0	1.0	1.0	10

Table 6.1: Parameters of the snake algorithm for the delineation of the bright stripe.

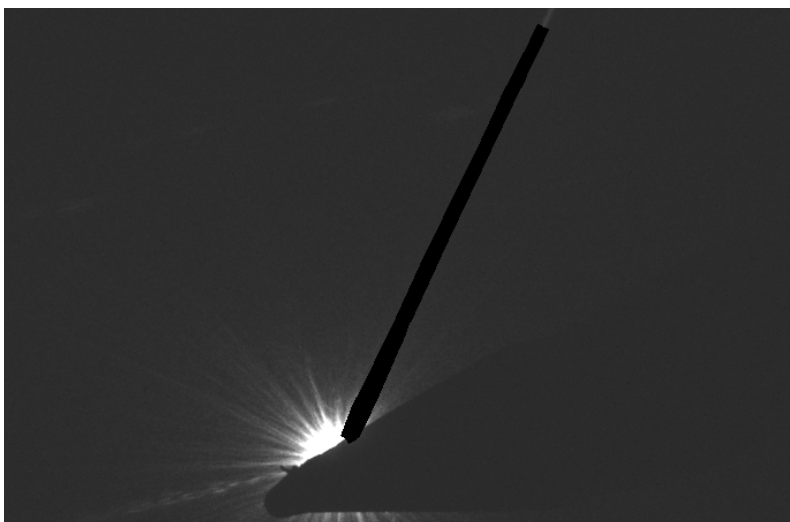


Figure 6.3: The image of figure 6.1 after the removal of the bright stripe using the snake algorithm.

The used parameters for learning are shown in table 6.1. Due to the negative sign of  $\omega_m$  a region of high intensity is delineated. Figure 6.3 shows that the shape of the stripe is found well.

In the following steps of the analysis, pixels, which are assigned to the bright stripe, are handled like pixels corrupted by the beamstopper and are therefore ignored.

#### 6.1.4 Detection of the beamstopper

The detection of the beamstopper works as described in section 4.3.2. The parameters of table 4.1 also yield satisfying results for this experimental diffraction pattern.

The initialization of the active contour and its shape after the learning process is shown in figure 6.4. The shape is not found perfectly but sufficiently well for the purpose.

#### 6.1.5 Normalization of the intensity

The intensity dependent on the distance to the center of the diffraction pattern can be approximated by the exponential function quite well as can be seen in figure 6.5. The curve contains no visible maxima since the intensity of the diffraction spots is too low.

The effect of the undiffracted electrons cannot be eliminated completely since the intensity is not radial-symmetrically distributed. Nevertheless the rough trend can

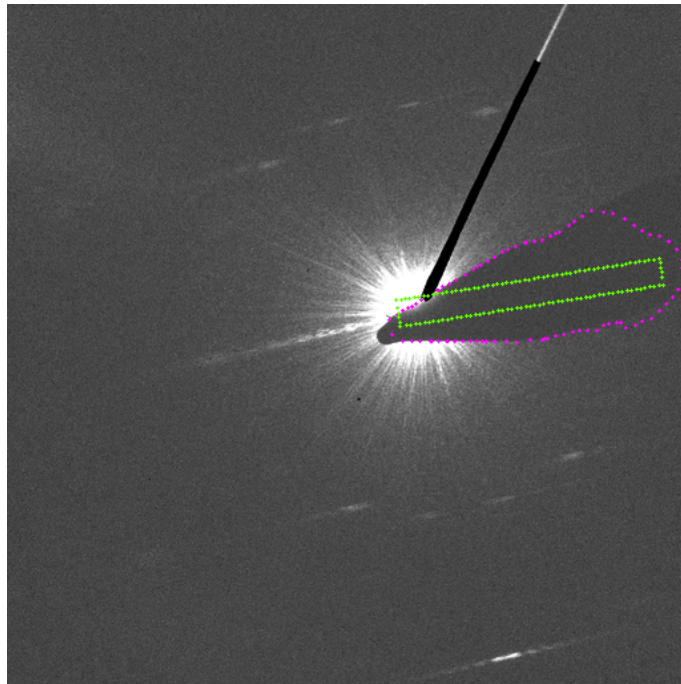


Figure 6.4: The light-green crosses mark the initialization of the active contour for the beamstopper detection. The pink crosses show the positions after learning. The intensity and the contrast of the image were increased manually otherwise the shape of the beamstopper would not be visible.

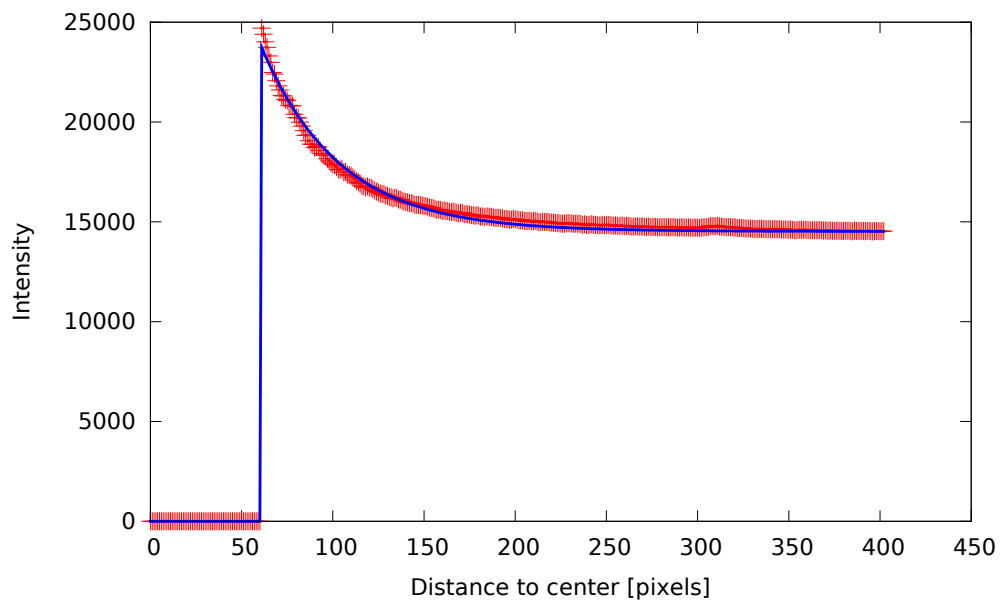


Figure 6.5: The red points show the intensity distribution depending on the distance to the center. The blue curve is the fitted exponential curve.

be removed.

### 6.1.6 Determination of the radius

The detection of the radius for this real image is harder than for the simulated image in chapter 4.

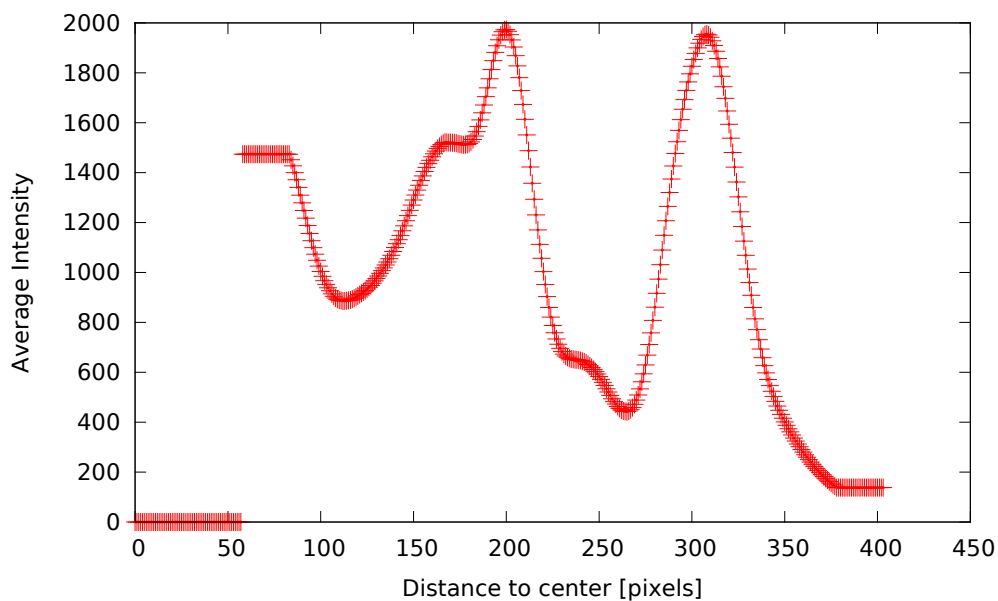


Figure 6.6: The radial intensity distribution measured as described in section 4.5.2: The maximum near 300 pixels does not have the highest intensity but the highest amplitude related to the lowest minimum with smaller distance to the center.

The curve in figure 6.6 shows the intensity depending on the distance to the center measured as described in section 4.5.2. The maximum, which is caused by the diffraction spots, is the one near 300 pixels. It is not the maximum with the highest intensity since the brightness of the spots is low and the noise level is high. However for the radius detection the value of interest is the height with respect to the lowest minimum with a smaller distance to the center. For the maximum near 200 pixels the lowest minimum with smaller distance to the center (zero values are ignored) is the one near 100 pixels. For the maximum near 300 pixels it is the one near 260 pixels. In the sense of this measurement the maximum near 300 pixels possesses a higher amplitude and therefore the radius is found correctly for this manual choice of the center.

### **Influence of the manual choice of the center**

However this curve changes even with small shifting of the center. The optimal center is located approximately at  $(x_c, y_c) = (621, 460)$ . To test the robustness of the algorithm, the automatic radius detection was applied for all integer values for  $x$  and  $y$ , which differ at most by  $\Delta c$  pixels from the optimal center, i.e.  $|(x, y) - (x_c, y_c)| \leq \Delta c$ . For  $\Delta c = 2.5$  pixels 21 possible starting points exist. For 20 initial conditions a radius was detected automatically, with which reasonable results were obtained.

In the following a result is defined as reasonable, if the distances of the located layer lines differ at most by 10 pixels from the distances obtained with the optimal center. This condition might also be checked easily by a non-experienced user, since the positions of the located layer lines are marked in the graphical user interface. The user just has to assure, that the positions match with the visible layer lines.

In cases when the automatic detection fails, the radius can still be determined by hand. Therefore in the one case that is not working for a maximum deviation of  $\Delta c = 2.5$  pixels a reasonable result was obtained when the radius was given by hand. No further manual intervention was necessary.

With larger deviation from the optimal center, the probability for a too imprecise determination of the radius increases. For a manually identified center, which differs at most by  $\Delta c = 5$  pixels from the optimal center, the algorithm works well in 55 cases out of the 81 cases tested. The manual radius determination fixed the problems in 12 cases.

The reason for the failure of the analysis in the cases when the radius was given by hand might be found in the normalization of the intensity and in the initialization of the snake algorithm for the beamstopper detection. These two preprocessing steps also depend on the position of the chosen center. If one of these preprocessing steps fails completely, the further analysis could be impossible.

#### **6.1.7 Correction of the center**

If the center of the image is identified by hand, the correction of the center is important, since one goal of the automation of the analysis is the enhancement of objectivity. Therefore the analysis should depend as little as possible on subjective decisions of the analyzing person. In this section the influence of the manual center choice on the center position after the correction of the center is described.

As well as in the section above various values for the rough determination of the center with a maximum deviation  $\Delta c$  of 2.5 and 5 pixels around the optimal center

are tested. Only cases are examined, which yield reasonable results in the end. The correction of the center depends on the radius of the circle through the diffraction spots (cf. section 4.5.3), therefore the correction only makes sense for appropriate values of the radius.

As reference to decide how much the obtained corrected centers differ, the median of the corrected centers is determined. The deviation from the median position is calculated in the direction parallel and perpendicular to the equatorial line. In the perpendicular direction the deviation for  $\Delta c = 5$  pixels is in  $52 \hat{=} 78\%$  of the cases, which yield a reasonable result, smaller than 1 pixel. For  $\Delta c = 2.5$  pixels even in all cases the deviation is below 1 pixel.

For the direction parallel to the equatorial line the deviation is smaller than 1 pixel in only 52% ( $\Delta c = 2.5$  pixels) respectively 39% ( $\Delta c = 5$  pixels) of the cases. This is not astonishing, since the correction of the center parallel to the tube axis works significantly more precisely than parallel to the equatorial line.

As it was shown here, the correction of the center reduces the impact of the manual choice of the center by the analyzing person significantly.

### 6.1.8 Determination of the layer line distances

The intensity dependent on the distance to the equatorial line measured near a circle is shown in figure 6.7.

In this curve it stands out, that the maximum near 265 pixels, which belongs to the second layer line, consists of two peaks. This splitting is not an artifact generated by the measurement near the circle since it is actually visible in the image, as can be seen in figure 6.8 on the left side.

One could assume, that two tubes with very similar chiral angle  $\alpha$  are observed and therefore there are two second layer lines. However the splitting of the line does not only occur on the second layer line but also on the equatorial line, as can be seen in figure 6.8 on the right side.

Christian Huber, who took the image, assumes in his thesis [16], that the tube is broken at the position where the image was taken and therefore the direction of the tube axis changes in the relevant area. Also the image taken in real space indicates that.

That means for the automatic analysis, that the determination of the distances of the second layer line to the equatorial line contains a large error, since in one quadrant the nearer and in another quadrant the farther maximum may be detected. Table 6.2 shows the distances, the corresponding errors and the obtained ratio  $r_{meas}$  with

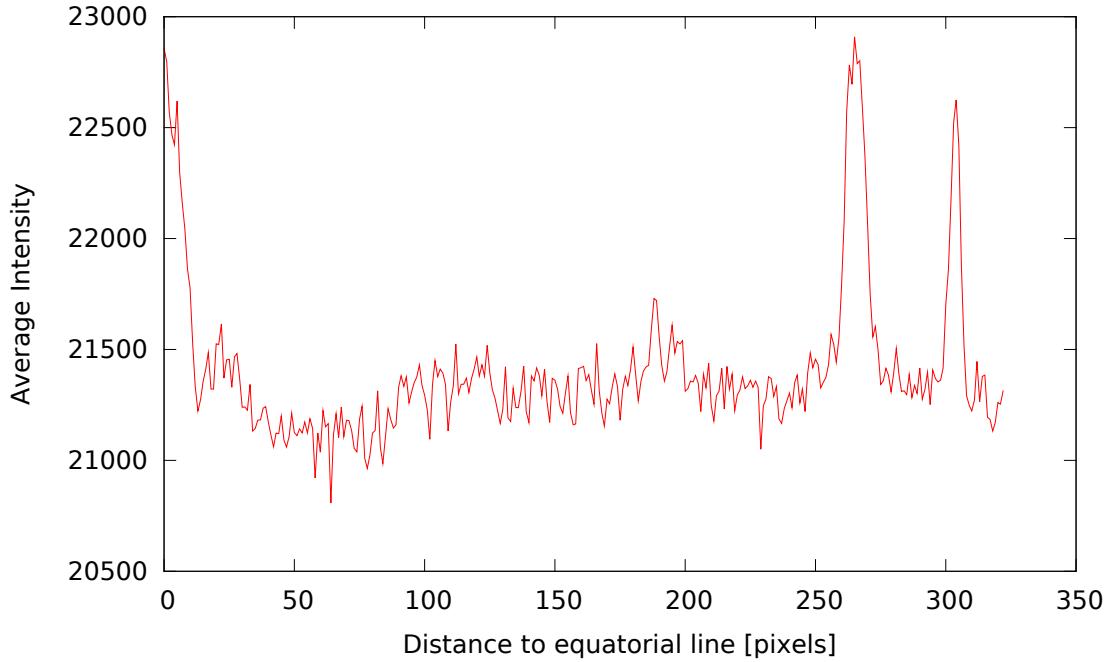


Figure 6.7: Intensity dependent on the distance to the equatorial line measured near a circle: The maximum near 265 pixels consists of two peaks.

its error.

$D_1$	$\Delta D_1$	$D_2$	$\Delta D_2$	$D_3$	$\Delta D_3$	$r_{meas}$	$\Delta r$
304.70	0.58	266.46	2.31	n.a.	n.a.	0.666	0.014

Table 6.2: Distances of the layer lines to the equatorial line with their errors and the measured ratio  $r_{meas} = m/n$  and its error.

The third layer line should be located near 38 pixels, however it is not observable in the curve in figure 6.7.

Since the error  $\Delta r$  is quite large, the number of possible candidates is high. These candidates are further analyzed in the following.

### 6.1.9 Center correction using the layer lines

The correction of the center with the use of the intensity distributions on the layer lines in the individual quadrants (cf. section 4.7.1) further increases the independence of the choice of the manual center.

Since the correction only has an effect on the direction parallel to the equatorial line, just that direction is taken into account here. For  $\Delta c = 5$  pixels now 66 %

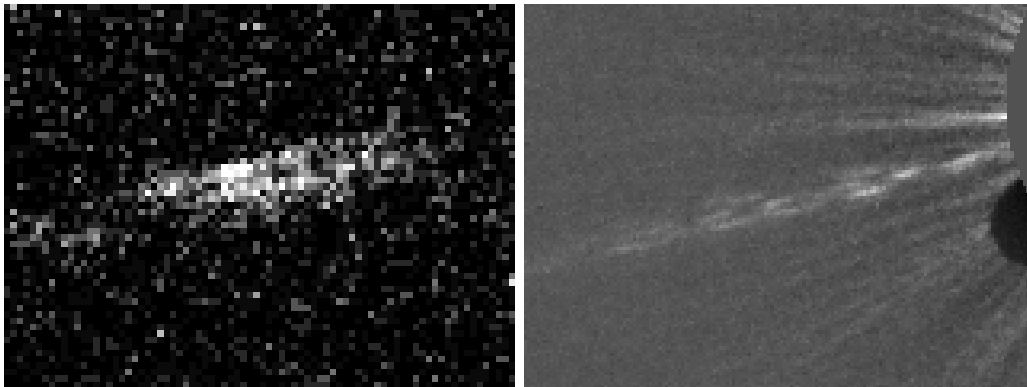


Figure 6.8: An enlarged detail around the second layer line in the third quadrant of the preprocessed image with enhanced contrast and brightness is shown on the left. It looks like two separate layer lines. The right side shows an enlarged part of the equatorial line, the brightness and the contrast were not enhanced. The equatorial line seems to consist even of three lines.

differ from the median at most by 1 pixel. For  $\Delta c = 2.5$  pixels even 91 % fulfill this condition.

This shows, that after the corrections the located center is mostly independent of the manual choice of the center, as far as it is a good approximation of the real center. This enhances the objectivity of the analysis.

### 6.1.10 Determination of the maxima positions on the layer lines

The following steps of the analysis are presented using the best manual choice of the center (621, 460) and its automatic corrections. The large number of candidates should now be decreased by the comparison between simulated layer lines and the measured ones. Figure 6.9 shows the averaged intensity distribution and the intensity distribution in each quadrant dependent on the distance to the tube axis measured on the first layer line.

The first maximum  $k_1$  is the highest peak in all quadrants and clearly visible. The second maximum  $p_1$ , which is located approximately at 110 pixels, is not observable in the third quadrant. In the other three quadrants and in the averaged curve it is clearly visible. Because of the third quadrant there is a large error in the measurement of the distance between the first and second maximum.

In the intensity distribution on the second layer line similar behavior appears (cf. figure 6.10).

Also here the first maximum  $k_2$  is the highest peak in the averaged curve and easily

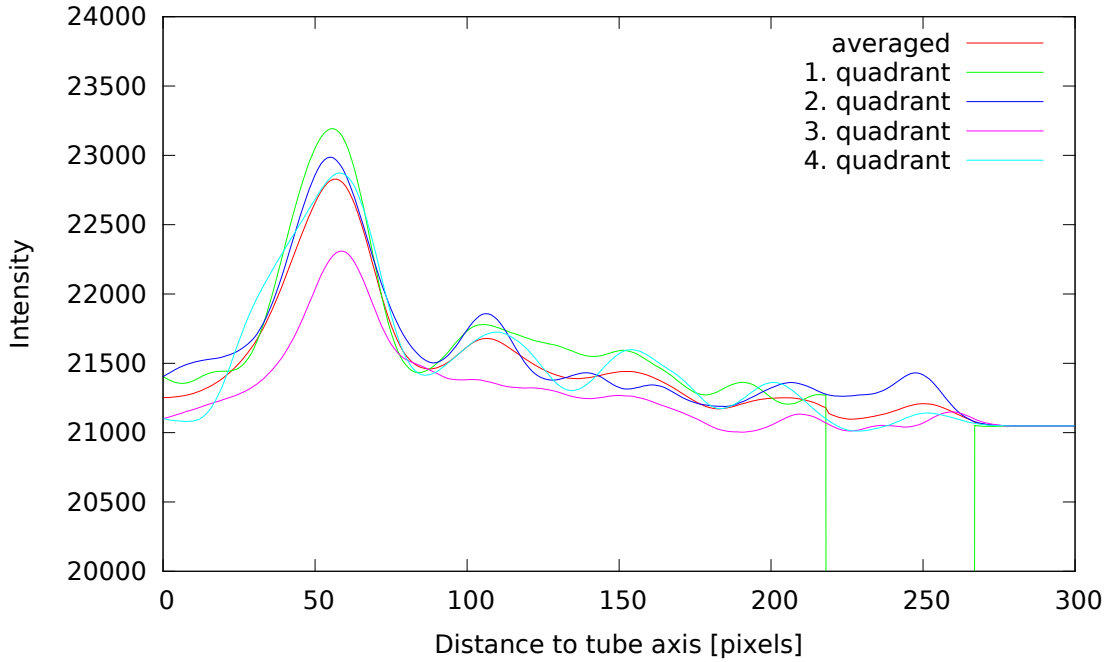


Figure 6.9: Intensity distribution dependent on the distance to the tube axis on the first layer line in the quadrants: The first maxima all match well, the second maximum is not visible in the third quadrant.

identifiable in all quadrants. However in the third quadrant no maximum is located at the position, where the maximum appears in the second and forth quadrant (near 220 pixels). The first quadrant yields no information at this point, since in the area of the image, where the second maximum should appear, the bright stripe is located and hence the pixels there are marked as corrupted. Therefore in the measurement of the distance between the first and the second maximum  $p_2$  on the second layer line a large error is obtained.

The disruption of the tube could be the reason for the deformed curve of the layer lines in the third quadrant. This defect might cause additional interferences in the diffraction pattern.

Table 6.3 shows the measured values and their errors.

$k_1$	$\Delta k_1$	$p_1$	$\Delta p_1$	$k_2$	$\Delta k_2$	$p_2$	$\Delta p_2$
56.6	2.0	49.9	7.3	169.6	2.9	42.9	5.6

Table 6.3: Measured distances to the tube axis and their errors for the experimental single-walled pattern.

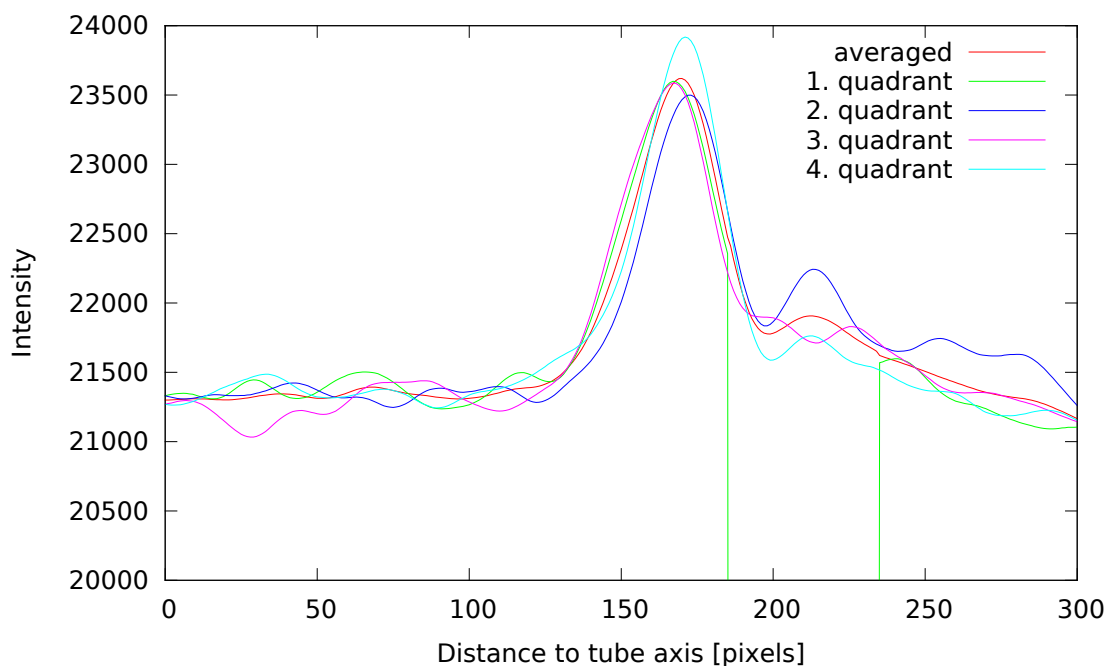


Figure 6.10: Intensity distribution dependent on the distance to the tube axis on the second layer line in the quadrants: Again the first maxima all match well, but the position of the second maximum in the third quadrant differs. The zero values in the first quadrant are caused by pixels, which are corrupted by the bright stripe.

### 6.1.11 Comparison between measurement and simulation

Since the errors in each individual measurement are large, the number of tubes, which reach a similar and high score, is high. Table 6.4 shows the candidates, which reach the highest scores for the manual set center (621, 460).

First of all it is noticeable, that the three candidates with the highest score all possess identical score  $S_r$  for the ratio of the chiral indices. These candidates have the same ratio  $m/n = 2/3$ , which also means, that they possess the same chiral angle  $\alpha$ . In contrast the analysis of the intensity distributions on the layer lines takes more care of the diameter of the candidates. Here the table shows, that the first layer line points to larger tubes than the second layer line, since the candidates with a larger diameter reach higher scores for the first layer line. The tube, which reaches high values for both layer lines, is the (33, 22) tube. Overall it therefore reaches the highest score, which can be seen as a reasonable result.

For the (33, 22) tube the angle between the electron beam and the tube axis tube is estimated to be  $\gamma = 67.8^\circ \pm 1.1^\circ$  using the first layer line and  $\gamma = 66.6^\circ \pm 0.2^\circ$  using the second layer line. This quite precise determination of the angle is an effect of the

Candidate	$S_l^1$	$S_l^2$	$S_l^3$	$S_r$	$S$
(33, 22)	0.9566	0.9651	n.a.	0.9992	0.9600
(36, 24)	0.9957	0.8949	n.a.	0.9992	0.9432
(30, 20)	0.8655	0.9998	n.a.	0.9992	0.9294
(35, 23)	0.9882	0.9198	n.a.	0.9564	0.9118
(32, 21)	0.9351	0.9828	n.a.	0.9469	0.9077
(39, 26)	0.9963	0.8006	n.a.	0.9992	0.8924
(34, 23)	0.9709	0.9446	n.a.	0.9265	0.8872
(38, 25)	0.9995	0.8330	n.a.	0.9638	0.8794
(37, 25)	0.9990	0.8632	n.a.	0.9364	0.8696
(31, 21)	0.8987	0.9953	n.a.	0.9138	0.8642
(29, 19)	0.8253	0.9968	n.a.	0.9343	0.8473
(42, 28)	0.9724	0.7103	n.a.	0.9992	0.8304
⋮	⋮	⋮	⋮	⋮	⋮

Table 6.4: Candidates and their scores for the experimental image in figure 6.1.

large deviation from perpendicular incidence. In this area the diffraction pattern varies strongly with a change of the angle  $\gamma$ .

The (33, 22) tube possesses a diameter of 3.75 nm. Christian Huber suggests in his thesis a diameter of 3.28 nm measured in real space. Professor Zweck estimates the uncertainty in the determination to be 20%. This yields a possible range for the diameter of [2.62, 3.94] nm. The (33, 22) tube therefore is in the range of allowed diameters.

In the estimation of the ratio  $m/n$  a small discrepancy between the manual and the automatic analysis appears. The manual by Christian Huber determined ratio is  $0.656 \pm 0.01$ . The automatically obtained result is  $0.666 \pm 0.014$ . With respect to the error limits, these values match well.

Overall the manual and the automatic analysis yield very similar results. A final conclusion, which analysis determined the tube more precisely, cannot be done. However a large advantage of the automatic analysis is its objectivity.

### **Influence of the manual choice of the center**

The manual choice of the center effects the final result as follows. In the 21 possibilities for the center, which differ at most by 2.5 pixels from the optimal center ( $\Delta c = 2.5$  pixels), the (33, 22) reaches the highest score 20 times. This as well suggests, that the (33, 22) tube is indeed the right choice.

With a maximum deviation  $\Delta c = 5$  pixels the final result is not that clear. Now in 67 out of 81 cases the positions of the layer lines are detected tolerably exact. For

these 67 cases the (33, 22) tube reaches the highest score  $44 \hat{=} 66\%$  times.

This shows, that the algorithm can deal with small variations of the manual determination of the center. Even for many not optimal starting points reasonable and similar results are obtained. The dependence on the analyzing person is therefore significantly reduced and the objectivity is increased.

Except for the manual detection of the center the analysis is done completely autonomously. Deeper knowledge of the analyzing person about the theory of electron diffraction from carbon nanotubes is therefore not necessary.

## 6.2 Analysis of multi-walled tube respectively bundle of tubes

The diffraction pattern (cf. figure 6.11) presented in this section was kindly provided by Elsa Thune.

The diffraction spots in this image possess high intensity, so it is observable by the naked eye, that it has to be a multi-walled tube or a bundle of tubes. Even the second ring of diffraction spots is visible, but it is not used for the analysis.

The image was taken analogously and afterwards digitalized with a scanner. The size amounts to  $1493 \times 1558$  pixels. It is a gray-scale image with a color-depth of 16 bits, in which only 12 bits are used.

There is no available image in real space for this pattern, therefore it cannot be used to decide, whether it is a bundle of tubes or a multi-walled tube. An analysis of this pattern with another technique than the one presented here is not known.

### 6.2.1 Noise Reduction

Like the other experimental image presented before this image contains noise, which should be reduced. However the noise in this image is of a slightly different kind. It consists not of single pixels which are corrupted, but of small areas of several pixels, which are disturbed. The reason for this is, that the image was taken analogously.

The noise reduction described in section 6.1.1 also works in this case as can be seen in figure 6.12. Many of the too bright patches in the original image (left side) disappear after the processing (right side). Even though not all defects are found, a significant improvement is reached.



Figure 6.11: Diffraction pattern of a multi-walled tube or a bundle of tubes kindly provided by Elsa Thune. The diffraction spots possess high intensity.

### 6.2.2 Rough determination of the center

The rough determination of the center, as described in section 4.2, works well for this diffraction pattern, since the undiffracted electron beam is very distinctive in this case. Therefore the image contains a uniformly shaped circle, where the intensity reaches its saturation. This is the shape of the undiffracted electron beam which is optimal for the used algorithm.

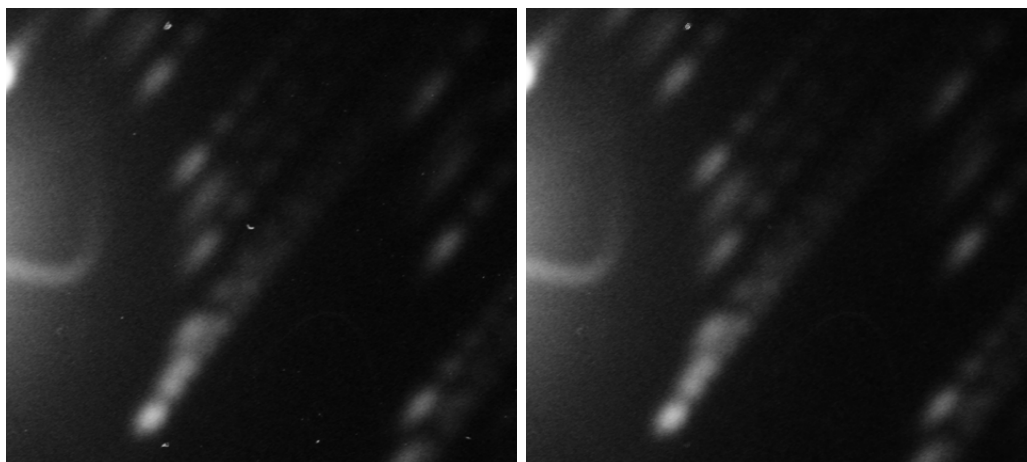


Figure 6.12: The left side shows an enlarged part of the image in figure 6.11. The right side shows the same part after the noise reduction. Many of the small bright areas disappear, but the diffraction spots are not affected.

### 6.2.3 Delineation of the beamstopper

The beamstopper in this image contains slightly different properties than the one that is used in the TEM of the University of Regensburg. Its width is not growing further in the area near the border and the contrast is higher.

Since the program should deal with both kinds of images, the parameters of the snake algorithm are kept constant for all images. This leads to an imperfect delineation of the beamstopper in this image, however the accuracy is still sufficient, since the identification in the important area works well (cf. figure 6.13).

The detection would work significantly better, if the set of parameters was adjusted. But this would also lead to an incorrect detection of the beamstopper of the image taken in Regensburg. The parameters used here represent a compromise, so that all kinds of images are treated sufficiently well.

If a large number of similar images is available, it will be advisable to adjust the parameters for these images. This could be done without any change of the source code of the program, since the parameters are stored in a configuration file, which can be edited without any knowledge of programming.

### 6.2.4 Normalization of the intensity

Also in this image the undiffracted electron beam adds intensity to the image, which is dependent on the distance to the center. In the intensity distribution with respect to the distance to the center (cf. figure 6.14 red) two significant maxima appear,

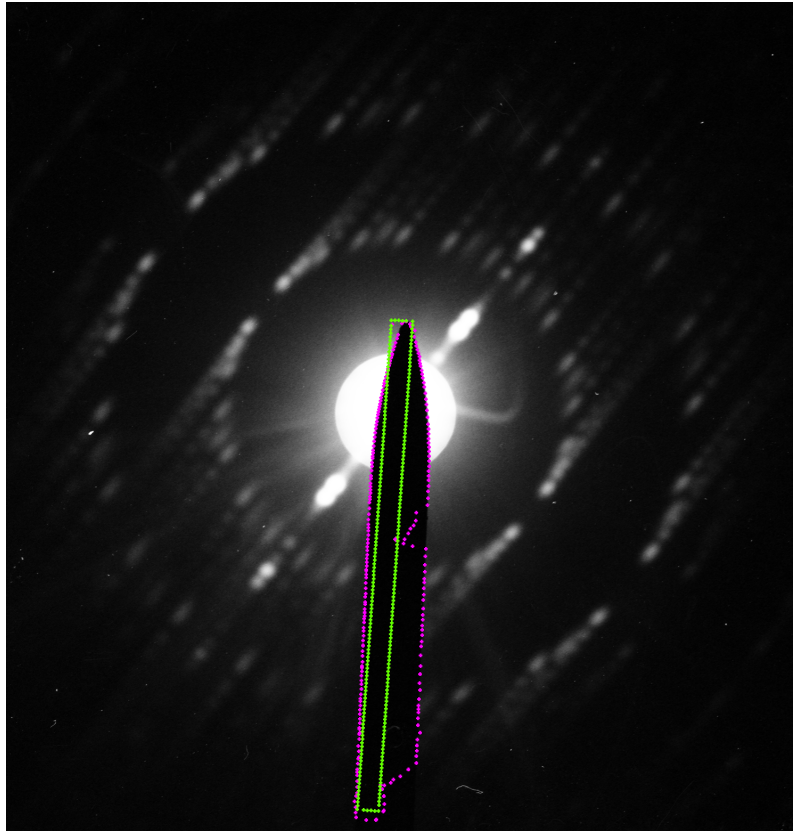


Figure 6.13: The initialization for the snake algorithm is shown in green. The pink points mark the active contour after learning. The shape of the beamstopper is not determined exactly but sufficiently precise in the important area. The performance could be improved with a different set of parameters.

which are caused by the two visible rings in the image, where the diffraction spots are located. The strong appearance of these maxima is also a consequence of the high intensity of the diffraction spots.

If this distribution was subtracted from the image, two dark circles would appear similar to the simulated image in figure 4.6. By the approximation of the curve with an exponential function this effect is avoided (cf. section 4.4).

To reduce the influence of the maxima on the approximated curve, only points are used, whose intensity is smaller than the intensity of all points with smaller distance to the center. The used points are marked cyan in figure 6.14, the approximated exponential is the blue curve.

Figure 6.15 shows the image after the subtraction of the fitted curve. The intensity is independent of the distance to the center and the diffraction spots are not diminished above average.

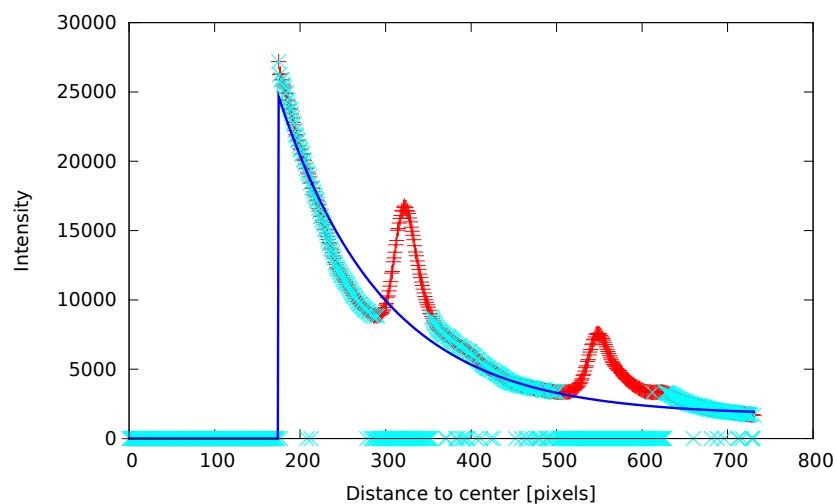


Figure 6.14: The red points show the intensity distribution measured in figure 6.11, cyan are the points used for the fit. The blue curve marks the fitted curve. The rings of the diffraction spots cause high maxima. These maxima are not used for the fit.

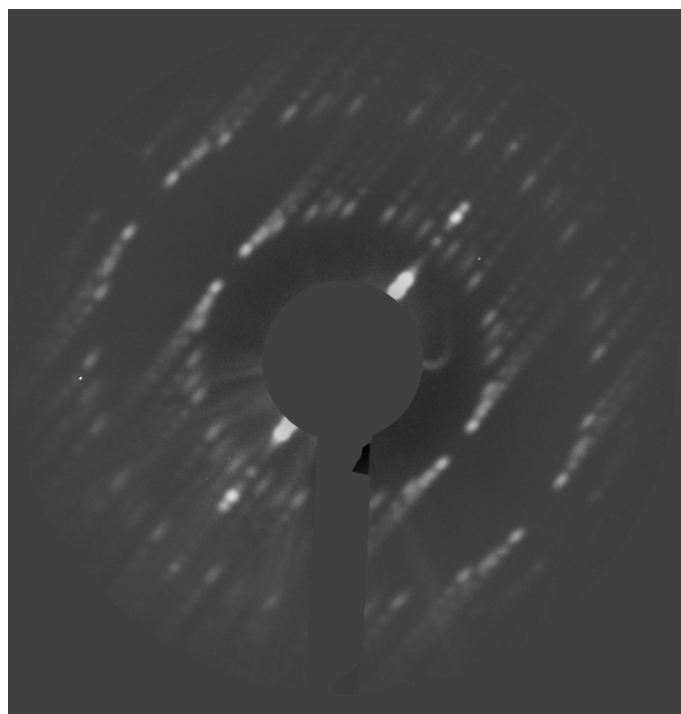


Figure 6.15: After the subtraction of the approximated exponential curve, the intensity is not dependent on the distance to the center. No black circle through the diffraction spots occurs.

### 6.2.5 Determination of the radius

The radius of the circle through the main diffraction spots can be well determined by the method described in section 4.5.2, since the main diffraction spots possess high intensity. They cause a high maximum in the intensity distribution depending on the distance to the center (cf. figure 6.16). The second highest maximum belongs to the second ring of diffraction spots.

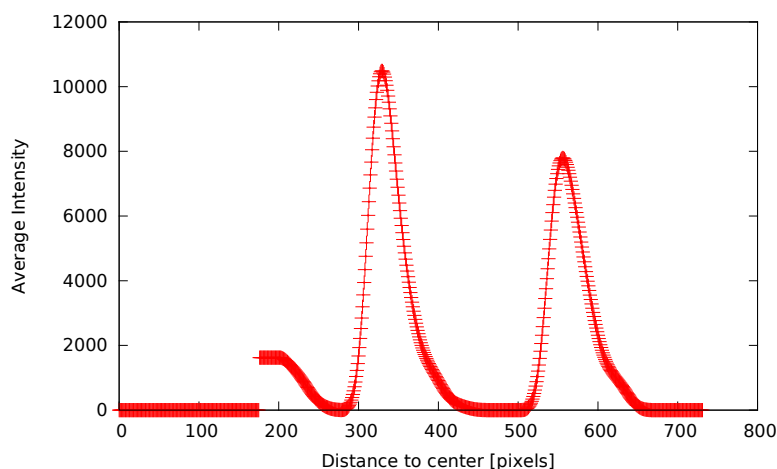


Figure 6.16: Intensity depending on the distance to the center measured as described in section 4.5.2. The main diffraction spots cause a high maximum near 330 pixels.

### 6.2.6 Correction of the center

Although in this image the rough detection of the center works very well, also here the correction of the center is very important. This is caused by the fact, that the center of the undiffracted electron beam does not match the center of the diffraction pattern exactly.

This behavior is observable in figure 6.17. The blue and the pink circle have the same center, which is marked cyan. The blue circle follows the shape of the undiffracted electron beam very well, whereas the pink circle does not match the first diffraction spots perfectly. In the bottom left corner the spots are matched well, but in the top right corner the spots are only touched. This means, that this center of the circle through the diffraction spots is not the perfect one, although it is the center of the undiffracted electron beam.

Since the correction of the center, which was described in section 4.5.3, uses the diffraction spots for the correction, it is able to compensate this. Without the correction the intensity distribution measured near the circle in the quadrants looks

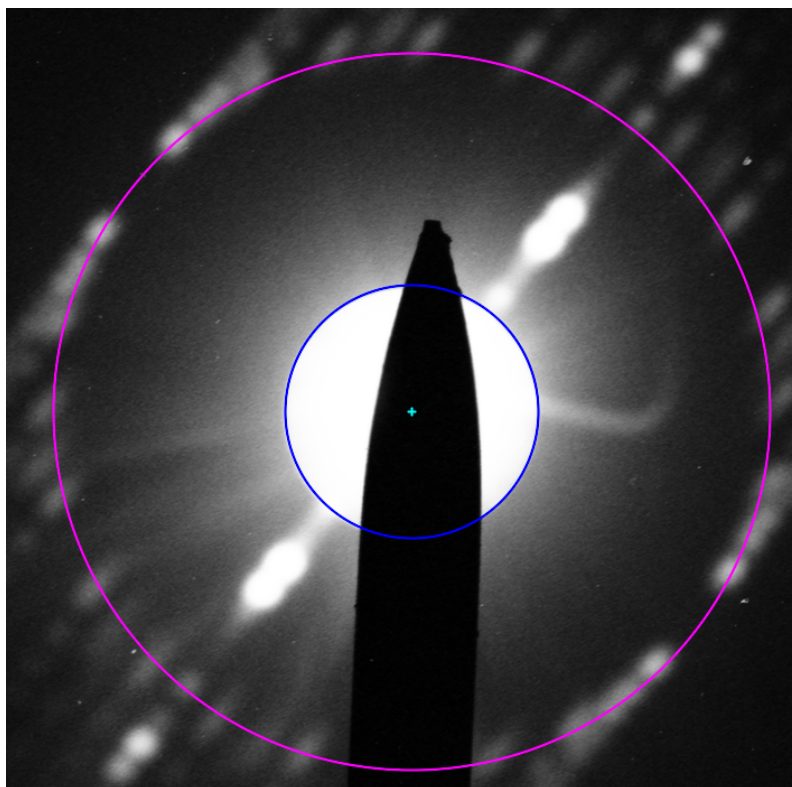


Figure 6.17: The blue and the pink circle have the same center, which is marked cyan. The blue circle follows the shape of the undiffracted electron beam very well, whereas the pink circle does not match the first diffraction spots perfectly. Especially in the bottom left and top right corner the spots are crossed differently.

like shown in figure 6.18. The positions of the diffraction spots, which cause maxima in this distribution, differ significantly in the various quadrants. This of course has a negative influence on the averaged intensity distribution.

The intensity distribution measured in the quadrants after the correction of the center is shown in figure 6.19. The curves of the individual quadrants match much better.

The correction moves the center by 9.5 pixels. This shows, that the correction of the center is very important for this image.

### 6.2.7 Determination of the layer line distances

Like the example in section 5.1 the image possesses very broad layer lines. Therefore also here the first layer lines overlap in the direction perpendicular to the equatorial line.

The red curve in figure 6.20 shows the intensity distribution dependent on the dis-

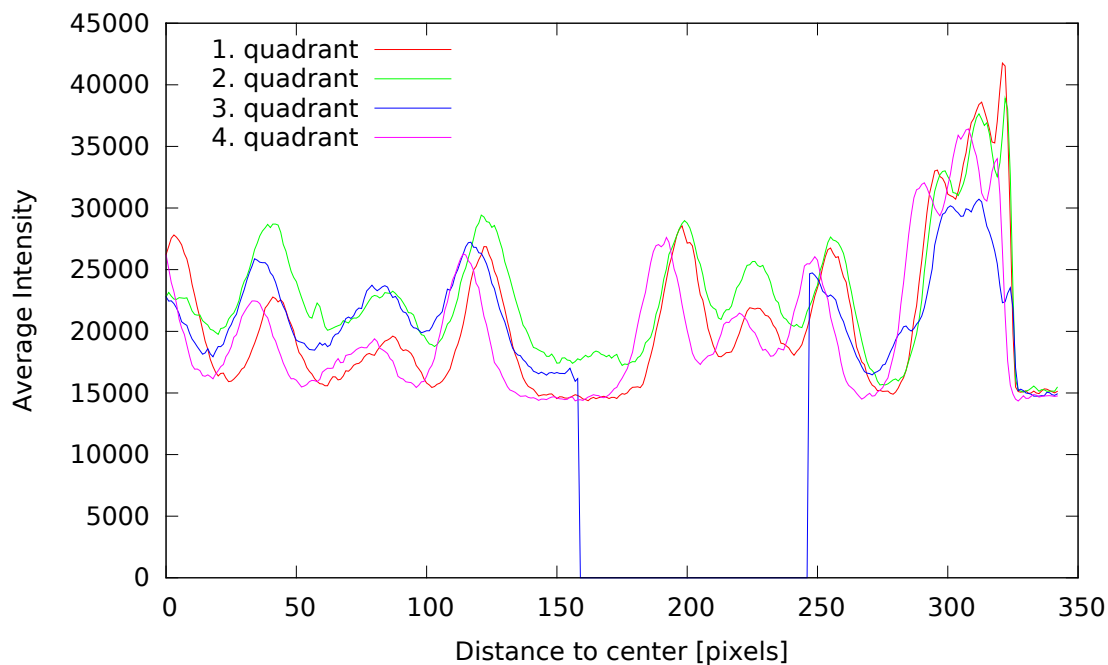


Figure 6.18: The intensity measured near a circle with the uncorrected center differs significantly in the quadrants.

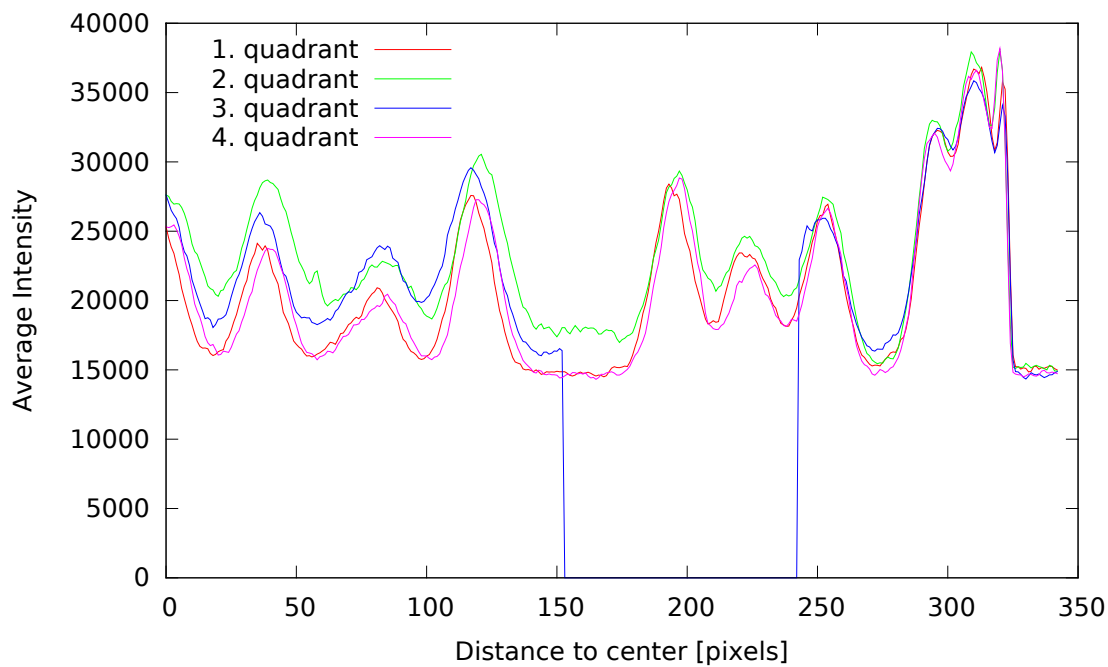


Figure 6.19: After the correction of the center and the angle the curves in the quadrants possess significantly higher correlation.

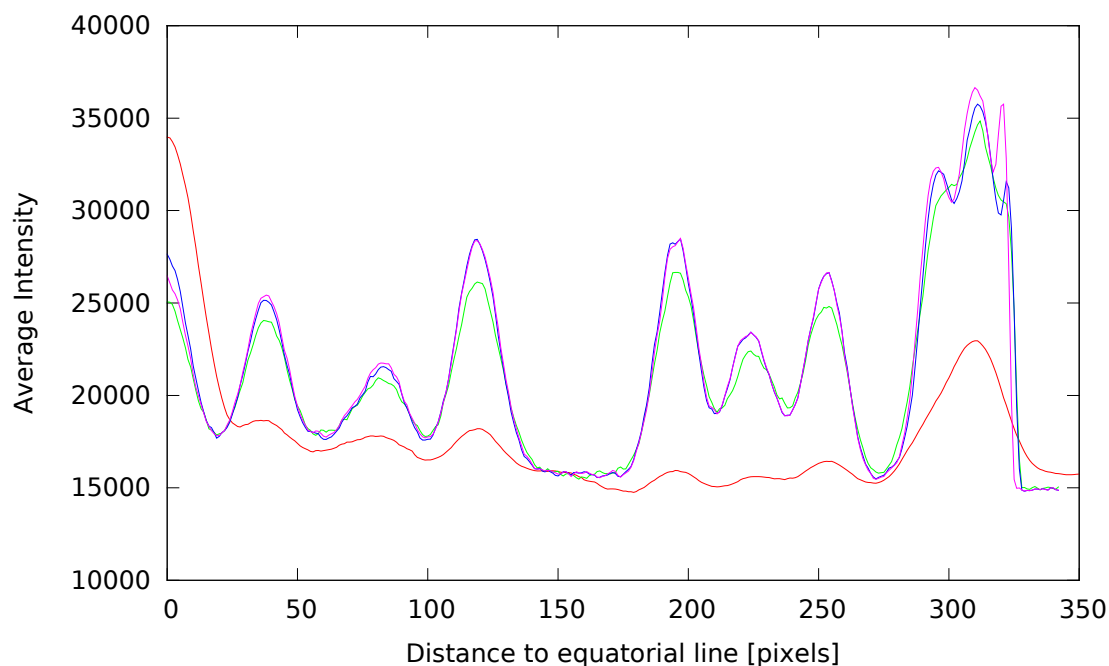


Figure 6.20: The intensity distribution depending on the distance to the equatorial line measured in four different ways: *Red*: All pixels of the image are used. The intensities of the maxima are low, near 300 pixels only one broad maximum can be observed. *Green*: The measurement took place near the circle around the uncorrected center. The maxima are higher, but still just one maximum appears near 300 pixels, where the first layer lines are located. *Blue*: In the measurement near the circle around the corrected center the layer lines can be distinguished. *Pink*: In the measurement near the ellipse the maxima corresponding to the first layer lines can be distinguished well, especially the one with the largest distance to the equatorial line.

tance to the equatorial line measured with the use of all pixels of the image. Here the layer lines cause only small maxima. Near 300 pixels only one broad maximum appears. The fact, that there are three different layer lines in this area, cannot be observed.

The green curve shows the measurement near the circle, but without the correction of the center and the angle. The layer lines generate significantly higher maxima, however the layer lines near 300 pixels still cannot be distinguished.

The blue curve shows the measurement near the circle after the correction of the center. Here near 300 pixels three maxima are observable, therefore the layer lines could be resolved. However the maximum with the largest distance to the equatorial line is still less distinctive.

This is improved by the measurement near the ellipse, which the pink curve shows.

The maximum is clearly distinguishable there and can be recognized by the algorithm easily. Overall nine maxima, which correspond to the layer lines, can be identified. All of them are detected by the algorithm and can be assigned to three nanotubes.

Not only the measurement near the ellipse is important for the correct analysis, but also the improvement of the accuracy in the determination of the distances of the layer lines by the measurement in a rectangle as described in section 4.5.6 is important. For the layer line with the largest distance to the equatorial line the correction amounts to six pixels. This deviation would falsify the ratio  $m/n$  significantly.

Table 6.5 shows the distances of the layer lines of the three tubes with their errors and the corresponding ratios  $m/n = r_{meas}$  with their errors.

Tube	$D_1$	$\Delta D_1$	$D_2$	$\Delta D_2$	$D_3$	$\Delta D_3$	$r_{meas}$	$\Delta r$
1	313.57	1.53	195.70	2.61	118.91	1.96	0.1804	0.0113
2	308.53	1.24	225.17	2.25	83.32	2.00	0.3618	0.0121
3	294.59	1.97	253.05	1.92	37.90	2.06	0.6293	0.0188

Table 6.5: Distances to the equatorial line of the layer lines with their errors and the measured ratios  $r_{meas} = m/n$  and their errors.

Due to the very broad layer lines relatively large errors in the determination of the distances to the equatorial line occur. This also leads to large errors in the ratio  $r_{meas}$ .

Further should be mentioned, that the first layer lines of the first two tubes only possess a distance of five pixels to each other and are additionally very broad. Nevertheless they can be distinguished due to the measurement near the ellipse.

### 6.2.8 Analysis of the layer lines

The analysis of the intensity distributions on the layer lines raises problems in this case. Due to the small distance between the layer lines in combination with their large width they overlap. The first layer lines of each of the three tubes is shown in figure 6.21.

Especially the first layer lines of the first (red) and the second (green) tube possess high correlation. This is a strong indication for the overlap of the lines. But also the line of the third tube (blue) is disturbed, as can be seen in the flat slope of the first maximum. The slope would be steeper there for non-overlapping lines.

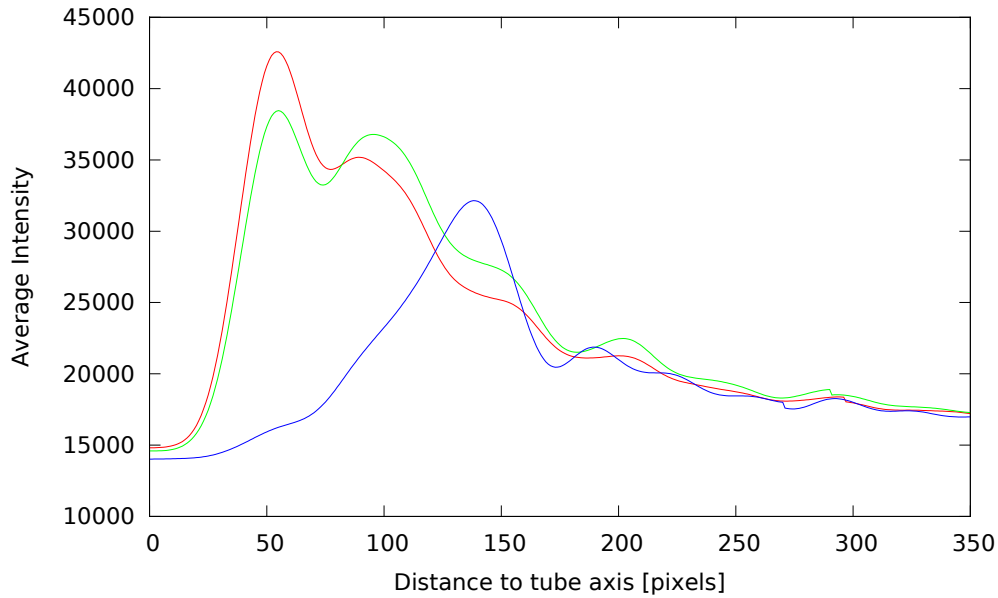


Figure 6.21: The intensity distribution on the first layer lines of the first (red), second (green) and third (blue) tube depending on the distance to the tube axis: Especially the ones of the first and second tube possess high correlation, which is an indication for the overlap. Also the line of the third tube is disturbed, whereupon the flat slope of the first maximum is an indication.

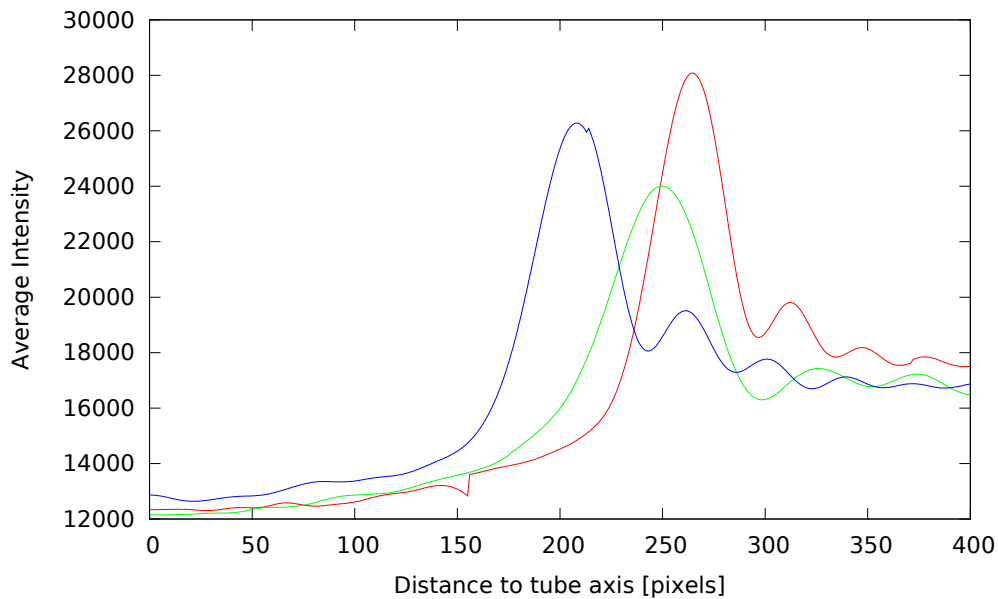


Figure 6.22: The intensity distribution on the second layer lines of the first (red), second (green) and third (blue) tube depending on the distance to the tube axis: All are of very nice shape, even the third maxima are observable.

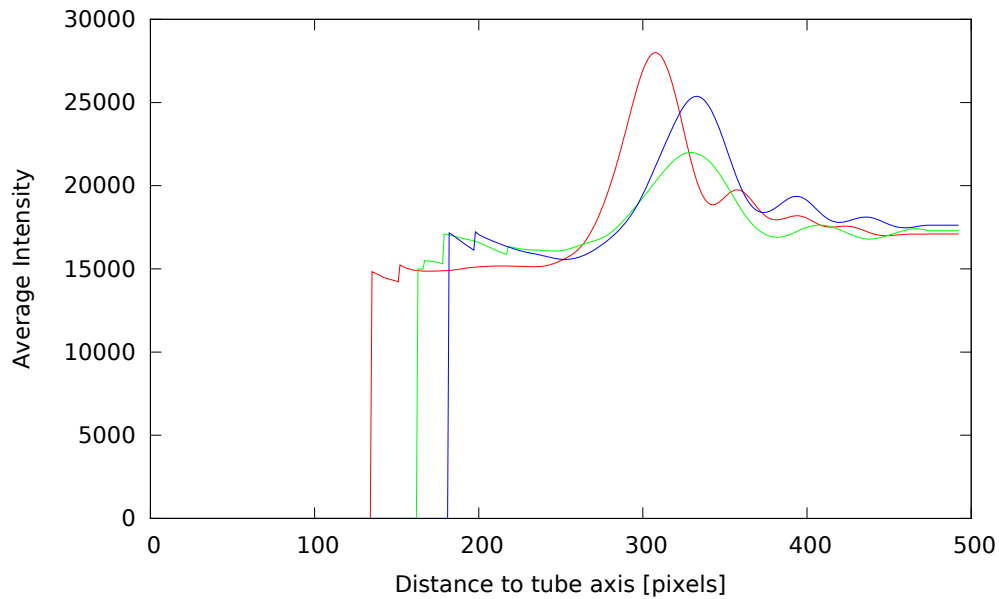


Figure 6.23: The intensity distribution on the third layer lines of the first (red), second (green) and third (blue) tube depending on the distance to the tube axis: All are of very nice shape, even the third maxima are slightly observable. The zero-values near the tube axis are caused by the beamstopper.

The second (cf. figure 6.22) respectively third (cf. figure 6.23) layer lines possess the typical shape, which is similar to Bessel functions. They are of high quality, which means that the second maximum is very clearly observable. Almost everywhere even further maxima can be identified, but these are not used for the analysis.

Due to their nice shape, these lines are suitable for the analysis. But by default only the first two layer lines of each tube are used for the analysis. However the user has the possibility to select in the graphical user interface, which layer lines should be used. In this case the second and third layer lines of each tube were selected as they possess high quality and are not overlapping.

The tables 6.6, 6.7 and 6.8 show the candidates for the three tubes with their scores. It should be noted, that the score for the first layer line does not contribute to the calculation of the overall score.

In the case of the first tube (cf. table 6.6), the (33, 6) tube reaches a very high score of 0.9977, especially since the highest possible score is 1. This means, that in all relevant measurements a high accordance with the simulation is reached. The score of the (34, 6) is high as well, but in all relevant parts the (33, 6) tube is superior, therefore one can assume, that it really is the tube of choice.

It should further be mentioned that the score of the first layer line is vanishingly

Candidate	$S_l^1$	$S_l^2$	$S_l^3$	$S_r$	$S$
(33, 6)	0.0000	0.9992	1.0000	0.9980	0.9977
(34, 6)	0.0025	0.9676	0.9444	0.9850	0.9689
(32, 6)	0.0158	0.9634	0.9264	0.9520	0.9344
(35, 6)	0.7132	0.8941	0.8091	0.9244	0.8740
(31, 6)	0.6363	0.8422	0.7416	0.8448	0.7753
(36, 6)	0.2288	0.8263	0.6497	0.8317	0.7561
(37, 7)	0.1012	0.6630	0.4045	0.9274	0.7552
(36, 7)	0.8981	0.8012	0.5656	0.8249	0.7384
(38, 7)	0.6198	0.5321	0.2530	0.9859	0.7192
⋮	⋮	⋮	⋮	⋮	⋮

Table 6.6: Candidates and their scores for the first tube.

low. Therefore a sensible result is only possible if this layer line is ignored.

Candidate	$S_l^1$	$S_l^2$	$S_l^3$	$S_r$	$S$
(16, 6)	0.0000	0.8987	0.9869	0.8634	0.8185
(17, 6)	0.0024	0.4797	0.9937	0.9343	0.6471
(14, 5)	0.0000	0.2948	0.5601	0.9811	0.5327
(15, 5)	0.0000	0.6139	0.7767	0.4997	0.3915
(18, 7)	0.0028	0.2727	0.8353	0.5369	0.2804
(18, 6)	0.0001	0.2838	0.9316	0.4997	0.2662
(19, 7)	0.0499	0.0206	0.7361	0.9641	0.1383
(13, 5)	0.0000	0.0124	0.3329	0.6436	0.0717
⋮	⋮	⋮	⋮	⋮	⋮

Table 6.7: Candidates and their scores for the second tube.

The score of the candidates of the second tube (cf. table 6.7) is not that high. However in this case the gap between the scores of the first and the second tube is higher. The reason for the relatively low scores is the small error in the determination of the maxima of the second layer line. In all quadrants the values are almost identical, so the error in the determination of the distance between the first and second maximum is  $\Delta p_i = 2$ , which is quite small. Therefore even small deviations from the simulation are punished hard on this layer line.

For this tube the probability is high, that it is indeed a (16, 6) tube. However the (17, 6) cannot be omitted completely since it might be possible that the precision of the measurement on the second layer line is overestimated and the score for the third layer line and the ratio is slightly larger. The other tubes are improbable, because they possess lower scores in both layer lines.

Also here it is very important to ignore the first layer line, since it yields senseless

results due to the overlap.

Candidate	$S_l^1$	$S_l^2$	$S_l^3$	$S_r$	$S$
(21, 13)	0.5484	0.9925	0.8960	0.9639	0.9603
(19, 12)	0.9997	0.8483	0.7605	0.9981	0.9193
(22, 14)	0.0996	0.8147	0.5451	0.9824	0.8867
(20, 13)	0.4066	0.9899	0.9838	0.8594	0.8551
(23, 14)	0.1333	0.7828	0.3366	0.8617	0.7623
(24, 15)	0.0115	0.4999	0.1220	0.9936	0.7026
(20, 12)	0.9639	0.8937	0.9617	0.7397	0.6993
(17, 11)	0.5597	0.4577	0.1498	0.8944	0.6051
⋮	⋮	⋮	⋮	⋮	⋮

Table 6.8: Candidates and their scores for the third tube.

In the case of the third tube (cf. table 6.8) the (21, 13) reaches a high score. On both relevant layer lines a significantly higher score than for the (19, 12) tube is reached. The low score for the ratio may be caused by the broad layer lines. However this is already taken into account for the calculation of the score, since the error in this determination is large and therefore the deviation is not punished that hard.

The first layer line was ignored again. The high score of the second best candidate on this layer line should not be overestimated, since here an overlap with the other tubes occurs.

Looking at the estimated angles  $\gamma$  between the incoming electron beam and the tube axis for the tubes with the highest scores (cf. table 6.9), accordance in the error limits is observed. The large errors, compared to the image in the last section, are a consequence of the incidence angle, which only differs a little from perpendicular incidence. In this range a change in the angle leads only to small changes in the diffraction pattern. Therefore the estimation of the angle is more imprecise than for a large deviation from perpendicular incidence.

Tube	$\gamma$	$\Delta\gamma$	$s$	$\Delta s$
1	80.2°	4.4°	0.0944	0.0006
2	77.4°	9.8°	0.0932	0.0010
3	80.3°	4.1°	0.0935	0.0011

Table 6.9: The estimated incidence angles  $\gamma$  and the scales  $s$  for the three candidates with the highest scores.

Almost the whole process is done automatically in this image, the user just has to recognize that there is an overlap of the first layer lines and deselect them in a graphical user interface. For this no deeper understanding of electron diffraction

from carbon nanotubes is necessary for the analysis using the program. Overall the analysis of this image yields very satisfying results.



# Chapter 7

## Conclusions

In this PhD-thesis a method was developed, which offers the possibility to analyze electron diffraction patterns from carbon nanotubes automatically with a computer program to determine the chiral indices  $n$  and  $m$ . Diffraction patterns of single-walled nanotubes can be evaluated as well as images of multi-walled tubes or bundles of tubes. To be able to verify the results of the algorithm, a simulation program was written, which produces diffraction patterns, that are similar to real ones, i.e. they contain noise, a beamstopper and an undiffracted electron beam.

The analyzing algorithm was described with the help of such a simulated image. The center of the diffraction pattern is estimated with the use of the undiffracted electron beam. The snake algorithm proofed to be a useful tool to delineate the position of the beamstopper. This is necessary to recognize in the later analysis, which pixels are corrupted by it.

The intensity, which is added to the image by the undiffracted electron beam, depends on the distance to the center. This intensity distribution is approximated by an exponential function, to get a smooth curve. Afterwards the intensity, which has been estimated to be caused by undiffracted electrons, is subtracted from each pixel. It was shown, that the influence of the undiffracted electron beam is reduced without diminishing the diffraction spots.

The distances of the diffraction spots to the center are measured using the symmetry properties of the diffraction pattern. Near a circle with a radius, which corresponds to this distance, intensity distributions dependent on the distance to the equatorial line in the individual quadrants are measured. The correlation between the curves in the quadrants are used to improve the accuracy of the detection of the center and the angle of the equatorial line. Since the diffraction spots are not perfectly located on a circle, parameters for an ellipse were estimated.

From the measurement of the intensity distribution dependent on the distance to the equatorial line near an ellipse, the distances of the layer lines are obtained, since these cause maxima in that curve. From the number of these maxima and their distances to the equatorial line additionally the number of observed tubes is estimated. With the use of the distances of the layer lines the ratio of the chiral indices  $n$  and  $m$  and therefore the helical angle  $\alpha$  is calculated.

Thereby a set of possible tubes, which possess a similar ratio of the chiral indices, is obtained. These possible tubes, called candidates, are compared to simulations of diffraction patterns. For that the angle between the incoming electron beam and the tube axis  $\gamma$  and the scale of the image has to be known. It was shown that it is possible to estimate these parameters using the positions of the main diffraction spots on the layer lines. With the knowledge of these parameters the intensity distributions on the layer lines are compared to simulated curves. Thereby the positions of the second maxima on the layer lines are evaluated.

For an easy comparison of the match between the measurement and the theory of the individual candidates, scores for the various parameters are assigned. Hereby a deviation in a measurement, which could be performed precisely, leads to a stronger deduction of the score than for an estimation of high uncertainty.

To test the abilities of the algorithm, it was applied to various simulated images. Hereby it was shown that the algorithm yields the right chiral indices, even though the layer lines are that broad, that they slightly overlap. Applied to an image of very low signal to noise ratio, the correct result was obtained as well. Also the analysis of the diffraction pattern of a “zigzag” tube functions well. Only the image of an “armchair” tube could not be evaluated, since here the layer lines, which are necessary for the analysis, overlap. In the case of a simulated image of a bundle of five tubes the chiral indices of all tubes were estimated correctly by the algorithm. For images of very high quality there is no theoretical limit for the number of tubes, as long as the layer lines do not overlap.

The experimental diffraction pattern of a single-walled carbon nanotube, which was taken at the University of Regensburg by Christian Huber, was also analyzed by hand. In the analysis accordance between the manual and the automatic analysis was obtained in all measurements respecting the error limits. Estimating, which result is most possibly the right one, small deviations occurred. The reason might be a disruption of the tube, which is observable in the image in real space, because it influences the quality of the diffraction pattern. In any case the automatic analysis possesses the big advantage of being objective.

In the case of this image, the center could not be determined by the algorithm.

However it is possible, to estimate the center by hand. It was shown, that small deviations from the optimal center can be compensated by the automatic correction of the center. Therefore in most of the cases for manually chosen centers the same final result was obtained.

The analysis of an experimental diffraction pattern of a bundle of tubes or a multi-walled tube showed that the measurement near the ellipse allows the distinction of layer lines, which overlap to some extent. For this image, the number of possible chiral indices for all of the three tubes is very low. The analysis is performed completely autonomously, except that the user has to deselect the first layer lines for the analysis, since they overlap. For this no deeper understanding of electron diffraction from carbon nanotubes is necessary.

Overall the algorithm yields satisfying results for the analysis of the experimental patterns. The graphical user interface makes the usage easy and improves the traceability of the individual steps.

For the testing of the algorithm only a few experimental images were available, which differ strongly in their properties. Therefore the parameters of the program were chosen so that for all images reasonable, even though in some cases imperfect, results were obtained. If many images were available, which possess similar properties, it would be advisable to optimize the parameters for these images. This can be done in a configuration file, therefore no knowledge about programming is needed.

All in all the program is a very useful tool to analyze electron diffraction patterns from carbon nanotubes. It provides the user with an objective and fast method to estimate the structural parameters of the observed tubes.



# Appendix A

## Table of carbon nanotubes

The following table contains the diameter  $d$  and the helical angle  $\alpha$  of all carbon nanotubes with  $n \leq 40$  sorted by their ratio  $m/n$ .

Table A.1: Ratio  $m/n$

$m/n$	$n$	$m$	$d$ [nm]	$\alpha$ [°]	$m/n$	$n$	$m$	$d$ [nm]	$\alpha$ [°]
0.0000	n	0	n.a.	0.000	0.0250	40	1	3.1720	1.225
0.0256	39	1	3.0938	1.256	0.0263	38	1	3.0155	1.289
0.0270	37	1	2.9372	1.323	0.0278	36	1	2.8589	1.359
0.0286	35	1	2.7806	1.397	0.0294	34	1	2.7023	1.438
0.0303	33	1	2.6241	1.481	0.0312	32	1	2.5458	1.526
0.0323	31	1	2.4675	1.575	0.0333	30	1	2.3892	1.626
0.0345	29	1	2.3110	1.682	0.0357	28	1	2.2327	1.741
0.0370	27	1	2.1544	1.804	0.0385	26	1	2.0762	1.872
0.0400	25	1	1.9979	1.945	0.0417	24	1	1.9197	2.024
0.0435	23	1	1.8414	2.111	0.0455	22	1	1.7631	2.204
0.0476	21	1	1.6849	2.307	0.0500	20	1	1.6067	2.419
0.0500	40	2	3.2133	2.419	0.0513	39	2	3.1351	2.479
0.0526	19	1	1.5284	2.543	0.0526	38	2	3.0569	2.543
0.0541	37	2	2.9787	2.610	0.0556	18	1	1.4502	2.680
0.0556	36	2	2.9004	2.680	0.0571	35	2	2.8222	2.755
0.0588	17	1	1.3720	2.833	0.0588	34	2	2.7440	2.833
0.0606	33	2	2.6658	2.916	0.0625	16	1	1.2938	3.004
0.0625	32	2	2.5876	3.004	0.0645	31	2	2.5094	3.098
0.0667	15	1	1.2156	3.198	0.0667	30	2	2.4312	3.198
0.0690	29	2	2.3530	3.304	0.0714	14	1	1.1374	3.418
0.0714	28	2	2.2749	3.418	0.0741	27	2	2.1967	3.540

$m/n$	$n$	$m$	$d$ [nm]	$\alpha$ [°]	$m/n$	$n$	$m$	$d$ [nm]	$\alpha$ [°]
0.0750	40	3	3.2560	3.582	0.0769	13	1	1.0593	3.670
0.0769	26	2	2.1186	3.670	0.0769	39	3	3.1778	3.670
0.0789	38	3	3.0997	3.763	0.0800	25	2	2.0404	3.811
0.0811	37	3	3.0216	3.861	0.0833	12	1	0.9811	3.963
0.0833	24	2	1.9623	3.963	0.0833	36	3	2.9434	3.963
0.0857	35	3	2.8653	4.071	0.0870	23	2	1.8842	4.128
0.0882	34	3	2.7872	4.186	0.0909	11	1	0.9030	4.307
0.0909	22	2	1.8061	4.307	0.0909	33	3	2.7091	4.307
0.0938	32	3	2.6311	4.435	0.0952	21	2	1.7280	4.502
0.0968	31	3	2.5530	4.571	0.1000	10	1	0.8250	4.715
0.1000	20	2	1.6500	4.715	0.1000	30	3	2.4750	4.715
0.1000	40	4	3.2999	4.715	0.1026	39	4	3.2219	4.829
0.1034	29	3	2.3969	4.869	0.1053	19	2	1.5719	4.950
0.1053	38	4	3.1439	4.950	0.1071	28	3	2.3189	5.033
0.1081	37	4	3.0659	5.076	0.1111	9	1	0.7470	5.209
0.1111	18	2	1.4939	5.209	0.1111	27	3	2.2409	5.209
0.1111	36	4	2.9879	5.209	0.1143	35	4	2.9099	5.349
0.1154	26	3	2.1630	5.397	0.1176	17	2	1.4160	5.496
0.1176	34	4	2.8320	5.496	0.1200	25	3	2.0850	5.599
0.1212	33	4	2.7540	5.652	0.1250	8	1	0.6690	5.818
0.1250	16	2	1.3381	5.818	0.1250	24	3	2.0071	5.818
0.1250	32	4	2.6761	5.818	0.1250	40	5	3.3452	5.818
0.1282	39	5	3.2673	5.957	0.1290	31	4	2.5982	5.993
0.1304	23	3	1.9292	6.053	0.1316	38	5	3.1894	6.103
0.1333	15	2	1.2602	6.178	0.1333	30	4	2.5204	6.178
0.1351	37	5	3.1115	6.256	0.1364	22	3	1.8514	6.309
0.1379	29	4	2.4425	6.376	0.1389	36	5	3.0337	6.417
0.1429	7	1	0.5912	6.587	0.1429	14	2	1.1824	6.587
0.1429	21	3	1.7736	6.587	0.1429	28	4	2.3647	6.587
0.1429	35	5	2.9559	6.587	0.1471	34	5	2.8781	6.766
0.1481	27	4	2.2870	6.812	0.1500	20	3	1.6958	6.890
0.1500	40	6	3.3916	6.890	0.1515	33	5	2.8004	6.954
0.1538	13	2	1.1046	7.053	0.1538	26	4	2.2092	7.053
0.1538	39	6	3.3139	7.053	0.1562	32	5	2.7227	7.154
0.1579	19	3	1.6181	7.223	0.1579	38	6	3.2362	7.223

$m/n$	$n$	$m$	$d$ [nm]	$\alpha$ [°]	$m/n$	$n$	$m$	$d$ [nm]	$\alpha$ [°]
0.1600	25	4	2.1315	7.311	0.1613	31	5	2.6450	7.365
0.1622	37	6	3.1585	7.401	0.1667	6	1	0.5135	7.589
0.1667	12	2	1.0270	7.589	0.1667	18	3	1.5404	7.589
0.1667	24	4	2.0539	7.589	0.1667	30	5	2.5674	7.589
0.1667	36	6	3.0809	7.589	0.1714	35	6	3.0033	7.786
0.1724	29	5	2.4898	7.827	0.1739	23	4	1.9763	7.889
0.1750	40	7	3.4392	7.934	0.1765	17	3	1.4628	7.994
0.1765	34	6	2.9257	7.994	0.1786	28	5	2.4122	8.080
0.1795	39	7	3.3616	8.118	0.1818	11	2	0.9494	8.213
0.1818	22	4	1.8988	8.213	0.1818	33	6	2.8482	8.213
0.1842	38	7	3.2841	8.311	0.1852	27	5	2.3347	8.350
0.1875	16	3	1.3853	8.445	0.1875	32	6	2.7707	8.445
0.1892	37	7	3.2067	8.513	0.1905	21	4	1.8213	8.565
0.1923	26	5	2.2573	8.639	0.1935	31	6	2.6933	8.689
0.1944	36	7	3.1292	8.725	0.2000	5	1	0.4360	8.948
0.2000	10	2	0.8720	8.948	0.2000	15	3	1.3079	8.948
0.2000	20	4	1.7439	8.948	0.2000	25	5	2.1799	8.948
0.2000	30	6	2.6159	8.948	0.2000	35	7	3.0519	8.948
0.2000	40	8	3.4878	8.948	0.2051	39	8	3.4105	9.153
0.2059	34	7	2.9745	9.183	0.2069	29	6	2.5386	9.223
0.2083	24	5	2.1026	9.280	0.2105	19	4	1.6666	9.367
0.2105	38	8	3.3332	9.367	0.2121	33	7	2.8973	9.430
0.2143	14	3	1.2306	9.515	0.2143	28	6	2.4613	9.515
0.2162	37	8	3.2560	9.591	0.2174	23	5	2.0253	9.637
0.2188	32	7	2.8200	9.691	0.2222	9	2	0.7947	9.826
0.2222	18	4	1.5894	9.826	0.2222	27	6	2.3841	9.826
0.2222	36	8	3.1788	9.826	0.2250	40	9	3.5376	9.935
0.2258	31	7	2.7429	9.966	0.2273	22	5	1.9482	10.023
0.2286	35	8	3.1017	10.073	0.2308	13	3	1.1535	10.158
0.2308	26	6	2.3070	10.158	0.2308	39	9	3.4605	10.158
0.2333	30	7	2.6658	10.257	0.2353	17	4	1.5123	10.333
0.2353	34	8	3.0246	10.333	0.2368	38	9	3.3834	10.392
0.2381	21	5	1.8711	10.440	0.2400	25	6	2.2300	10.513
0.2414	29	7	2.5888	10.566	0.2424	33	8	2.9476	10.606
0.2432	37	9	3.3064	10.637	0.2500	4	1	0.3588	10.893

$m/n$	$n$	$m$	$d$ [nm]	$\alpha$ [°]	$m/n$	$n$	$m$	$d$ [nm]	$\alpha$ [°]
0.2500	8	2	0.7177	10.893	0.2500	12	3	1.0765	10.893
0.2500	16	4	1.4353	10.893	0.2500	20	5	1.7942	10.893
0.2500	24	6	2.1530	10.893	0.2500	28	7	2.5118	10.893
0.2500	32	8	2.8707	10.893	0.2500	36	9	3.2295	10.893
0.2500	40	10	3.5884	10.893	0.2564	39	10	3.5115	11.135
0.2571	35	9	3.1527	11.162	0.2581	31	8	2.7938	11.197
0.2593	27	7	2.4350	11.242	0.2609	23	6	2.0762	11.302
0.2632	19	5	1.7173	11.387	0.2632	38	10	3.4347	11.387
0.2647	34	9	3.0759	11.445	0.2667	15	4	1.3585	11.518
0.2667	30	8	2.7171	11.518	0.2692	26	7	2.3582	11.612
0.2703	37	10	3.3580	11.651	0.2727	11	3	0.9997	11.742
0.2727	22	6	1.9994	11.742	0.2727	33	9	2.9992	11.742
0.2750	40	11	3.6401	11.825	0.2759	29	8	2.6404	11.857
0.2778	18	5	1.6407	11.927	0.2778	36	10	3.2813	11.927
0.2800	25	7	2.2816	12.008	0.2812	32	9	2.9225	12.054
0.2821	39	11	3.5635	12.083	0.2857	7	2	0.6409	12.216
0.2857	14	4	1.2819	12.216	0.2857	21	6	1.9228	12.216
0.2857	28	8	2.5638	12.216	0.2857	35	10	3.2047	12.216
0.2895	38	11	3.4870	12.352	0.2903	31	9	2.8460	12.383
0.2917	24	7	2.2051	12.432	0.2941	17	5	1.5641	12.520
0.2941	34	10	3.1283	12.520	0.2963	27	8	2.4873	12.598
0.2973	37	11	3.4105	12.634	0.3000	10	3	0.9232	12.731
0.3000	20	6	1.8464	12.731	0.3000	30	9	2.7696	12.731
0.3000	40	12	3.6928	12.731	0.3030	33	10	3.0519	12.839
0.3043	23	7	2.1287	12.885	0.3056	36	11	3.3341	12.928
0.3077	13	4	1.2055	13.004	0.3077	26	8	2.4110	13.004
0.3077	39	12	3.6164	13.004	0.3103	29	9	2.6933	13.098
0.3125	16	5	1.4878	13.174	0.3125	32	10	2.9756	13.174
0.3143	35	11	3.2579	13.236	0.3158	19	6	1.7701	13.289
0.3158	38	12	3.5402	13.289	0.3182	22	7	2.0524	13.373
0.3200	25	8	2.3347	13.436	0.3214	28	9	2.6170	13.486
0.3226	31	10	2.8994	13.526	0.3235	34	11	3.1817	13.559
0.3243	37	12	3.4640	13.587	0.3250	40	13	3.7463	13.610
0.3333	3	1	0.2823	13.898	0.3333	6	2	0.5647	13.898
0.3333	9	3	0.8470	13.898	0.3333	12	4	1.1293	13.898

$m/n$	$n$	$m$	$d$ [nm]	$\alpha$ [°]	$m/n$	$n$	$m$	$d$ [nm]	$\alpha$ [°]
0.3333	15	5	1.4116	13.898	0.3333	18	6	1.6940	13.898
0.3333	21	7	1.9763	13.898	0.3333	24	8	2.2586	13.898
0.3333	27	9	2.5410	13.898	0.3333	30	10	2.8233	13.898
0.3333	33	11	3.1056	13.898	0.3333	36	12	3.3880	13.898
0.3333	39	13	3.6703	13.898	0.3421	38	13	3.5943	14.198
0.3429	35	12	3.3120	14.223	0.3438	32	11	3.0297	14.254
0.3448	29	10	2.7474	14.290	0.3462	26	9	2.4650	14.335
0.3478	23	8	2.1827	14.392	0.3500	20	7	1.9004	14.465
0.3500	40	14	3.8008	14.465	0.3514	37	13	3.5185	14.510
0.3529	17	6	1.6181	14.564	0.3529	34	12	3.2362	14.564
0.3548	31	11	2.9538	14.628	0.3571	14	5	1.3358	14.705
0.3571	28	10	2.6715	14.705	0.3590	39	14	3.7250	14.766
0.3600	25	9	2.3892	14.800	0.3611	36	13	3.4427	14.837
0.3636	11	4	1.0535	14.921	0.3636	22	8	2.1070	14.921
0.3636	33	12	3.1604	14.921	0.3667	30	11	2.8781	15.021
0.3684	19	7	1.8247	15.079	0.3684	38	14	3.6493	15.079
0.3704	27	10	2.5959	15.143	0.3714	35	13	3.3671	15.178
0.3750	8	3	0.7712	15.295	0.3750	16	6	1.5424	15.295
0.3750	24	9	2.3136	15.295	0.3750	32	12	3.0848	15.295
0.3750	40	15	3.8560	15.295	0.3784	37	14	3.5738	15.406
0.3793	29	11	2.8026	15.436	0.3810	21	8	2.0314	15.490
0.3824	34	13	3.2916	15.535	0.3846	13	5	1.2602	15.608
0.3846	26	10	2.5204	15.608	0.3846	39	15	3.7806	15.608
0.3871	31	12	3.0094	15.689	0.3889	18	7	1.7492	15.746
0.3889	36	14	3.4984	15.746	0.3913	23	9	2.2382	15.824
0.3929	28	11	2.7272	15.874	0.3939	33	13	3.2162	15.909
0.3947	38	15	3.7052	15.934	0.4000	5	2	0.4890	16.102
0.4000	10	4	0.9780	16.102	0.4000	15	6	1.4670	16.102
0.4000	20	8	1.9560	16.102	0.4000	25	10	2.4450	16.102
0.4000	30	12	2.9341	16.102	0.4000	35	14	3.4231	16.102
0.4000	40	16	3.9121	16.102	0.4054	37	15	3.6300	16.274
0.4062	32	13	3.1410	16.300	0.4074	27	11	2.6520	16.337
0.4091	22	9	2.1630	16.390	0.4103	39	16	3.8369	16.426
0.4118	17	7	1.6740	16.474	0.4118	34	14	3.3479	16.474
0.4138	29	12	2.8589	16.537	0.4167	12	5	1.1850	16.627

$m/n$	$n$	$m$	$d$ [nm]	$\alpha$ [°]	$m/n$	$n$	$m$	$d$ [nm]	$\alpha$ [°]
0.4167	24	10	2.3699	16.627	0.4167	36	15	3.5549	16.627
0.4194	31	13	3.0659	16.711	0.4211	19	8	1.8809	16.764
0.4211	38	16	3.7619	16.764	0.4231	26	11	2.5769	16.826
0.4242	33	14	3.2729	16.863	0.4250	40	17	3.9689	16.886
0.4286	7	3	0.6960	16.996	0.4286	14	6	1.3920	16.996
0.4286	21	9	2.0879	16.996	0.4286	28	12	2.7839	16.996
0.4286	35	15	3.4799	16.996	0.4324	37	16	3.6870	17.115
0.4333	30	13	2.9910	17.142	0.4348	23	10	2.2950	17.187
0.4359	39	17	3.8940	17.221	0.4375	16	7	1.5990	17.269
0.4375	32	14	3.1980	17.269	0.4400	25	11	2.5021	17.346
0.4412	34	15	3.4051	17.381	0.4444	9	4	0.9030	17.480
0.4444	18	8	1.8061	17.480	0.4444	27	12	2.7091	17.480
0.4444	36	16	3.6122	17.480	0.4474	38	17	3.8193	17.568
0.4483	29	13	2.9162	17.596	0.4500	20	9	2.0132	17.648
0.4500	40	18	4.0264	17.648	0.4516	31	14	3.1233	17.696
0.4545	11	5	1.1102	17.784	0.4545	22	10	2.2203	17.784
0.4545	33	15	3.3305	17.784	0.4571	35	16	3.5376	17.861
0.4583	24	11	2.4274	17.897	0.4595	37	17	3.7447	17.930
0.4615	13	6	1.3173	17.992	0.4615	26	12	2.6346	17.992
0.4615	39	18	3.9518	17.992	0.4643	28	13	2.8417	18.073
0.4667	15	7	1.5244	18.143	0.4667	30	14	3.0488	18.143
0.4688	32	15	3.2560	18.205	0.4706	17	8	1.7316	18.258
0.4706	34	16	3.4631	18.258	0.4722	36	17	3.6703	18.306
0.4737	19	9	1.9387	18.349	0.4737	38	18	3.8774	18.349
0.4750	40	19	4.0846	18.388	0.4762	21	10	2.1459	18.422
0.4783	23	11	2.3530	18.482	0.4800	25	12	2.5602	18.533
0.4815	27	13	2.7674	18.576	0.4828	29	14	2.9745	18.613
0.4839	31	15	3.1817	18.645	0.4848	33	16	3.3889	18.673
0.4857	35	17	3.5960	18.698	0.4865	37	18	3.8032	18.720
0.4872	39	19	4.0104	18.740	0.5000	2	1	0.2072	19.107
0.5000	4	2	0.4143	19.107	0.5000	6	3	0.6215	19.107
0.5000	8	4	0.8287	19.107	0.5000	10	5	1.0359	19.107
0.5000	12	6	1.2430	19.107	0.5000	14	7	1.4502	19.107
0.5000	16	8	1.6574	19.107	0.5000	18	9	1.8646	19.107
0.5000	20	10	2.0717	19.107	0.5000	22	11	2.2789	19.107

$m/n$	$n$	$m$	$d$ [nm]	$\alpha$ [°]	$m/n$	$n$	$m$	$d$ [nm]	$\alpha$ [°]
0.5000	24	12	2.4861	19.107	0.5000	26	13	2.6933	19.107
0.5000	28	14	2.9004	19.107	0.5000	30	15	3.1076	19.107
0.5000	32	16	3.3148	19.107	0.5000	34	17	3.5219	19.107
0.5000	36	18	3.7291	19.107	0.5000	38	19	3.9363	19.107
0.5000	40	20	4.1435	19.107	0.5128	39	20	4.0696	19.467
0.5135	37	19	3.8624	19.487	0.5143	35	18	3.6552	19.508
0.5152	33	17	3.4481	19.533	0.5161	31	16	3.2409	19.560
0.5172	29	15	3.0337	19.591	0.5185	27	14	2.8266	19.626
0.5200	25	13	2.6194	19.667	0.5217	23	12	2.4122	19.715
0.5238	21	11	2.2051	19.773	0.5250	40	21	4.2030	19.805
0.5263	19	10	1.9979	19.842	0.5263	38	20	3.9958	19.842
0.5278	36	19	3.7887	19.882	0.5294	17	9	1.7908	19.927
0.5294	34	18	3.5815	19.927	0.5312	32	17	3.3744	19.977
0.5333	15	8	1.5836	20.034	0.5333	30	16	3.1672	20.034
0.5357	28	15	2.9601	20.099	0.5385	13	7	1.3765	20.174
0.5385	26	14	2.7529	20.174	0.5385	39	21	4.1294	20.174
0.5405	37	20	3.9223	20.230	0.5417	24	13	2.5458	20.260
0.5429	35	19	3.7151	20.293	0.5455	11	6	1.1693	20.363
0.5455	22	12	2.3387	20.363	0.5455	33	18	3.5080	20.363
0.5484	31	17	3.3009	20.441	0.5500	20	11	2.1315	20.485
0.5500	40	22	4.2631	20.485	0.5517	29	16	3.0938	20.531
0.5526	38	21	4.0560	20.555	0.5556	9	5	0.9622	20.633
0.5556	18	10	1.9244	20.633	0.5556	27	15	2.8867	20.633
0.5556	36	20	3.8489	20.633	0.5588	34	19	3.6418	20.720
0.5600	25	14	2.6796	20.751	0.5625	16	9	1.7173	20.817
0.5625	32	18	3.4347	20.817	0.5641	39	22	4.1898	20.859
0.5652	23	13	2.4725	20.889	0.5667	30	17	3.2276	20.927
0.5676	37	21	3.9828	20.951	0.5714	7	4	0.7551	21.052
0.5714	14	8	1.5103	21.052	0.5714	21	12	2.2654	21.052
0.5714	28	16	3.0206	21.052	0.5714	35	20	3.7757	21.052
0.5750	40	23	4.3238	21.145	0.5758	33	19	3.5686	21.165
0.5769	26	15	2.8135	21.195	0.5789	19	11	2.0584	21.247
0.5789	38	22	4.1167	21.247	0.5806	31	18	3.3616	21.291
0.5833	12	7	1.3032	21.361	0.5833	24	14	2.6065	21.361
0.5833	36	21	3.9097	21.361	0.5862	29	17	3.1546	21.435

$m/n$	$n$	$m$	$d$ [nm]	$\alpha$ [°]	$m/n$	$n$	$m$	$d$ [nm]	$\alpha$ [°]
0.5882	17	10	1.8514	21.487	0.5882	34	20	3.7027	21.487
0.5897	39	23	4.2508	21.526	0.5909	22	13	2.3995	21.555
0.5926	27	16	2.9476	21.598	0.5938	32	19	3.4957	21.628
0.5946	37	22	4.0439	21.650	0.6000	5	3	0.5481	21.787
0.6000	10	6	1.0963	21.787	0.6000	15	9	1.6444	21.787
0.6000	20	12	2.1925	21.787	0.6000	25	15	2.7406	21.787
0.6000	30	18	3.2888	21.787	0.6000	35	21	3.8369	21.787
0.6000	40	24	4.3850	21.787	0.6053	38	23	4.1781	21.920
0.6061	33	20	3.6300	21.940	0.6071	28	17	3.0818	21.967
0.6087	23	14	2.5337	22.006	0.6111	18	11	1.9856	22.066
0.6111	36	22	3.9712	22.066	0.6129	31	19	3.4231	22.111
0.6154	13	8	1.4375	22.173	0.6154	26	16	2.8749	22.173
0.6154	39	24	4.3124	22.173	0.6176	34	21	3.7643	22.229
0.6190	21	13	2.3268	22.264	0.6207	29	18	3.2162	22.305
0.6216	37	23	4.1056	22.328	0.6250	8	5	0.8894	22.411
0.6250	16	10	1.7787	22.411	0.6250	24	15	2.6681	22.411
0.6250	32	20	3.5575	22.411	0.6250	40	25	4.4468	22.411
0.6286	35	22	3.8987	22.499	0.6296	27	17	3.0094	22.525
0.6316	19	12	2.1200	22.572	0.6316	38	24	4.2400	22.572
0.6333	30	19	3.3507	22.615	0.6364	11	7	1.2306	22.689
0.6364	22	14	2.4613	22.689	0.6364	33	21	3.6919	22.689
0.6389	36	23	4.0332	22.750	0.6400	25	16	2.8026	22.777
0.6410	39	25	4.3745	22.802	0.6429	14	9	1.5719	22.846
0.6429	28	18	3.1439	22.846	0.6452	31	20	3.4852	22.902
0.6471	17	11	1.9133	22.947	0.6471	34	22	3.8265	22.947
0.6486	37	24	4.1678	22.985	0.6500	20	13	2.2546	23.018
0.6500	40	26	4.5091	23.018	0.6522	23	15	2.5959	23.070
0.6538	26	17	2.9372	23.110	0.6552	29	19	3.2785	23.141
0.6562	32	21	3.6198	23.167	0.6571	35	23	3.9611	23.188
0.6579	38	25	4.3025	23.206	0.6667	3	2	0.3413	23.413
0.6667	6	4	0.6826	23.413	0.6667	9	6	1.0240	23.413
0.6667	12	8	1.3653	23.413	0.6667	15	10	1.7066	23.413
0.6667	18	12	2.0479	23.413	0.6667	21	14	2.3892	23.413
0.6667	24	16	2.7306	23.413	0.6667	27	18	3.0719	23.413
0.6667	30	20	3.4132	23.413	0.6667	33	22	3.7545	23.413

$m/n$	$n$	$m$	$d$ [nm]	$\alpha$ [°]	$m/n$	$n$	$m$	$d$ [nm]	$\alpha$ [°]
0.6667	36	24	4.0958	23.413	0.6667	39	26	4.4372	23.413
0.6750	40	27	4.5719	23.608	0.6757	37	25	4.2306	23.624
0.6765	34	23	3.8893	23.642	0.6774	31	21	3.5480	23.664
0.6786	28	19	3.2067	23.691	0.6800	25	17	2.8653	23.724
0.6818	22	15	2.5240	23.766	0.6842	19	13	2.1827	23.822
0.6842	38	26	4.3654	23.822	0.6857	35	24	4.0241	23.856
0.6875	16	11	1.8414	23.897	0.6875	32	22	3.6828	23.897
0.6897	29	20	3.3415	23.947	0.6923	13	9	1.5001	24.007
0.6923	26	18	3.0002	24.007	0.6923	39	27	4.5003	24.007
0.6944	36	25	4.1590	24.056	0.6957	23	16	2.6589	24.084
0.6970	33	23	3.8177	24.114	0.7000	10	7	1.1588	24.182
0.7000	20	14	2.3176	24.182	0.7000	30	21	3.4764	24.182
0.7000	40	28	4.6352	24.182	0.7027	37	26	4.2939	24.244
0.7037	27	19	3.1351	24.266	0.7059	17	12	1.9763	24.315
0.7059	34	24	3.9526	24.315	0.7083	24	17	2.7938	24.370
0.7097	31	22	3.6113	24.401	0.7105	38	27	4.4289	24.420
0.7143	7	5	0.8175	24.504	0.7143	14	10	1.6350	24.504
0.7143	21	15	2.4526	24.504	0.7143	28	20	3.2701	24.504
0.7143	35	25	4.0876	24.504	0.7179	39	28	4.5639	24.585
0.7188	32	23	3.7463	24.603	0.7200	25	18	2.9288	24.631
0.7222	18	13	2.1113	24.680	0.7222	36	26	4.2226	24.680
0.7241	29	21	3.4051	24.722	0.7250	40	29	4.6989	24.741
0.7273	11	8	1.2938	24.791	0.7273	22	16	2.5876	24.791
0.7273	33	24	3.8814	24.791	0.7297	37	27	4.3577	24.845
0.7308	26	19	3.0639	24.868	0.7333	15	11	1.7701	24.924
0.7333	30	22	3.5402	24.924	0.7353	34	25	4.0165	24.967
0.7368	19	14	2.2464	25.001	0.7368	38	28	4.4928	25.001
0.7391	23	17	2.7227	25.050	0.7407	27	20	3.1990	25.085
0.7419	31	23	3.6753	25.111	0.7429	35	26	4.1516	25.131
0.7436	39	29	4.6279	25.147	0.7500	4	3	0.4763	25.285
0.7500	8	6	0.9526	25.285	0.7500	12	9	1.4289	25.285
0.7500	16	12	1.9052	25.285	0.7500	20	15	2.3815	25.285
0.7500	24	18	2.8578	25.285	0.7500	28	21	3.3341	25.285
0.7500	32	24	3.8104	25.285	0.7500	36	27	4.2868	25.285
0.7500	40	30	4.7631	25.285	0.7568	37	28	4.4219	25.429

$m/n$	$n$	$m$	$d$ [nm]	$\alpha$ [°]	$m/n$	$n$	$m$	$d$ [nm]	$\alpha$ [°]
0.7576	33	25	3.9456	25.447	0.7586	29	22	3.4693	25.469
0.7600	25	19	2.9930	25.498	0.7619	21	16	2.5167	25.539
0.7632	38	29	4.5571	25.565	0.7647	17	13	2.0404	25.598
0.7647	34	26	4.0808	25.598	0.7667	30	23	3.6045	25.639
0.7692	13	10	1.5641	25.693	0.7692	26	20	3.1283	25.693
0.7692	39	30	4.6924	25.693	0.7714	35	27	4.2161	25.740
0.7727	22	17	2.6520	25.767	0.7742	31	24	3.7398	25.797
0.7750	40	31	4.8276	25.814	0.7778	9	7	1.0878	25.872
0.7778	18	14	2.1757	25.872	0.7778	27	21	3.2635	25.872
0.7778	36	28	4.3513	25.872	0.7812	32	25	3.8751	25.944
0.7826	23	18	2.7872	25.973	0.7838	37	29	4.4866	25.997
0.7857	14	11	1.6994	26.037	0.7857	28	22	3.3988	26.037
0.7879	33	26	4.0104	26.081	0.7895	19	15	2.3110	26.114
0.7895	38	30	4.6219	26.114	0.7917	24	19	2.9225	26.159
0.7931	29	23	3.5341	26.189	0.7941	34	27	4.1457	26.210
0.7949	39	31	4.7573	26.225	0.8000	5	4	0.6116	26.330
0.8000	10	8	1.2232	26.330	0.8000	15	12	1.8347	26.330
0.8000	20	16	2.4463	26.330	0.8000	25	20	3.0579	26.330
0.8000	30	24	3.6695	26.330	0.8000	35	28	4.2810	26.330
0.8000	40	32	4.8926	26.330	0.8056	36	29	4.4164	26.442
0.8065	31	25	3.8048	26.460	0.8077	26	21	3.1932	26.485
0.8095	21	17	2.5817	26.522	0.8108	37	30	4.5518	26.548
0.8125	16	13	1.9701	26.582	0.8125	32	26	3.9402	26.582
0.8148	27	22	3.3286	26.628	0.8158	38	31	4.6871	26.648
0.8182	11	9	1.3585	26.696	0.8182	22	18	2.7171	26.696
0.8182	33	27	4.0756	26.696	0.8205	39	32	4.8225	26.742
0.8214	28	23	3.4640	26.760	0.8235	17	14	2.1055	26.802
0.8235	34	28	4.2110	26.802	0.8250	40	33	4.9580	26.831
0.8261	23	19	2.8525	26.853	0.8276	29	24	3.5994	26.882
0.8286	35	29	4.3464	26.902	0.8333	6	5	0.7470	26.996
0.8333	12	10	1.4939	26.996	0.8333	18	15	2.2409	26.996
0.8333	24	20	2.9879	26.996	0.8333	30	25	3.7349	26.996
0.8333	36	30	4.4818	26.996	0.8378	37	31	4.6173	27.084
0.8387	31	26	3.8703	27.101	0.8400	25	21	3.1233	27.126
0.8421	19	16	2.3764	27.167	0.8421	38	32	4.7528	27.167

$m/n$	$n$	$m$	$d$ [nm]	$\alpha$ [°]	$m/n$	$n$	$m$	$d$ [nm]	$\alpha$ [°]
0.8438	32	27	4.0058	27.199	0.8462	13	11	1.6294	27.245
0.8462	26	22	3.2588	27.245	0.8462	39	33	4.8882	27.245
0.8485	33	28	4.1413	27.291	0.8500	20	17	2.5118	27.320
0.8500	40	34	5.0237	27.320	0.8519	27	23	3.3943	27.356
0.8529	34	29	4.2767	27.376	0.8571	7	6	0.8824	27.457
0.8571	14	12	1.7649	27.457	0.8571	21	18	2.6473	27.457
0.8571	28	24	3.5298	27.457	0.8571	35	30	4.4122	27.457
0.8611	36	31	4.5477	27.533	0.8621	29	25	3.6653	27.551
0.8636	22	19	2.7828	27.581	0.8649	37	32	4.6832	27.604
0.8667	15	13	1.9004	27.638	0.8667	30	26	3.8008	27.638
0.8684	38	33	4.8187	27.672	0.8696	23	20	2.9183	27.693
0.8710	31	27	3.9363	27.720	0.8718	39	34	4.9543	27.735
0.8750	8	7	1.0180	27.796	0.8750	16	14	2.0359	27.796
0.8750	24	21	3.0539	27.796	0.8750	32	28	4.0718	27.796
0.8750	40	35	5.0898	27.796	0.8788	33	29	4.2073	27.867
0.8800	25	22	3.1894	27.889	0.8824	17	15	2.1714	27.933
0.8824	34	30	4.3429	27.933	0.8846	26	23	3.3249	27.976
0.8857	35	31	4.4784	27.996	0.8889	9	8	1.1535	28.055
0.8889	18	16	2.3070	28.055	0.8889	27	24	3.4605	28.055
0.8889	36	32	4.6140	28.055	0.8919	37	33	4.7495	28.110
0.8929	28	25	3.5960	28.128	0.8947	19	17	2.4425	28.163
0.8947	38	34	4.8851	28.163	0.8966	29	26	3.7316	28.196
0.8974	39	35	5.0206	28.212	0.9000	10	9	1.2891	28.259
0.9000	20	18	2.5781	28.259	0.9000	30	27	3.8672	28.259
0.9000	40	36	5.1562	28.259	0.9032	31	28	4.0027	28.318
0.9048	21	19	2.7137	28.346	0.9062	32	29	4.1383	28.374
0.9091	11	10	1.4246	28.425	0.9091	22	20	2.8492	28.425
0.9091	33	30	4.2739	28.425	0.9118	34	31	4.4094	28.474
0.9130	23	21	2.9848	28.497	0.9143	35	32	4.5450	28.519
0.9167	12	11	1.5602	28.562	0.9167	24	22	3.1204	28.562
0.9167	36	33	4.6806	28.562	0.9189	37	34	4.8162	28.603
0.9200	25	23	3.2560	28.622	0.9211	38	35	4.9518	28.641
0.9231	13	12	1.6958	28.677	0.9231	26	24	3.3916	28.677
0.9231	39	36	5.0874	28.677	0.9250	40	37	5.2230	28.711
0.9259	27	25	3.5272	28.728	0.9286	14	13	1.8314	28.775

$m/n$	$n$	$m$	$d$ [nm]	$\alpha$ [°]	$m/n$	$n$	$m$	$d$ [nm]	$\alpha$ [°]
0.9286	28	26	3.6628	28.775	0.9310	29	27	3.7984	28.819
0.9333	15	14	1.9670	28.859	0.9333	30	28	3.9340	28.859
0.9355	31	29	4.0696	28.897	0.9375	16	15	2.1026	28.933
0.9375	32	30	4.2052	28.933	0.9394	33	31	4.3408	28.966
0.9412	17	16	2.2382	28.998	0.9412	34	32	4.4764	28.998
0.9429	35	33	4.6120	29.027	0.9444	18	17	2.3738	29.055
0.9444	36	34	4.7476	29.055	0.9459	37	35	4.8832	29.081
0.9474	19	18	2.5094	29.106	0.9474	38	36	5.0188	29.106
0.9487	39	37	5.1544	29.130	0.9500	20	19	2.6450	29.152
0.9500	40	38	5.2900	29.152	0.9524	21	20	2.7806	29.193
0.9545	22	21	2.9162	29.231	0.9565	23	22	3.0519	29.265
0.9583	24	23	3.1875	29.296	0.9600	25	24	3.3231	29.325
0.9615	26	25	3.4587	29.351	0.9630	27	26	3.5943	29.376
0.9643	28	27	3.7299	29.399	0.9655	29	28	3.8656	29.420
0.9667	30	29	4.0012	29.439	0.9677	31	30	4.1368	29.458
0.9688	32	31	4.2724	29.475	0.9697	33	32	4.4080	29.491
0.9706	34	33	4.5437	29.506	0.9714	35	34	4.6793	29.521
0.9722	36	35	4.8149	29.534	0.9730	37	36	4.9505	29.547
0.9737	38	37	5.0862	29.559	0.9744	39	38	5.2218	29.570
0.9750	40	39	5.3574	29.581					

# Bibliography

- [1] Riichiro Saito, Gene Dresselhaus, Mildred S. Dresselhaus, *Physical properties of carbon nanotubes*, London (2007)
- [2] Charles Kittel, *Einführung in die Festkörperphysik*, Oldenbourg 1999
- [3] Kleber, Bautsch, Bohm, *Einführung in die Kristallographie*, Verlag Technik GmbH Berlin (1990)
- [4] Lu-Chang Qin, *Electron diffraction from carbon nanotubes*, Rep. Prog. Phys. 69 2761-2821 (2006)
- [5] L. C. Qin, T. Ichihashi and S. Iijima, *On the measurement of helicity of carbon nanotubes*, Ultramicroscopy Volume 67, Issues 1-4, 181-189 (1997)
- [6] Zejian Liu, Lu-Chang Qin, *Breakdown of 2mm symmetry in electron diffraction for multiwalled carbon nanotubes*, Chemical Physics Letters 402, 202-205 (2005)
- [7] Lu-Chang Qin, *Measuring the true helicity of carbon nanotubes*, Chem. Phys. Lett. 297, 23 (1998)
- [8] Zejian Liu, Lu-Chang Qin, *Symmetry of electron diffraction from single-walled carbon nanotubes*, Chem. Phys. Lett. 400, 430-435 (2004)
- [9] M. Gao, J. M. Zuo, R. D. Twisten, I. Petrov, L. A. Nagahara and R. Zhang, *Structure determination of individual single-wall carbon nanotubes by nanoarea electron diffraction*, Applied Physics Letters, Volume 82, Number 16 (2003)
- [10] John C. Russ, *The image processing handbook*, CRC Press, Inc. 2nd edition (1995)
- [11] Harald Broll, *Analyse von Peptide-Maps mit Hilfe von neuronalen Netzen*, Universität Regensburg (2000)

- [12] Blair Mackiewicz, *Intracranial Boundary Detection and Radio Frequency Correction in Magnetic Resonance Images*, Simon Fraser University (1995)
- [13] Ph. Lambin and A. A. Lucas, *Quantitative theory of diffraction by carbon nanotubes*, Phys. Rev. B 56, 3571 (1997)
- [14] P.A. Doyle and P.S. Turner, *Relativistic hartree-fock x-ray and electron scattering factors*, Acta Cryst. A 24 (1968) 390
- [15] Hua Jiang, *Unambiguous atomic structural determination of single-walled carbon nanotubes by electron diffraction*, ScienceDirect Carbon 45 662-667 (2007)
- [16] Christian Huber, *Elektronenmikroskopische Strukturuntersuchungen an Kohlenstoffnanoröhren*, Universität Regensburg (2009)

# Acknowledgment

An dieser Stelle möchte ich allen meinen Dank aussprechen, ohne die diese Arbeit nicht möglich gewesen wäre. Dies waren insbesondere:

- Professor Dr. Elmar W. Lang, der mir dieses Thema anbot und mir stets mit Rat zur Seite stand.
- Professor Dr. Christoph Strunk, der durch sein Interesse an den Ergebnissen der Arbeit diese erst ermöglichte und sie auch finanziell unterstützte.
- Professor Dr. Josef Zweck, der stets ein offenes Ohr für alle Fragen zur Elektronenmikroskopie hatte.
- Christian Huber und Elsa Thune, die mir experimentelle Beugungsaufnahmen zur Verfügung stellten.
- Die gesamte AG-Lang, in der ich eine hervorragende Zeit hatte und ein tolles Arbeitsklima herrschte. Ich danke auch für die fachlichen Diskussionen, insbesondere Matthias Böhm.
- Die DFG, durch deren Stipendium der Großteil dieser Arbeit finanziert wurde.
- Meine Familie, die mich während meines gesamten Studiums stets vorbehaltlos unterstützte.
- Meine Freundin und Kollegin Angela Zeiler, die mir sowohl moralisch als auch fachlich eine nicht zu ersetzende Stütze war.



# Erklärung

## Eidesstattliche Erklärung

Ich erkläre hiermit an Eides statt, dass ich die vorliegende Arbeit ohne unzulässige Hilfe Dritter und ohne Benutzung anderer als der angegebenen Hilfsmittel angefertigt habe; die aus anderen Quellen direkt oder indirekt übernommenen Daten und Konzepte sind unter Angabe des Literaturzitats gekennzeichnet.

Bei der Auswahl und Auswertung folgenden Materials haben mir die nachstehend aufgeführten Personen in der jeweils beschriebenen Weise unentgeltlich geholfen:

Beugungsbilder: Wurden zur Verfügung gestellt von den Arbeitsgruppen Strunk und Zweck

Weitere Personen waren an der inhaltlich-materiellen Herstellung der vorliegenden Arbeit nicht beteiligt. Insbesondere habe ich hierfür nicht die entgeltliche Hilfe eines Promotionsberaters oder anderer Personen in Anspruch genommen. Niemand hat von mir weder unmittelbar noch mittelbar geldwerte Leistungen für Arbeiten erhalten, die im Zusammenhang mit dem Inhalt der vorgelegten Dissertation stehen.

Die Arbeit wurde bisher weder im In- noch im Ausland in gleicher oder ähnlicher Form einer anderen Prüfungsbehörde vorgelegt.

Regensburg, den 06.07.2011

Dominik Senninger